

ABSTRACT

Title of Document: DEVELOPMENT OF AN EXPERIMENT FOR
MEASURING FILM COOLING
PERFORMANCE IN SUPERSONIC FLOWS

Daanish Maqbool
M.S. Aerospace Engineering, 2010

Directed By: Christopher Cadou
Associate Professor

This thesis describes the development of an experiment for acquiring supersonic film cooling performance data in canonical configurations suitable for code validation.

A methodology for selecting appropriate experimental conditions is developed and used to select test conditions in the UMD atmospheric pressure wind tunnel that are relevant to film cooling conditions encountered in the J-2X rocket engine. A new technique for inferring wall heat flux with 10% uncertainty from temperature-time histories of embedded sensors is developed and implemented. Preliminary heat flux measurements on the uncooled upper wall and on the lower wall with the film cooling flow turned off suggest that RANS solvers using Menter's SST model are able to predict heat flux within 15% in the far-field (> 10 injection slot heights) but are very inaccurate in the near-field. However, more experiments are needed to confirm this finding. Preliminary Schlieren images showing the shear layer growth rate are also presented.

DEVELOPMENT OF AN EXPERIMENT FOR MEASURING FILM COOLING
PERFORMANCE IN SUPERSONIC FLOWS

By

Daanish Maqbool

Thesis submitted to the Faculty of the Graduate School of the
University of Maryland, College Park, in partial fulfillment
of the requirements for the degree of
M.S. Aerospace Engineering
2011

Advisory Committee:
Assoc. Professor Christopher Cadou, Chair
Assoc. Professor Andre Marshall
Professor Mark Lewis

© Copyright by
Daanish Maqbool
2011

To my grandparents.

Table of Contents

Table of Contents.....	iii
Chapter 1: Introduction.....	1
1.1 Motivation.....	1
1.2 Film Cooling Basics.....	2
1.3 Previous Work: Film Cooling.....	5
1.4 Previous Work: Heat Flux Measurements.....	10
1.5 Objectives and Approach.....	13
Chapter 2: Experiment Design.....	14
2.1 Experiment Overview.....	14
2.2 Selection of Test Conditions.....	15
2.3 Modifications to UMD Supersonic Wind Tunnel.....	21
2.4 Component Design.....	23
2.4.1 Estimation of Test Time.....	23
2.4.2 Test Section Arrangement.....	23
2.4.3 Supersonic Contour Design.....	26
2.4.4 Test Surfaces.....	28
2.4.5 Film Heater.....	30
2.5 Instrumentation.....	32
2.5.1 Heat Flux Measurement.....	32
2.5.2 Pressure Measurement.....	37
2.5.3 Schlieren Imaging.....	38
2.5.4 Data Acquisition.....	39
Chapter 3: Inverse Measurement of Heat Flux.....	43
3.1 Introduction.....	43
3.2 Inverse Measurement Technique.....	44
3.2.1 Case of Uniform Initial Wall Temperature.....	44
3.2.2 Case of Initial Temperature Gradient.....	46
3.2.3 Note on Implementation.....	48
3.3 Transient Convection.....	49
3.3.1 Wall Temperature Distribution with Initial Temperature Gradient.....	50
3.3.2 Thermal Penetration Depth.....	54
3.4 Numerical Verification of Results.....	54
3.5 The Effect of N (number of terms).....	60
3.6 Uncertainty in Heat Flux and Temperature Measurements.....	62
3.7 Instrumentation Test.....	65
Chapter 4: Results.....	67
4.1 Configuration of demonstration experiments.....	67
4.2 Schlieren Imaging and Pressure Measurements.....	68
4.2.1 Test Case 3.....	68
4.2.2 Test Case 2.....	72
4.2.3 Test Case 1.....	74
4.2.4 No Film Flow.....	76

4.2.5 Comparison of Schlieren Images	78
4.2.6 Comparison with Numerical Results	79
4.3 Heat Transfer Measurements	82
4.3.1 Upper Wall Heat Flux	82
4.3.2 Lower Wall Heat Flux with No Film Flow.....	87
Chapter 5: Conclusion.....	90
5.1 Summary of Findings.....	90
5.2 Main Contributions	92
5.3 Future Work	92
Appendix A: Method of Characteristics MATLAB Code.....	94
Appendix B: Derivation of Inverse Method	98
Appendix C: Inverse Method MATLAB Code	100
Appendix D: Full-view Schlieren Images.....	107
Bibliography	110

Chapter 1: Introduction

1.1 Motivation

The performance of heat engines generally improves with higher operating temperatures. In the quest for performance, gas temperatures achieved inside aerospace engines often exceed the melting temperature of the material which constitutes the engine. Therefore, active cooling mechanisms are essential for protecting engine components and ensuring sustained and reliable operation of the engine.

With regard to rocket engines, a number of cooling techniques have been developed over the years. The most notable of these are regenerative, radiation, and film cooling¹. In regenerative cooling, fuel is circulated through the walls of the engine prior to being injected into the combustion chamber. The relatively cool fuel serves to cool the walls, thereby also recovering some of the thermal energy lost by the combustion gases to the walls - hence the name 'regenerative' cooling. In radiation cooling, heat is expelled from the walls by radiation to the environment. Lastly, film cooling involves the injection of a thin layer of coolant fluid along the wall to physically separate the wall from the hot core flow. Film cooling is the subject of this study, and will be explained in more detail later.

The J-2X rocket engine (Figure 1.1), being developed by Pratt & Whitney Rocketdyne to power the upper stage of NASA's Ares I rocket, uses film cooling to protect its nozzle extension. The University of Maryland is supporting the engine's development by conducting fundamental investigations of film cooling effectiveness in supersonic environments analogous to those that will be encountered in the engine. The overall goal of the research program is to develop experimentally validated computational tools to predict film cooling performance in supersonic conditions like those in the J-2X nozzle.



Figure 1.1: J-2X engine (Image credit: NASA).

1.2 Film Cooling Basics

Film cooling is a common strategy in gas turbine combustors and rocket engine combustion chambers to protect the walls from extremely hot gas flows¹⁻². It involves the injection of a relatively cool layer of fluid along the wall that is to be protected as

shown in Fig. 1.2. At the interface of the two streams, a shear layer forms. This shear layer grows with distance and eventually its lower edge reaches the wall. At this point, the thermal protection offered by the film starts to drop rapidly.

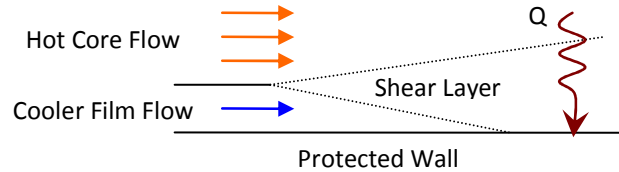


Figure 1.2: Film cooling concept.

Film cooling effectiveness is usually defined as^{3,4}

$$\eta(x) = \frac{T_w(x) - T_\infty}{T_f - T_\infty} \quad (1-1)$$

where T_w is the adiabatic wall temperature, T_∞ is the recovery temperature of the core flow, and T_f is the recovery temperature of the film flow. The effectiveness changes with downstream distance as the film breaks down. At zero distance (at the point of film injection), the adiabatic wall temperature should be the same as the recovery temperature of the film flow which implies that the initial film cooling effectiveness, η , is 1. As the flow moves downstream, the film will eventually completely break down and the adiabatic wall temperature will approach the recovery temperature of the core flow. At this point, η will approach 0.

However, there are situations where the walls are not adiabatic. In this case, there is heat flux into the walls which also changes with downstream distance as the film breaks down. The film cooling effectiveness is then defined as⁴

$$\eta(x) = 1 - \frac{Q(x)}{Q_0} \quad (1-2)$$

where $Q(x)$ is the heat flux into the wall from the flow on the film-cooled side, and Q_0 is the heat flux into the wall that would result if there was no thermal protection i.e. the core flow simply flowed over the wall. $Q(x)$ changes with distance as the shear layer grows and the film breaks down. $Q(x=0)$ is expected to be at a minimum because the flow immediately next to the wall is dominated by the cooler film, and therefore η is expected to be at a maximum. However, as the flow progresses, the film will break down and the fluid will come into direct contact with the hot core flow. At this point, the heat flux into the walls will approach Q_0 , and η will therefore approach 0.

Film cooling performance depends on several fundamental non-dimensional parameters⁵:

$$M_c = \frac{u_\infty - u_f}{a_\infty + a_f} \quad (1-3)$$

$$\lambda = \frac{\rho_f u_f}{\rho_\infty u_\infty} \quad (1-4)$$

$$s = \frac{\rho_f}{\rho_\infty} \quad (1-5)$$

$$r = \frac{u_\infty}{u_f} \quad (1-6)$$

M_C is the convective Mach number, λ is the blowing ratio, s is the density ratio, and r is the velocity ratio. Similarity between different film cooling flows is established based on these non-dimensional parameters. While it is not usually possible to match all non-dimensional quantities in a lab-based experiment, the objective when designing an experiment is to bring the values of these parameters as close as possible to their values in the actual application (in this case the J-2X nozzle extension).

1.3 Previous Work: Film Cooling

Film cooling in supersonic environments has been extensively studied over the years. The motivation for previous research has included thermal protection for scramjet combustors, rocket nozzles, and optical surfaces on high-speed projectiles.

Perhaps the earliest study on supersonic film cooling was conducted by Goldstein et al⁶. Their investigations involved a Mach 3 core air flow with at most sonic injection of air and helium through a slot. The test section area was 2.5 square inches and the blowing ratio was varied between 0 and 0.4. The actual experiment focused on an analogous film heating problem in which the film flow was heated while the core flow remained unheated. This reversed the traditional temperature distributions in a film cooling scenario, but still enabled assessment of the film cooling effectiveness

from adiabatic wall temperature measurements. Goldstein and his colleagues found that the film cooling effectiveness in supersonic flows remained close to 1 for a considerable distance downstream of the injection point before decaying rapidly. In addition, Goldstein et al. used Schlieren imaging to identify the major flow features in a supersonic film flow. In particular, they identified an expansion fan in the core flow emanating from the point where the two streams meet, and a recompression shock at small film flow rates when the core flow is turned into itself upon meeting the wall after the step. The strength of the recompression shock decreases in strength as the film flow is increased.

A very comprehensive supersonic film cooling study was undertaken by Bass, Hardin, and Rodgers⁷. They experimented with hydrogen and nitrogen as a coolant in a vitiated Mach 3 core airstream in an effort to simulate scramjet combustor conditions. The study considered several slot heights, lip thicknesses, nozzle shapes, and coolant Mach numbers. Their experiments lasted for 150 seconds, which was enough time to achieve a thermal steady-state, so film cooling effectiveness was calculated using temperature data. An interesting observation was that combustion occurred in the shear layer between the core and film streams when hydrogen was injected as the coolant. A consistent observation throughout all their experiments was the existence of two distinct effectiveness profiles for hydrogen and nitrogen with hydrogen producing higher effectiveness. The authors concluded that the effectiveness profiles for different nozzle types and coolant Mach numbers collapse to a single profile when the downstream distance is non-dimensionalized by the slot

height and the blowing ratio. The authors also noted that a favorable pressure gradient can improve effectiveness, but did not go on to make any firm conclusions about this effect*.

Hunt, Juhany, and Sivo³ were also motivated by thermal protection for hypersonic engines to study supersonic film cooling with air and helium as coolants. In their study, the core stream was air at Mach 2.44 with injectant Mach numbers ranging from 1.2 to 1.9. The experimental facility was a continuous wind tunnel which allowed them to achieve steady state and use adiabatic temperature values to calculate the film cooling effectiveness. The authors found that increasing the injectant Mach number has a positive effect on film cooling performance and that helium provides superior thermal protection due to its higher specific heat. As observed by Bass, Hardin, and Rodgers⁷, non-dimensionalizing the downstream distance by the slot height and the blowing ratio caused the effectiveness profiles under the different test conditions to collapse to a single line.

Much research into film cooling in supersonic environments has been motivated by thermal protection for sensitive surfaces in high-speed projectiles. Dannenberg⁸ studied the film cooling performance of helium as a coolant over 3-inch diameter hemispheres in a Mach 10 flow. The experimental facility was a shock tunnel which implies a transient measurement of heat flux. This was obtained using the derivative

* Recent work by Dellimore et al.⁵ in subsonic flows shows that whether or not a streamwise pressure gradient improves or degrades film cooling performance depends on whether the velocity ratio is greater or less than 1 (i.e. whether or not you have a wall jet or core-driven situation)

of temperature measurements provided by thermocouples embedded in the surface of the model. The film cooling effectiveness was seen to follow similar trends as in 2-D rectangular tests; there is little or no heat flux near the injection point but it gradually increases with angle/distance. However, the heat flux starts to drop again after a certain angle/distance as the wall becomes parallel to the flow. This ‘turning point’ was seen to occur at an angle of approximately 30° and film cooling was demonstrated to be an effective strategy in reducing the heat load over blunt bodies by a factor of up to 2.5.

Lucas and Golladay⁹, motivated by the same reasons as the present study is, undertook an experiment on the film cooling performance in rocket nozzles. They used nitrogen as a coolant injected near the throat of a JP-4-oxygen rocket motor which was fired in an altitude tank for up to 70 seconds. This was enough time to attain steady-state thermal conditions. The nozzle was insulated and thermocouples were welded to the exterior surface in order to provide the adiabatic temperature distribution of the nozzle wall. The authors found that the thermal protection increased with injectant mass flow rate, as is typical in a film cooling flow. However, the authors also found that a particular injectant flow rate caused an anomalous depression in the adiabatic wall temperatures. This particular value of the flow rate seemed to provide an unusually high amount of thermal protection, the reasons for which were not known. Lastly, the authors stressed the need for careful structural and thermal design of the circular film slot because of its potential to distort due to expansion and compressive stresses in high temperature environments.

In work very similar to the current study, Aupoix et al.¹⁰ conducted experimental and numerical investigations into supersonic film cooling for application in the VULCAIN rocket engine for the Ariane 5 rocket. The experiments were conducted in a continuous supersonic wind tunnel with a core air flow at Mach 2.78 and stagnation temperature 320 K. A cooled film was injected at stagnation temperatures of 125 K and 260 K at Mach 2. The cool film was prepared by evaporating liquid nitrogen into air. Diagnostics included Schlieren, pressure, and temperature measurements.

Schlieren images showed the expansion fan and shock structures typical in a supersonic film cooling flow, as also observed by Goldstein et al⁶. The authors did not present results for film cooling effectiveness, but they provided data on (ideally) adiabatic wall temperature measurements which still allows assessment of film cooling performance. They found that as the film pressure is increased, the thermal protection offered by the film increases, as is typical. Experimental Mach number and stagnation temperature profiles were also obtained and compared with the results from numerical simulations. Several turbulence models were assessed. They found two-equation models to be adequate in predicting the general behavior of the flow, with the So, Zhang, and Speziale model²⁷ providing the best predictions.

Finally, there have been a number of studies investigating the effects of external shock waves on film cooling, i.e. how an external shock impinging on a supersonic mixing layer affects the film cooling effectiveness. Experimental investigations include those conducted by Juhany and Hunt¹¹, and by Kanda, Ono, and Saito¹².

Numerical investigations of this problem have been conducted by Peng and Jiang¹³ and Takita and Masuya¹⁴. The general consensus is that external shock waves tend to decrease film cooling effectiveness by slowing down the film layer and possibly also by encouraging mixing between the film and core streams.

1.4 Previous Work: Heat Flux Measurements

Film cooling studies often require heat flux measurements, and in the current study, transient heat flux measurements are required, for which there are several existing methods^{15,16}. The most common are calorimeter and thin-film gauges.

Calorimeter gauges involve a slug of high-conductivity material like copper embedded in the test surface as illustrated in figure 1.3. As the flow transfers heat to the surface, the temperature of the slug rises. The Biot number²⁸ is the ratio of the rate of heat transfer to the environment to heat transfer within the material and is usually written in terms of the heat transfer coefficient to the environment (h), the thermal conductivity of the body (k) and the characteristic length of the body (L):

$$Bi = \frac{hL}{k} \quad (1-7)$$

The slug in a calorimeter heat flux gage is designed to have a small Biot number.

This means that spatial temperature variations within the slug are small and measuring the temperature –time history at a single point in the slug can be used to determine the thermal energy added to the slug. This method is simple and robust but

preventing heat loss from the slug can be a challenge and the thermal inertia of the slug raises the response time making it less suited for short duration tests.

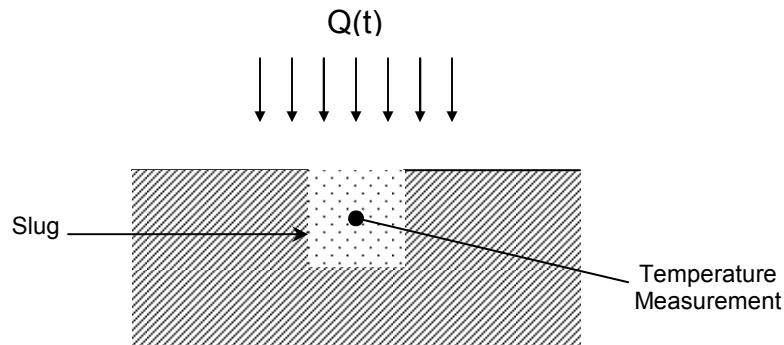


Fig. 1.3: Calorimeter gauge for measuring heat flux.

Another common instrument for measuring transient heat flux is the thin-film gauge. The thin-film gauge is a temperature sensor (thermocouple or thermistor) that is deposited on the test surface as illustrated in figure 1.4. The thin-film gauge provides a temperature-time history of the test surface. If the test surface (wall) is assumed to be semi-infinite, then the heat transfer into the surface can be inferred using a numerical routine¹⁶. This method is popular for very short-duration heat transfer measurements like those needed in shock tunnels. However, fabricating the gauges is non-trivial and the presence of the gauges and wires on the test surface could alter the flows we are trying to investigate. Therefore, film gages are not desirable either.

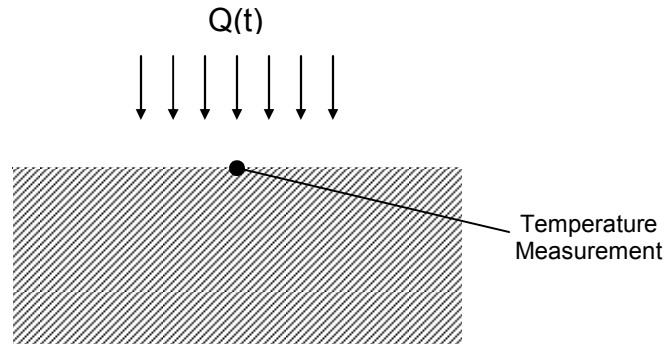


Fig. 1.4: Thin-film gauge for transient heat flux measurement.

Another technique for measuring transient heat flux is to measure the temperature-time history of an internal point in the test surface (wall) (Figure 1.5) and use this along with the one-dimensional conduction equation to infer heat transfer and temperature at the surface^{15,18-23}. This has the advantages of simple fabrication using conventional pre-welded thermocouples, and of leaving the test surface undisturbed. However, these methods are analytically more complex than calorimeter and thin-film gauges, and therefore have seen limited practical use. Therefore, one of the objectives of this work is to further develop this technique and implement it for the first time (to the author's knowledge) in a convective heat transfer study.

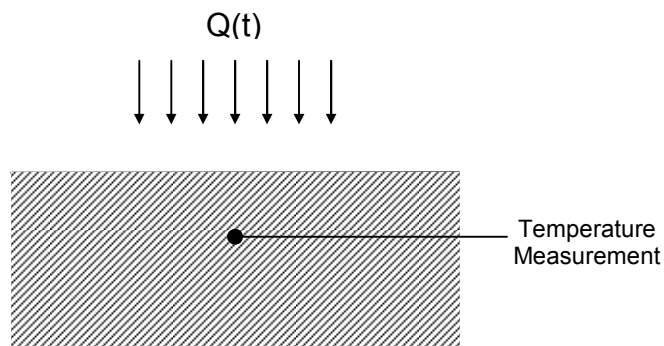


Fig. 1.5: Embedded-temperature sensor for transient heat flux measurement.

1.5 Objectives and Approach

The overall objective of the current study is to design an experimental facility for generating wall heat transfer and flow field data in a canonical film cooling configuration that can be used to validate numerical simulation tools. This will be accomplished through the following steps:

1. Identifying test conditions that – to the extent possible in an atmospheric total temperature and pressure tunnel – maximize relevancy to conditions encountered in the J-2X rocket nozzle extension.
2. Designing and constructing a new nozzle and film cooling test-section for the UMD supersonic wind tunnel.
3. Developing minimally intrusive instrumentation for measuring wall heat flux.
4. Demonstrating the experiment by making preliminary heat flux and shear layer growth rate measurements.
5. Comparing the preliminary measurements to the results of numerical simulations.

Chapter 2: Experiment Design

2.1 Experiment Overview

The basic experiment concept will be described in this sub-section. Film cooling effectiveness is defined as⁴

$$\eta(x) = 1 - \frac{Q(x)}{Q_0} \quad (2-1)$$

where $Q(x)$ is the heat flux on the protected (film-cooled) surface, and Q_0 is the heat flux on the surface without film cooling. Since it is difficult to heat the high-speed and high-volume core flow (because of the cost and safety concerns), the core flow is left unheated and instead the test surfaces and the film flow are heated to the same temperature. This results in heat transfer from the walls to the flow as shown in Fig. 2.1. The hot film prevents heat transfer from the hot wall to the core flow and as the film breaks down, the core flow comes into contact with the hot wall and the heat flux increases. This increase in heat flux implies a decrease in the film cooling effectiveness. While this arrangement reverses the direction of heat transfer from what is seen in a typical film cooling arrangement, it retains the essential fluid physics that are of interest and still allows calculation of film cooling effectiveness.

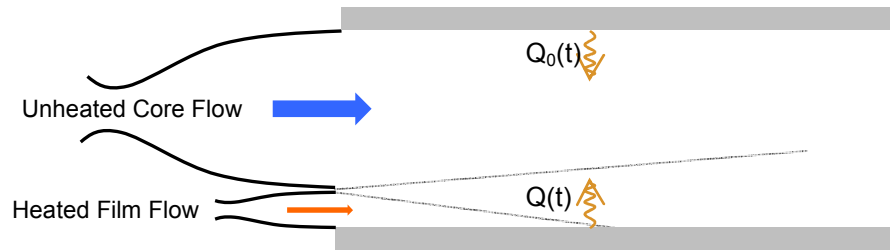


Fig. 2.1: Experiment layout.

Q is provided by the heat fluxes from the lower (film side) wall, and Q_0 is provided by the upper (plain) wall. However, the choice for Q_0 is a bit subjective as one could also consider it to be the heat flux on the lower wall with no film flow. This choice for Q_0 shifts the effectiveness profiles, but the essential trends remain the same.

The basic test procedure is as follows: prior to starting the experiment, the test surfaces are heated to the prescribed temperature. Then the core and film flows are started. As the experiment progresses, the test surfaces lose heat to the flow and the resulting heat transfer rates on both walls are compared to establish an effectiveness profile. More details on the experiment hardware and instrumentation are provided next.

2.2 Selection of Test Conditions

As mentioned earlier, the experiment needs to be as similar to the J-2X engine flow conditions as possible. However, it is not possible to match all of the relevant non-dimensional parameters in a laboratory experiment. Therefore the experiments have been designed to approach these parameters as closely as practically possible within

the total temperature and pressure limitations of the experimental facility (300 K and 1 atm respectively). Heating the high-speed, high-volume core flow (1.33 kg/s) is not a practical option because of the cost and safety concerns (would require 53 kW).

A more practical alternative is to study the inverse heat transfer problem (i.e. the film heating problem) by heating the film flow and the test surfaces. This does not change the essential fluid physics that are of interest in this study and is an approach that has also been used by others⁶. Care is taken to ensure that the test surfaces are heated to the same temperature as the film total temperature so that the wall heat flux is zero at the film louver exit. The heat flux increases as the film breaks down and the hot walls come into contact with the cool core flow. This arrangement enables one to measure the streamwise evolution of film cooling effectiveness while keeping the experiment within practical limitations.

Table 2.1 compares the conditions in the J-2X engine to those in the three planned experiments. Note that the first three experiments are conducted under conditions where the pressure remains approximately constant with downstream distance (Zero Pressure Gradient, ZPG). The last experiment simulates the favorable pressure gradient (FPG) experienced in the actual nozzle. The reasons for why these are reasonable test points are presented next.

Table 2.1: Experiment Test Cases.

	<u>J-2X</u>	<u>Test Case 1</u>	<u>Test Case 2</u>	<u>Test Case 3</u>	<u>Test Case 4</u>
<i>Pressure</i>	FPG	ZPG	ZPG	ZPG	FPG
<i>Gradient</i>					
<i>Core</i>	H2O	Air	Air	Air	Air
<i>Film</i>	H2O, H2	Air	Air	Air	Air
M_∞	3.74	2.40	2.40	2.40	2.40
M_f	1.4	0.50	0.73	1.40	0.73
$T_{0,\infty} (K)$	3767	300	300	300	300
$T_{0,f} (K)$	539	340	340	340	340
$u_\infty (m/s)$	4117	568.0	568.0	568.0	568.0
$u_f (m/s)$	1833	180.4	255.6	438.6	255.6
M_C	1.08	0.65	0.53	0.24	0.53
λ	0.62	0.14	0.2	0.44	0.2
s	1.39	0.43	0.45	0.57	0.45
r	2.22	3.13	2.22	1.30	2.22

Film cooling effectiveness is controlled by the shear layer growth rate so at the most basic level it is important to ensure that the behavior of the shear layer in the experiment will be similar to that expected in the real engine. An analytical model recently developed by Dellimore et al.⁵ to predict growth rates of compressible shear layers was used to generate contour plots of growth rate as a function of velocity ratio and density ratio for the design Mach 2.4 flow of the experiment and the Mach 3.74 flow in the J-2X. The results are shown in Fig. 2.2. The open symbols show the conditions corresponding to the proposed set of experiments while the cross shows

the J-2X engine. Note that the cross in Fig. 2.2a does not indicate shear layer growth rate in the J-2X. It is only used to indicate the velocity ratio and density ratio in the J-2X relative to the experiments. Similarly, the open symbols in Fig. 2.2b do not give the shear layer growth rate in the experiments; they are only used to indicate the velocity and density ratios in the experiments relative to the J-2X. The figures show that while it is possible to match the velocity ratios in the experiment and J-2X, the large difference in total temperature makes it impossible to match the density ratio. However, Fig. 2.2 shows that the non-dimensional growth rate range spanned by the experiments ($0.025 < \delta'_{comp} < \sim 0.06$) is in the same order of magnitude as that expected in the J-2X engine ($\delta'_{comp} \sim 0.08$). Therefore, we expect the shear layer in the experiment to behave in a manner that is similar to its counterpart in the J-2X. The fact that this growth rate changes by approximately a factor of 3 through the different experiments suggests that we ought to see measurably different behavior.

Figure 2.3 makes a similar comparison of convective Mach number as a function of velocity ratio for the experiment and the J-2X engine. Again, the large difference in total temperature makes it difficult to match the convective Mach number. However, the contours have similar shapes in both situations and the convective Mach number is varied by a factor of two through the different experiments so it should be possible to observe relevant differences in behavior in the various proposed experiments.

Lastly, it should be noted that the test cases in Table 2.1 are *design* or *ideal* test cases i.e. the experiments were designed for these test cases assuming ideal flow conditions. However viscous effects and the contour of the supersonic nozzle throat

produced some deviations from the ideal test matrix (Table 2.1) in both the experiments and the simulations. The actual test conditions achieved, while not far from the test matrix in Table 2.1, are described in chapter 4.

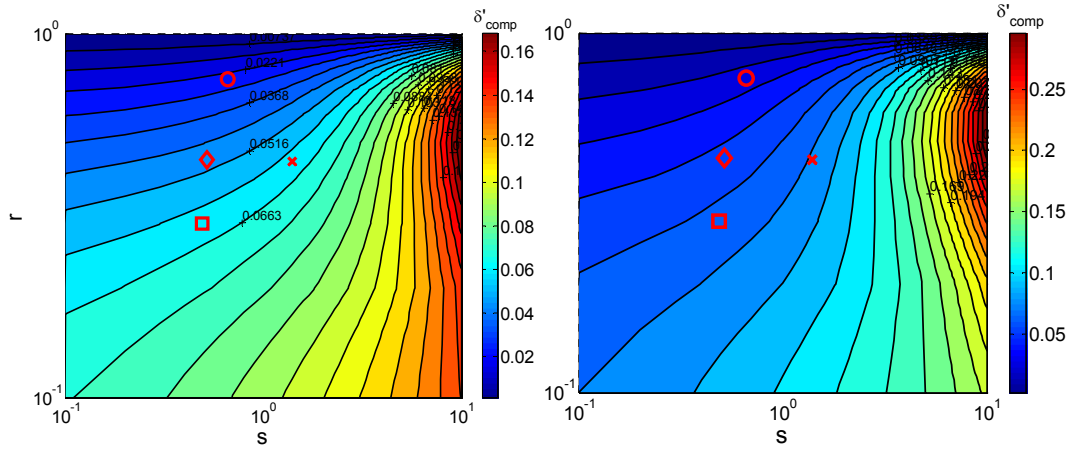
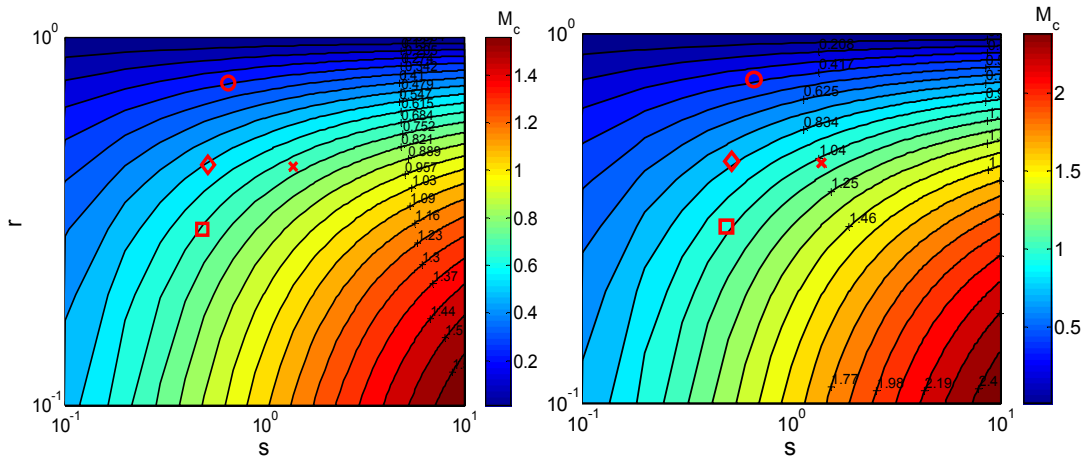


Figure 2.2: Contours of shear layer growth rate in (a) the $M = 2.4$ experiment and (b) the $M = 3.74$ J-2X. (Plots due to K. Dellimore⁵)



to make inferences about film cooling performance in the J-2X engine and why new experiments are required. For example, Goldstein et al.⁶ did not report the velocity ratio or convective Mach number. They also mention that the film was laminar, which is not the case in the J-2X engine. Bass, Hardin, and Rodgers⁷ studied a wall-jet ($r < 1$) whereas the J-2X engine operates in a wall wake configuration. This is important because the effects of pressure gradients and compressibility are completely different in the two cases⁵. The study by Hunt, Juhany, and Sivo³ investigates conditions that are somewhat similar to those encountered in the J-2X engine. However, their study was not comprehensive as no flow visualization was provided. This is important for understanding the underlying physics. Lucas and Golladay⁹ presented results for film cooling a rocket nozzle but provided even less flow field data so it is not clear at all how relevant their experiments are to the J-2X. Lastly, Aupoix et al.¹⁰ presented comprehensive results for an experiment with a convective Mach number and velocity ratio similar to the J-2X engine. However, the blowing ratio is more than an order of magnitude larger than that found in the J-2X engine. Taken together, there appears to be a lack of experimental data describing film cooling performance at conditions that are relevant to the J-2X engine. Therefore, the overall objective of this thesis is to develop an experiment capable of providing film cooling effectiveness measurements that are relevant to the J-2X engine and filling this gap in the literature.

Table 2.2: Summary of existing experimental data.

	M_∞	M_f	M_C	r	λ	Re_∞	Re_f
Goldstein et al. ⁶	3 (air)	1 (air)	Unkno wn	Unkn own	0.412	4×10^5	Unknown

Bass, Hardin, and Rodgers ⁷	3 (air)	2 (H ₂)	0.13	0.89	0.53	1.13 x 10 ⁶	5 x 10 ⁴
Hunt, Juhany, and Sivo ³	2.44 (air)	1.3 - 1.8 (air)	0.28 – 0.31	1.1 – 1.75	0.38 - 0.74	2.3 x 10 ⁵	4.8 x 10 ³
Lucas and Golladay ⁹	~1 (accelerating combustion gases)	<1 (N ₂)	Unkno wn	Unkn own	5.75 – 9.64	Unknown	Unknown
Aupoix et al. ¹⁰	2.78	2	0.73	1.85	9.25	8.9 x 10 ⁵	1.06 x 10 ⁶
Current study	2.4	0.5 - 1.4	0.24 – 0.65	1.3 – 3.13	0.14 – 0.44	9.4 x 10 ⁵	2.13 x 10 ⁴
J-2X	3.74	1.4	1.08	2.22	0.62	-	-

2.3 Modifications to UMD Supersonic Wind Tunnel

The experiments were conducted in the University of Maryland supersonic wind tunnel, which is shown in Figs. 2.4 and 2.5. It is a blowdown facility capable of generating Mach 2+ flows for several seconds through a 6 inch wide rectangular test section. The wind tunnel is connected to a vacuum tank. Prior to starting an experiment, the vacuum tank and wind tunnel section are evacuated by means of a large vacuum pump to a pressure of 2 in Hg. When an experiment is to be started, a pneumatically-actuated butterfly valve upstream of the nozzle section is opened. This

allows air from the atmosphere to flow in through the supersonic nozzle and test section, and finally into the vacuum tank, as shown in Fig. 2.4.

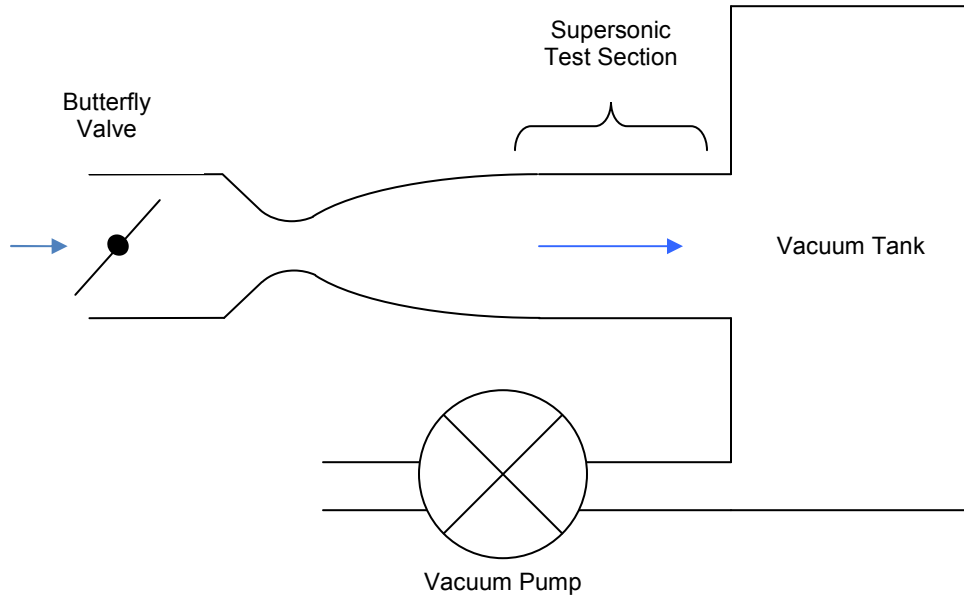


Fig. 2.4: Blowdown wind tunnel.

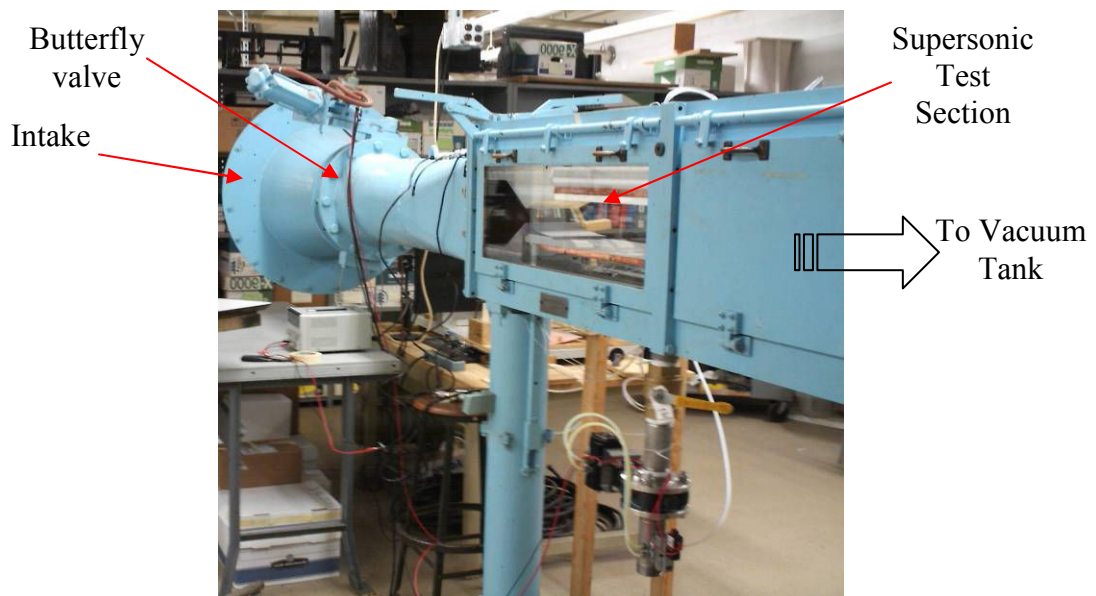


Fig. 2.5: UMD supersonic wind tunnel. Flow is from left to right.

2.4 Component Design

2.4.1 Estimation of Test Time

Using the volume of the vacuum tank (63.8 m^3) and the dimensions of the test apparatus, the tunnel test time was estimated using 1-D gas dynamic equations. The calculation was started by assuming a sub-atmospheric pressure in the vacuum tanks. When the flows initiate, the mass added to the tank determines the pressure rise. The pressure ratio between the atmosphere and the vacuum tanks is then used to determine whether or not supersonic flow can be sustained. The exact test time depends on the initial vacuum pressure in the tanks, the area of the core flow throat, the effective area of the film throat (this could be at the contraction in the louver or in the throttling valve), and atmospheric pressure and temperature. A worst-case calculation where the film throttle area is greater than the film nozzle throat area indicates that it should be possible to sustain supersonic flow for at least 6 seconds.

2.4.2 Test Section Arrangement

The core flow is created using a rectangular convergent-divergent nozzle designed for Mach 2.4 as shown in Fig. 2.6. The nozzle exhaust is 6 inches wide and 3.5 inches high and discharges into the constant-area rectangular test section. The film nozzle is located under the lower wall of the core nozzle and is designed to produce a Mach 1.4 film flowing parallel to the core flow on the lower wall. The film nozzle expands the flow in the spanwise direction (perpendicular to the core nozzle). The film nozzle is also 6 inches wide but 0.25 inches tall (s), and the lip thickness (t) separating the core and film nozzles at their exits is 0.05 inches. The ratio t/s in this study is therefore

0.2, whereas in the J-2X engine it is closer to 1. Fig. 2.7 shows a picture of the installed apparatus.

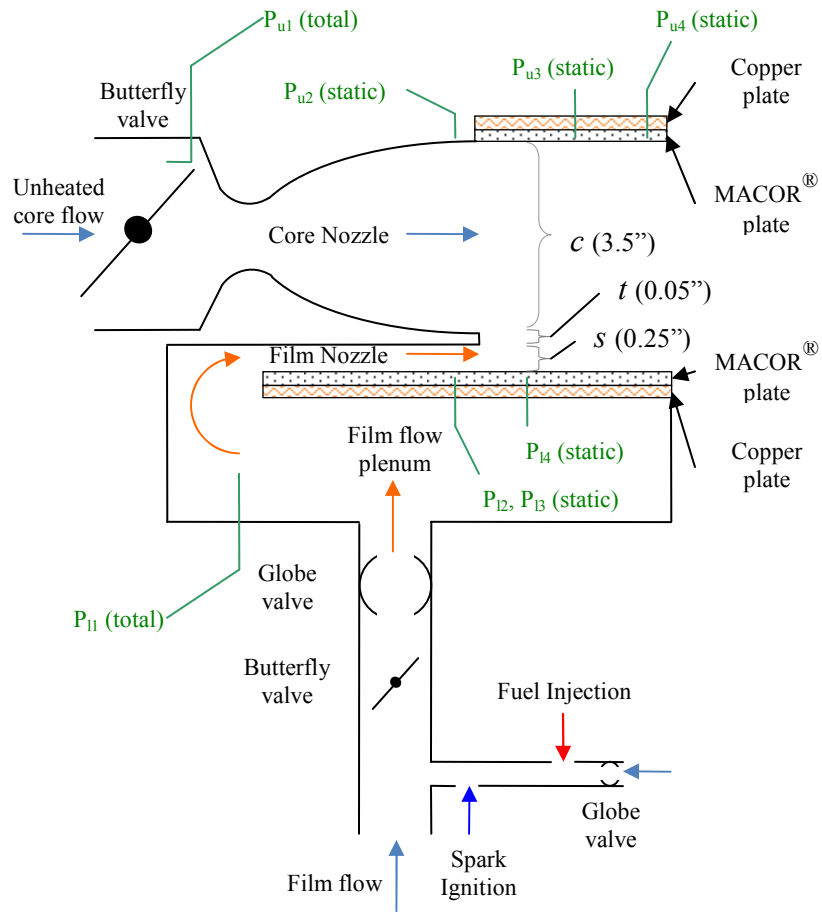


Fig. 2.6: Schematic illustration of test section with pressure instrumentation and their approximate locations.

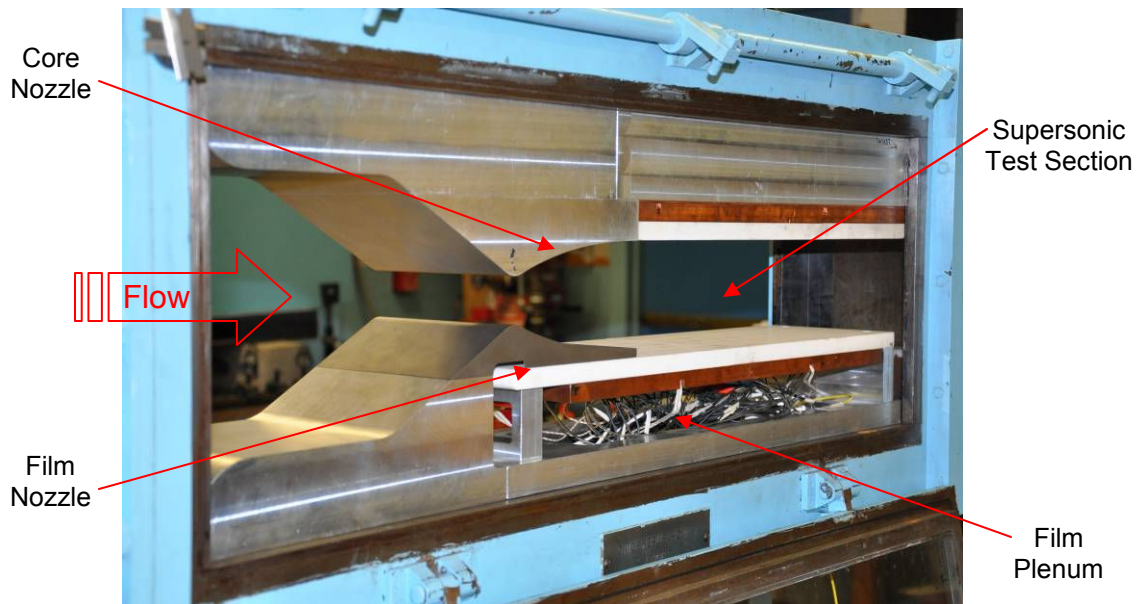


Fig. 2.7: Picture of supersonic test section.

The film flow is drawn from the atmosphere via a secondary opening underneath the test section. As shown in Figs. 2.6 and 2.8, a butterfly valve mounted on a 2" pipe provides on/off operation for the film flow. This valve is also pneumatically actuated and is electrically triggered simultaneously with the core flow butterfly valve. Compressed air is supplied to a solenoid valve which allows the air to open the film butterfly valve when an electric signal is applied to it. This electric signal is applied through the same switch as the core flow, thereby ensuring that the valves open simultaneously. After passing through the butterfly valve, the film flow passes through a globe valve which is used as a throttle to change the film total pressure and therefore the film exit Mach number (in the subsonic regime). Then, the flow enters a plenum under the lower test surface from where it turns upward and is accelerated

through the film nozzle and into the test section. As discussed in section 2.1, the film also needs to be heated, so a propane burner is attached to the film flow intake pipe. This burner is shown in Figs. 2.6 & 2.8, and will be discussed in more detail in section 2.4.5.

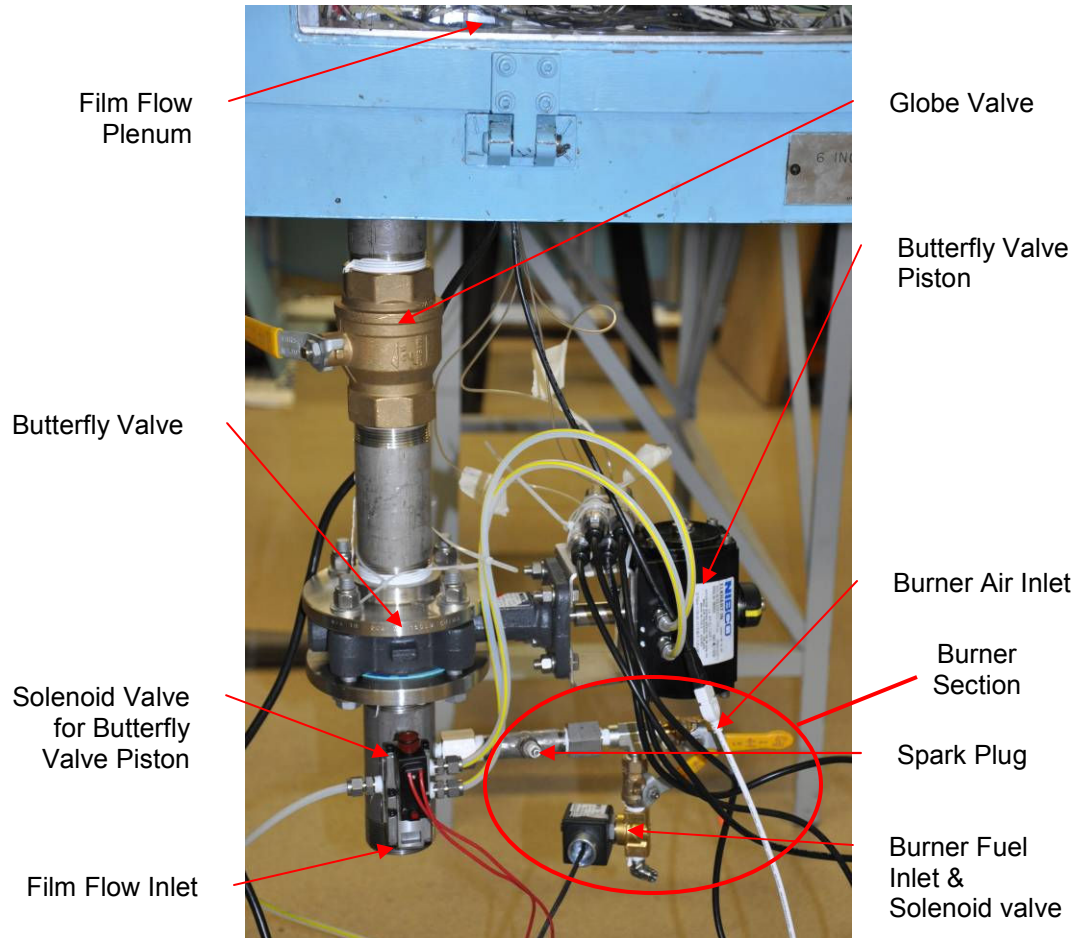


Fig. 2.8: Film flow control apparatus.

2.4.3 Supersonic Contour Design

The supersonic nozzle contours were designed using the method of characteristics (the code is presented in Appendix A). Figures 2.9 and 2.10 show lines of constant

Mach number for the Mach 2.4 and 1.4 nozzles designed for the experiments. This method produced a finite angle at the throat which was dealt with using NASA guidelines³²: the supersonic contour was truncated near the throat and replaced with a circular profile to carry it through to the subsonic section, from where onwards a simple converging section could be used.

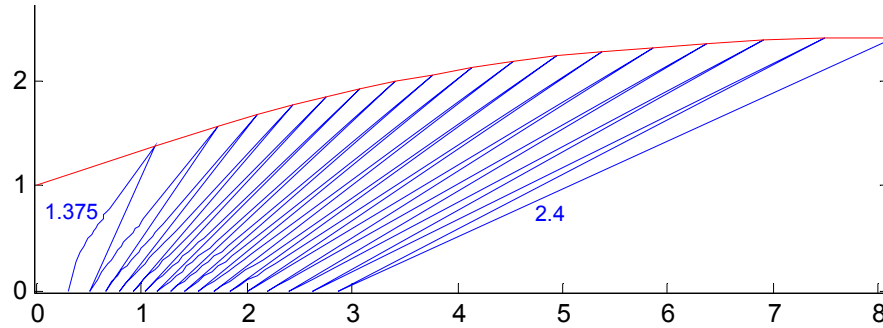


Fig. 2.9: Lines of constant Mach number for the Mach 2.4 core flow nozzle ($\gamma = 1.4$). Every alternate line represents a Mach contour.

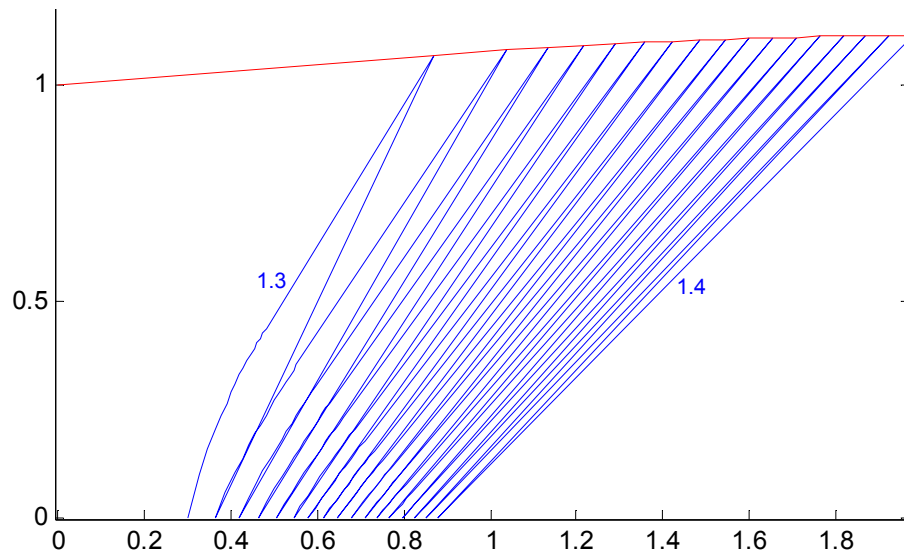


Fig. 2.10: Lines of constant Mach number for the Mach 1.4 film flow nozzle ($\gamma = 1.4$). Every alternate line represents a Mach contour.

2.4.4 Test Surfaces

The test surfaces were made of 0.625 inch thick MACOR[®], a machinable ceramic. The thickness and choice of material was largely driven by the requirement that streamwise and spanwise wall heat fluxes be minimized (so as to permit comparison to CFD simulations that do not consider heat transfer in the wall) and to ensure that the test surface (plate) appears thermally semi-infinite in the wall normal direction over the duration of the experiment (so as to permit the use of the heat flux measurement technique to be described in chapter 3). This means that the test plate thickness and the spacing of heat flux gauges must be greater than the thermal penetration depth so that the thermal wave associated with local heat transfer does not ‘feel’ the effect of the finite depth of the test plate or other sensors around it. The thermal penetration depth is generally defined as the depth at which the difference between the local instantaneous and initial temperatures is 1% of the difference between the surface instantaneous and initial temperatures^{16,17}:

$$\frac{T_{\delta} - T_s}{T_i - T_s} = 0.99 \quad (2-2)$$

In this equation, T_{δ} is the temperature at the penetration depth, T_i is the initial temperature, and T_s is the surface temperature. It can be shown^{16,17} that the semi-infinite condition is achieved if the depth of the plate (or the sensor spacing), d , is at least

$$d \geq 4\sqrt{\alpha t} \quad (2-3)$$

where α is the thermal diffusivity of the plate material and t is the test time. In order to keep the depth of the plate to a practical size and to maximize the spatial resolution of the heat flux measurements (i.e. minimize the gauge spacing), a material with a low thermal diffusivity was required. Furthermore, it was also important that the material be machinable. Table 2.3 lists thermal diffusivities and required minimum depths for several materials.

Table 2.3: Candidate materials for test plates.

Material	α (m^2/s)	d (m)	d (in.)	Comments
Copper	1.12E-04	0.103692	4.082356	Excessive thickness required
Aluminum	8.42E-05	0.089896	3.53921	Excessive thickness required
MACOR [®]	7.30E-07	0.008371	0.329582	
Glass	3.40E-07	0.005713	0.224927	Not machinable
PVC	1.00E-07	0.003098	0.121984	Warps with heating, properties have high temperature dependence

While there are materials other than MACOR[®] that can be used to manufacture a test plate with a practical thickness, other considerations such as machinability and temperature-dependence of thermal properties make MACOR[®] an attractive candidate. In addition, MACOR[®] is a well-established test material for transient heat flux measurements. Given these considerations, 0.625 inch thick MACOR[®] was chosen for the test plates. The test plates are attached to 0.625 inch thick copper plates with embedded electric cartridge heaters as shown in Figs. 2.6 and 2.7. The heated copper plates are intended to provide an (ideally) uniform but adjustable wall temperature boundary condition for the MACOR[®] plates.

2.4.5 Film Heater

Section 2.2 showed that the film flow needs to be heated to 40 K above ambient. Doing this electrically is impractical because electric heaters do not equilibrate quickly enough for the 6 second experiment of interest here. This means that some kind of separate flow system would need to be designed to supply a continuous flow through the heater that could be switched into the wind tunnel louver for 6 seconds and then switched back out. This would be expensive, and potentially unwieldy.

A much simpler approach is to heat the flow using a small propane-fueled burner. An energy balance (eq. 2-4) on the louver flow shows that diverting only 1% of the louver flow through a stoichiometric propane-air burner is sufficient to raise the film temperature by 40 K.

$$\dot{m}_{film} c_p \Delta T = \varphi_s \dot{m}_{burner} \Delta H \quad (2-4)$$

Where φ_s is the stoichiometric air-fuel ratio and ΔH is the heating value of the fuel. Therefore, a film heater was attached to the film flow inlet as shown in Figs. 2.6, 2.8, and 2.11. Propane stored in an external tank mixes with the incoming air in a short tube and is ignited by a spark plug sparking at 200 Hz. Both the propane and air inlets can be throttled with ball valves. The propane flow is switched on and off by a solenoid valve on the same electrical circuit as the core and film butterfly valves - this allows all flows to be initiated simultaneously, but the spark plug is controlled by a different switch which is turned on before the experiment is started.

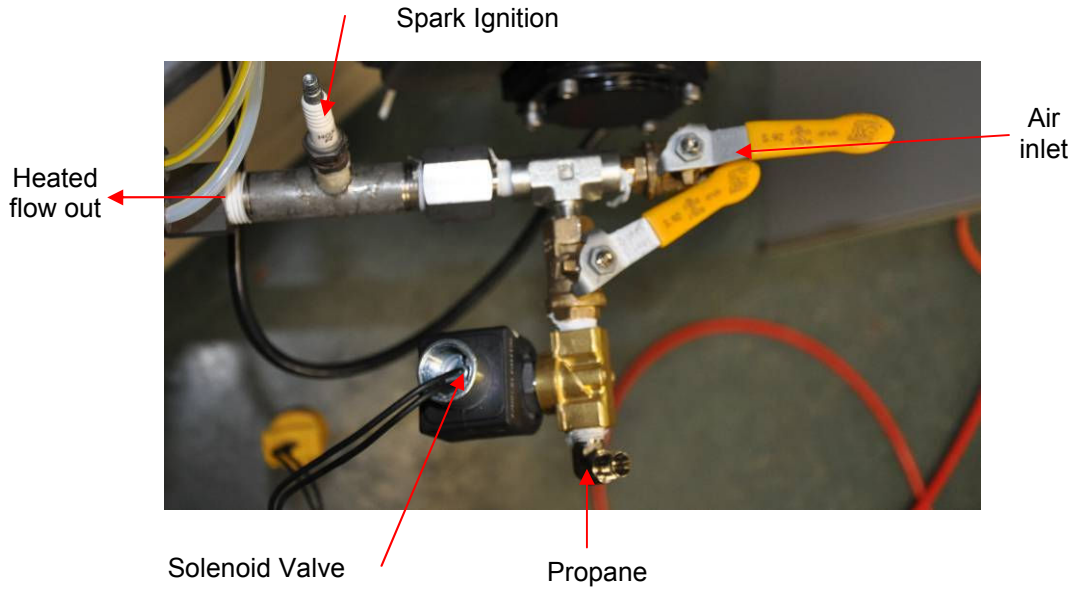


Fig. 2.11: Film heater.

One concern with the combustion-based approach to film heating is how the composition and specific heat capacity of the film flow are affected. This is important because we want to compare to computational results based on air. Assuming 4 constituents (N_2 , O_2 , CO_2 , H_2O) and that 1% of the incoming air is combusted stoichiometrically (Eq. 2-5), Table 2.4 gives the pre and post-combustion composition and specific heat capacity of the film flow.

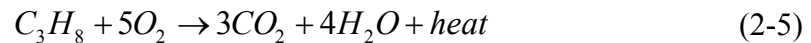


Table 2.4: Pre and post-combustion composition of film flow.

	Pre-combustion (dry air), composition by mass	Post-combustion, composition by mass	% Change
N_2	75.45%	75.40%	-0.05%

O ₂	23.16%	22.83%	-0.33%
CO ₂	0.05%	0.31%	0.26%
H ₂ O	0%	0.14%	0.14%
Heat Capacity, c _p (J/kg-K)	1000.3	1001.8	0.15%

Table 2.4 shows that the changes in composition and heat capacity are very small. Therefore, the combustion-based heater should have a minimal impact on the composition and heat capacity of the film flow and it will still be possible to compare the experimental results to CFD simulations.

2.5 Instrumentation

2.5.1 Heat Flux Measurement

As described in chapter 1, an embedded temperature-sensor heat flux gauge is chosen for this experiment because it offers minimal disturbance to the test surface and can be fabricated using pre-welded thermocouples. Implementing this technique requires one to solve the inverse heat transfer problem – i.e. inferring heat flux from temperature-time data as opposed to inferring temperature-time from heat flux – when the walls are not initially isothermal (because the heated walls will likely be losing heat to the wind tunnel structure and environment). The challenge is that most known inverse problem solutions cannot be used with initially non-isothermal walls and the remaining few that can are so complex that they are effectively unusable by all but the people who developed them. Therefore, it is necessary to develop our own simpler solution to the inverse problem under initially non-isothermal conditions.

How this is accomplished is described in detail in the next chapter. The location and fabrication of the embedded gauges is described here.

The ideal location for the temperature sensors is as close to the surface as possible so as to produce the maximum change in sensed temperature. However, fabrication and robustness considerations limit the minimum practical depth below the surface at which the sensors can be placed. If the sensor is too deep, the temperature change will be too small to measure accurately. If the sensor is too close to the surface, it may not be possible to machine the hole without breaking through the surface and the thin surface over the sensor is weak and therefore vulnerable to damage. A combination of analytical and numerical methods is used in Chapter 3 to establish that a depth of 0.050 inches strikes a suitable compromise between mechanical reliability and response. However, it will be learned experimentally that 0.050 in is probably too small as aerodynamic loads associated with startup caused several sensors to break.

A heat flux gauge was fabricated by drilling a 0.5 inch diameter hole in the MACOR[®] plate from underneath to a depth which would leave 0.05 inches between the hole end and the test surface, as shown in Fig. 2.12. Then, a MACOR[®] cylinder was fabricated to plug this hole. This cylinder had a groove, or chase, around it to accommodate thermocouple wire. T-type unsheathed butt-welded thermocouple wire (Omega COCO-010-BW) was then wrapped through the groove around this MACOR[®] plug, and the plug was inserted into the hole in the test plate. This placed the thermocouple junction at the prescribed depth inside the MACOR[®] plate. Thermaltake TG-2

Thermal grease with thermal conductivity 1.5 W/m-K (which is within 10% of that of MACOR[®]) was used to fill any possible voids so as to create a continuous thermal medium. A copper heating plate was bolted to the bottom of the MACOR[®] test plate and holes drilled in the copper plate permitted the thermocouple wires to pass through. The thermocouple wires were then insulated with heat-shrink tubing to avoid any contact with the copper heating plate and other metal.

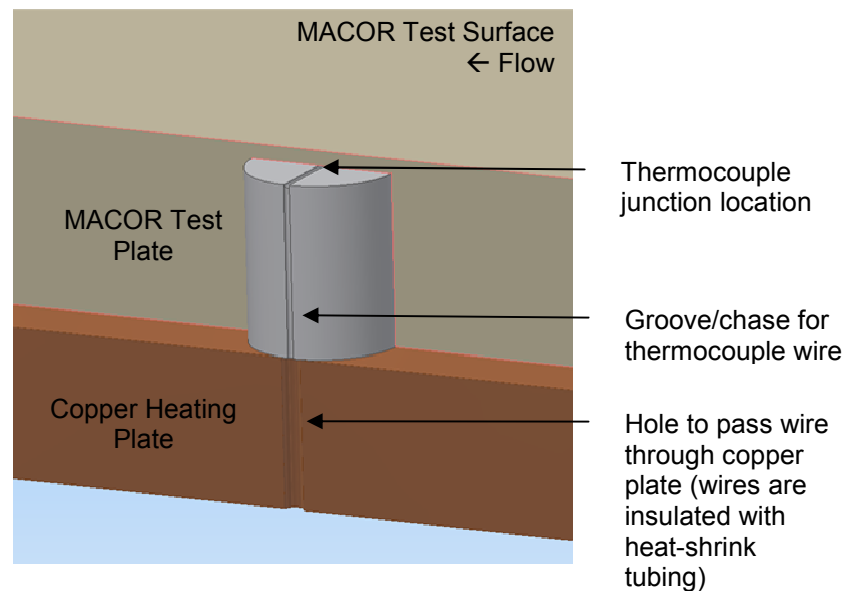


Fig. 2.12: Cross-section of the wall showing the components of the embedded heat flux gauge.

The heat flux gauges were installed on both the upper and lower walls at various streamwise locations as shown in Fig. 2.13. While most of the gauges were installed at the centerline, a few were installed off-centerline to check for 3-dimensional effects. More sensors were placed on the lower wall than on the upper wall, because the heat flux behavior on the lower wall was expected to change with distance unlike the upper wall, and the increased sensor density is meant to capture these trends. On

the lower wall itself, the sensor density is increased in the region between 10 and 40 slot heights because this is where the most pronounced change in heat transfer is expected (due to the lower edge of the shear layer impinging on the wall) based on numerical and semi-empirical results⁵. Table 2.5 gives the location, data acquisition (DAQ) channel, and status of the sensors.

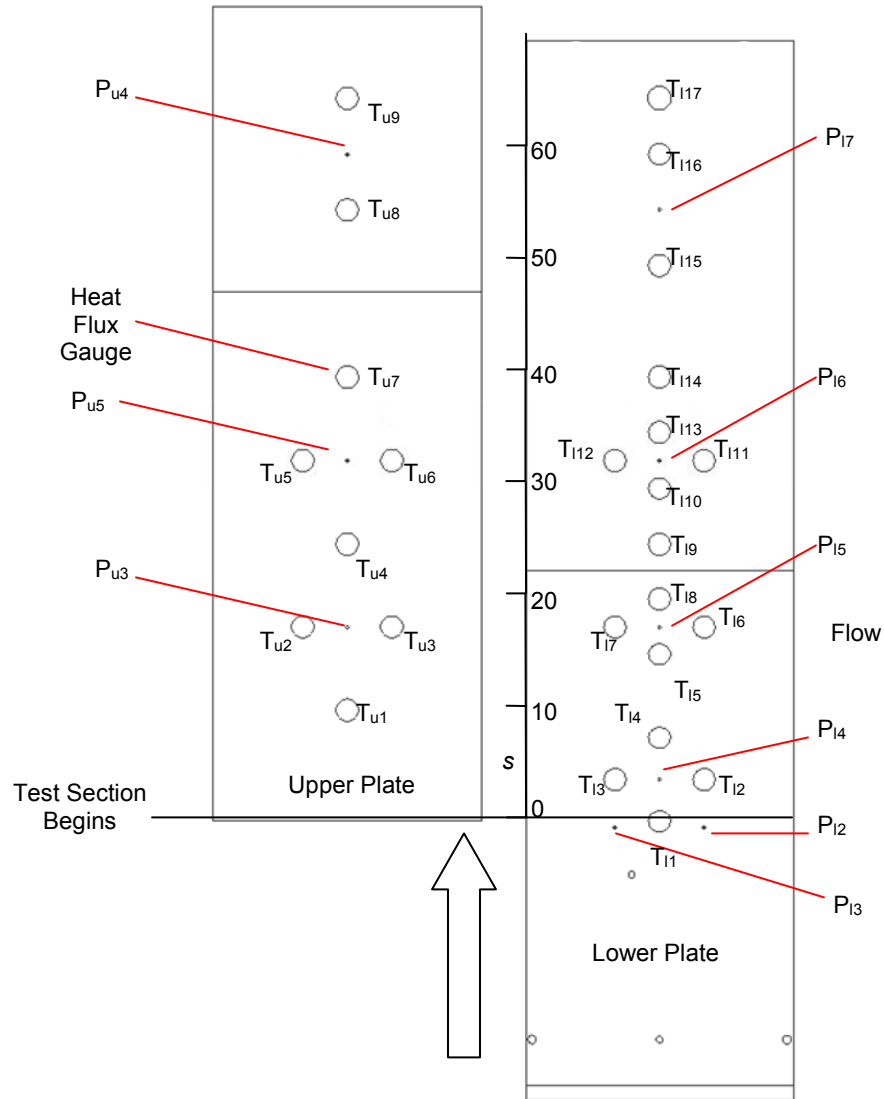


Fig. 2.13: Plan views of the upper and lower plates showing the locations of the heat flux gauges (largest circles) and the pressure taps (smallest circles/dots) with a scale indicating slot heights. The intermediate size circles are bolt holes.

Table 2.5: Sensor details

Sensor	Location (x/s)	DAQ channel	Status
T ₁₁	0	NI-9213-0	Active
T ₁₂	3.75	NI-9213-1	Active
T ₁₃	3.75	NI-9213-2	Active
T ₁₄	7.5	NI-9213-3	Active
T ₁₅	15	NI-9213-4	Active
T ₁₆	17.5	-	Not connected
T ₁₇	17.5	-	Not connected
T ₁₈	20	NI-9213-5	Damaged
T ₁₉	25	NI-9213-6	Active
T ₁₁₀	30	NI-9213-7	Active
T ₁₁₁	32.5	NI-9213-8	Active
T ₁₁₂	32.5	NI-9213-9	Active
T ₁₁₃	35	NI-9213-10	Active
T ₁₁₄	40	NI-9213-11	Active
T ₁₁₅	50	NI-9213-12	Active
T ₁₁₆	60	NI-9213-13	Active
T ₁₁₇	65	NI-9213-14	Active
P ₁₂	-0.6	NI-9205-5	Active
P ₁₃	-0.6	NI-9205-6	Active
P ₁₄	3.75	NI-9205-7	Active
P ₁₅	17.5	-	Not connected
P ₁₆	32.5	-	Not connected
P ₁₇	55	-	Not connected
T _{u1}	10	NI-9213-0	Damaged
T _{u2}	17.5	NI-9213-1	Active
T _{u3}	17.5	NI-9213-2	Active
T _{u4}	25	NI-9213-3	Active
T _{u5}	32.5	NI-9213-4	Active
T _{u6}	32.5	NI-9213-5	Damaged
T _{u7}	50	NI-9213-6	Damaged
T _{u8}	55	NI-9213-7	Damaged
T _{u9}	65	NI-9213-8	Active
P _{u3}	17.5	NI-9205-2	Active
P _{u4}	60	NI-9205-3	Active
P _{u5}	32.5	-	Not connected

During the course of the experiments, a few heat flux gauges developed surface cracks that caused the upper MACOR[®] surface to fail in the high speed flow. One such example is shown in Fig. 2.14, where the surface has been swept away to reveal

the thermocouple embedded in the material. The grey appearance is due to the thermal grease. In subsequent experiments, these damaged gauges were filled with *Bondo*, a filler material, to smooth out the surface and the data from these gauges was discarded.



Fig. 2.14: Photograph of a damaged heat flux gauge showing the embedded thermocouple and the MACOR plug covered with gray thermal grease. This ‘divot’ was filled with *Bondo* to restore the smooth surface but the data from the sensor was discarded.

2.5.2 Pressure Measurement

Several total and static pressure measurements were made to ascertain the core and film flow Mach numbers, and to measure the strength of any shocks. A total pressure measurement (P_{u1}) was made in the core flow downstream of the butterfly valve, but

upstream of the contraction, as shown in Fig. 2.6. Three static pressure taps (P_{u2}) were located at the core nozzle exit on the upper wall in the spanwise direction to measure the core exit Mach number and also to assess 3-dimensional effects which were determined to be small. Additional static pressure taps (P_{u3} and P_{u4}) on the upper wall, as shown in Figs. 2.6 & 2.13, were used to verify that the flow Mach number remained approximately constant through the length of the test section.

A total pressure measurement in the film plenum (P_{11}) in combination with static pressure measurements at the film nozzle exit (P_{12} and P_{13}) as shown in Figs. 2.6 & 2.13, were used to determine the film injection Mach number. An additional static pressure tap (P_{14}) shown in Figs. 2.6 & 2.13, located 3.75 slot heights from the injection point, was used to observe the pressure variation in the film stream. The pressure tap holes were connected with epoxy to steel tubes on the back side of the test plate. Plastic tubing was then used to connect these steel tubes on the back of the test plate, to steel tubes in a feed-through (figs. 2.16 and 2.18) to pass the pressure lines out of the wind tunnel. Plastic tubing was again used to connect the steel tubes from the feed-throughs to the pressure transducers. For all pressure measurements Omega PX309-015A5V voltage output absolute pressure sensors with a sensing range of 0 – 15 psia were used.

2.5.3 Schlieren Imaging

Schlieren imaging was also used to visualize shear layers and shock structures. Both sides of the wind tunnel test section are sealed by windows. Figure 2.15 is a top view of the optical system used to collect Schlieren images. A point light source is

provided by a Spectra-Physics mercury vapor lamp. The source is placed at the focal point of a parabolic mirror (M1; $f = 60$ in.) thereby creating a collimated beam that passes through the test section. The light is collected by a second parabolic mirror (M2, $f = 80$ in.) that focuses over the aperture of a digital SLR camera (Nikon D90 with a Nikkor f 20-120 lens), which collects 1024 x 580 images at 30 Hz. In this setup, the aperture (or iris) of the camera acts as the knife-edge, and the CCD sensor acts as the screen.

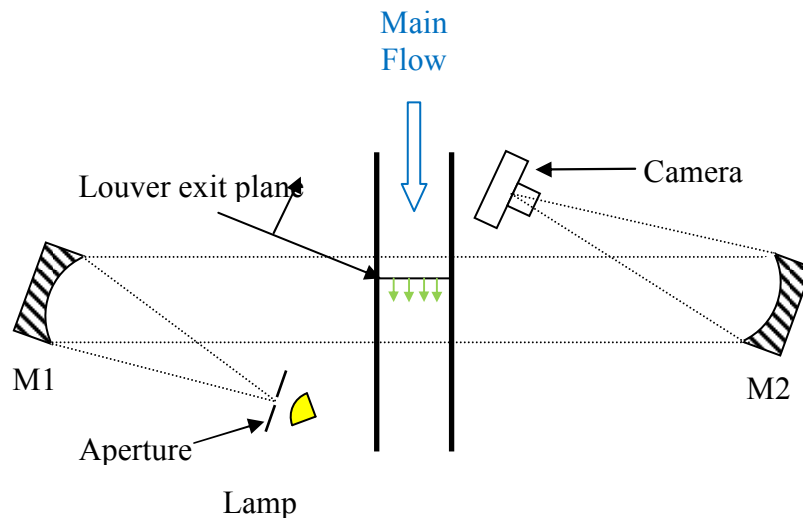


Fig 2.15: Schlieren imaging setup.

2.5.4 Data Acquisition

The data acquisition system consisted of a Lenovo R500 PC running NI LabView 8.6 with separate chassis and modules for heat flux and pressure sensors, as shown in Fig. 2.16.

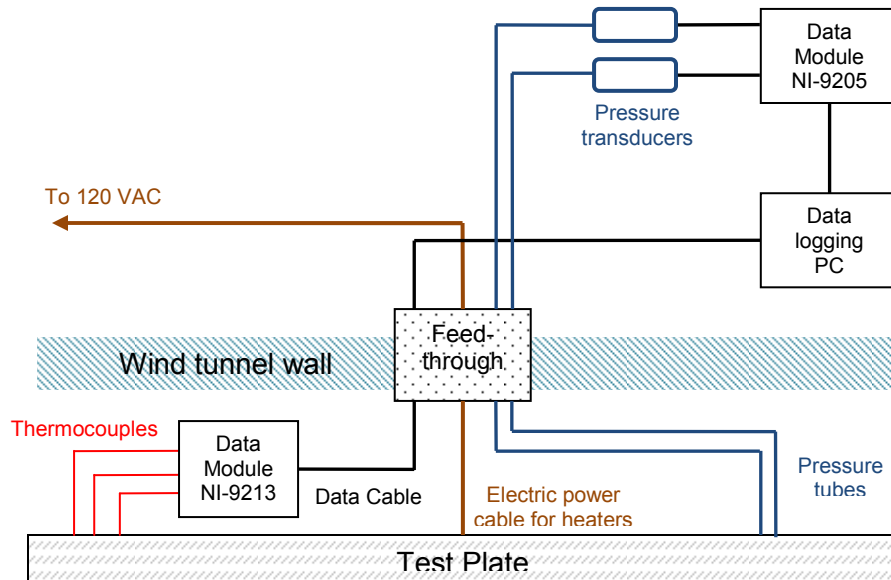


Fig. 2.16: Schematic for data acquisition setup.

The wires from the heat flux gauge thermocouples were led to a compact data acquisition module (NI-9213 mounted on NI USB-9162) which was small enough to fit inside the wind tunnel, shown in Fig. 2.17. This data acquisition module communicates with the host computer via a single USB cable which passes through the tunnel wall via the airtight feed-through shown in Fig. 2.18. The wires, tubes, and data acquisition modules were tucked away in a cavity above the upper test plate (Fig. 2.17) and in the film flow plenum for the lower plate (Fig. 2.7). The temperature data was sampled at 100 Hz for each sensor.

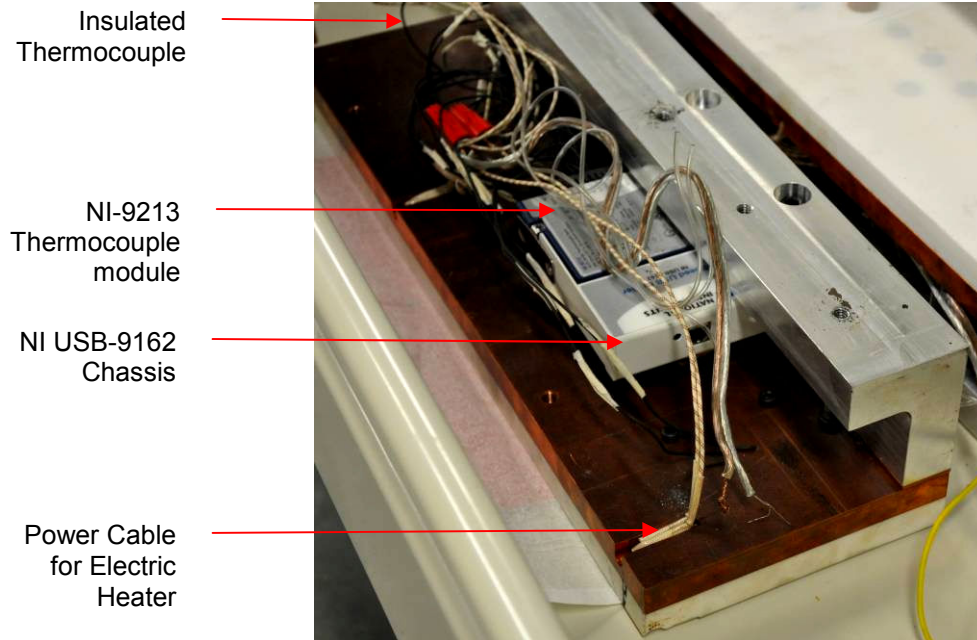


Fig. 2.17: Open section of upper wall assembly showing data acquisition arrangement for thermocouples. The silver bar is one of two structural components that attach the assembly to the wind tunnel wall.

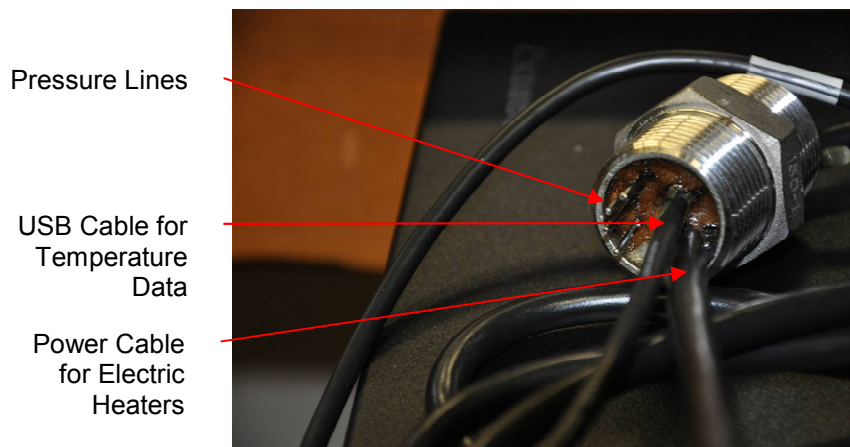


Fig. 2.18: Pressure, USB and electric power cable feed-through.

Tubes from the pressure taps pass out of the tunnel via 2 feed-throughs, one in the upper and lower tunnel walls each, and into the externally-located pressure transducers. The pressure readings were sampled using an NI cDAQ-9178 with NI 9205 modules at 500 Hz (to produce the smallest whole number sampling time permitted by the hardware), and the data was logged on a Lenovo R500 PC using NI LabView 8.6.

Chapter 3: Inverse Measurement of Heat Flux

3.1 Introduction

‘Inverse’ heat flux measurements refer to the process of inferring surface heat flux from a temperature-time history measured somewhere inside the body undergoing heat transfer. While there are several methods for determining the surface heat flux from an internal temperature-time history, all have some numerical aspect. Some are based on numerical integration in a finite-differencing scheme^{18,19}. Others involve curve-fitting the temperature data to a particular functional form²⁰⁻²³ which is a known solution to the 1-D unsteady conduction problem.

Most of these methods are quite complex and therefore have seen limited practical use. For this reason, the relatively practical curve-fitting method of Chen, Chiou, and Thomsen^{20,22} was chosen for this study. The existing method assumes an initially isothermal wall. However, the walls in the experiment may not be initially isothermal because of heat loss to the environment and wind tunnel structure. While there are inverse methods that can account for an initial temperature gradient¹⁹, these methods are too complicated to be practical. Therefore, it is necessary to expand the more practical method of Chen, Chiou, and Thomsen^{20,22} to accommodate a non-isothermal initial wall condition, which is often seen in experimental work. The technique for adapting the method of Chen, Chiou, and Thomsen^{20,22} to an initially non-isothermal

wall is described next. However, this method is also applicable to the other curve-fitting based interpretation methods.

3.2 Inverse Measurement Technique

3.2.1 Case of Uniform Initial Wall Temperature

Chen and Chiou²² considered the situation illustrated in Fig. 3.1, where a semi-infinite wall at an initially uniform temperature (i.e. $T(x, 0) = \text{constant}$) is suddenly exposed to an unknown unsteady heat flux $q(t)$ at the surface. The objective is to infer the surface heat flux from the temperature-time history at a point x_1 units below the surface.

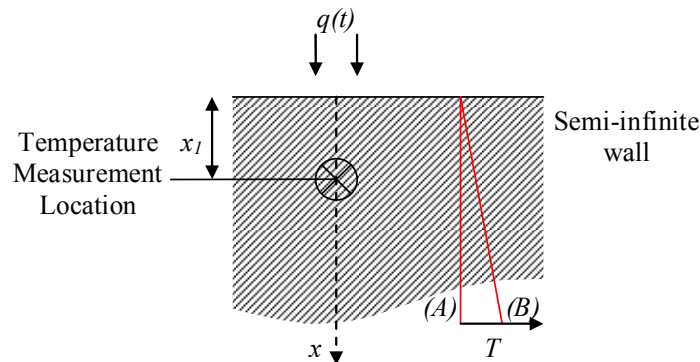


Fig. 3.1: Problem Schematic. Shown above is arbitrary heat flux into a semi-infinite wall and the internal temperature measurement location. Also shown are the two initial temperature distributions under consideration: (A) uniform initial temperature, and (B) initial temperature gradient.

The unsteady heat equation describes the temperature distribution in the solid:

$$\frac{\partial T}{\partial t} = \alpha \frac{\partial^2 T}{\partial x^2} \quad (3-1)$$

Chen and Chiou²² defined the following non-dimensional variables:

$$\tau \equiv \frac{\alpha t}{x_1^2} \quad X \equiv \frac{x}{x_1} \quad \theta \equiv \frac{T - T_0}{T_0} \quad (3-2)$$

where α is the thermal diffusivity of the material and T_0 is the initial temperature.

Using the new variables, the heat equation and initial conditions become

$$\frac{\partial \theta}{\partial \tau} = \frac{\partial^2 \theta}{\partial X^2} \quad (3-3)$$

$$\theta(X, 0) = 0 \quad \theta(1, \tau) = f(\tau) \quad \theta(\infty, \tau) = 0 \quad (3-4)$$

Using a Laplace transform technique, they showed that if the temperature-time history can be fitted to the following function:

$$f(\tau) = \sum_{n=1}^N b_n (4\tau)^n \Gamma(n+1) i^{2n} \operatorname{erfc}\left(\frac{1}{2\sqrt{\tau}}\right) \quad (3-5)$$

(where i^n represents a repeated integral, and N is the number of terms set by the user.

In general, more terms imply higher accuracy but at computational cost) then the coefficients, b_n (which are determined using a curve-fitting routine), can be used to determine the non-dimensional surface temperature and temperature gradient:

$$\theta(0, \tau) = \sum_{n=1}^N b_n \tau^n \quad (3-6)$$

$$-\frac{\partial\theta(0,\tau)}{\partial X} = \sum_{n=1}^N b_n \tau^{n-1/2} \frac{\Gamma(n+1)}{\Gamma(n+1/2)} \quad (3-7)$$

The dimensional surface temperature and heat flux are then given by

$$T_s = T_0 (1 + \theta(0, \tau)) \quad (3-8)$$

$$q = -\frac{kT_0}{x_1} \frac{\partial\theta(0,\tau)}{\partial X} \quad (3-9)$$

where k is the thermal conductivity of the material. The derivation of these results is given in Appendix B.

3.2.2 Case of Initial Temperature Gradient

Now, assume that the initial wall temperature profile is linear. The temperature distribution takes the following form:

$$T(x,0) = T_0 + ax \quad (3-10)$$

where T_0 is the initial surface temperature and a is a constant. Now let

$$\psi \equiv \frac{T - (T_0 + ax)}{T_0} \quad (3-11)$$

ψ also satisfies the governing equation for unsteady heat conduction. Hence,

$$\frac{\partial\psi}{\partial\tau} = \frac{\partial^2\psi}{\partial X^2} \quad (3-12)$$

The initial conditions for the problem remain

$$\psi(X,0) = 0 \quad \psi(1,\tau) = f(\tau) \quad \psi(\infty,\tau) = 0 \quad (3-13)$$

Since the governing equation, initial conditions, and boundary conditions transform to the same problem studied by Chen and Chiou²², their solution can be used directly by substituting ψ for θ . The differences are that ψ must now be curve-fitted instead of θ and that a correction term must be added when solving for the dimensional value of the surface heat flux. The surface temperature and heat flux in dimensional terms are given by

$$T_s = T_0(1 + \psi(0,\tau)) \quad (3-14)$$

$$q = -\frac{kT_0}{x_1} \frac{\partial \psi(0,\tau)}{\partial X} - ak \quad (3-15)$$

To conclude, the procedure for determining the surface heat flux associated with a measured subsurface temperature-time history when the wall is not initially isothermal is as follows:

1. Convert the temperature-time history into ψ - τ history where the value for x in ψ is x_1 , the sensor distance.
2. Curve-fit the ψ - τ history to the form suggested by Chen and Chiou²² (Eq. 3-5).
3. Use the coefficients, b_n , to determine ψ and $d\psi/dX$ at the surface using Eqs. (3-6) and (3-7).
4. Recover the dimensional quantities using Eqs. (3-14) and (3-15).

3.2.3 Note on Implementation

In order to implement the aforementioned technique, a numerical curve-fitting (optimization) routine must fit the temperature-time data from the sensor to the form given by Eq. (3-5). This involves a repeated integral, i^n , which is defined as follows for an arbitrary function $g(x)$:

$$i^n g(x) = \int_0^x \int_0^{u_{n-1}} \dots \int_0^{u_1} g(u) du \dots du_{n-2} du_{n-1} \quad (3-16)$$

In this case, $g(x)$ is the complementary error function. Evaluating Eq. (3-16) and incorporating this into an iterative routine is both challenging and impractical from a computational perspective because it requires the numerical evaluation of several (depending on the number of terms) nested integrals in each iteration. The expression can be reduced to a single integral using Cauchy's formula but there is an even more convenient form for the particular repeated integral in Eq. (3-5): the repeated integral of the error function can be written explicitly in terms of the confluent hypergeometric function²⁴, M , for which explicit numerical routines are commonly available:

$$i^n erf(z) = e^{-z^2} \left[\frac{1}{2^n \Gamma\left(\frac{n}{2} + 1\right)} M\left(\frac{n+1}{2}, \frac{1}{2}, z^2\right) - \frac{z}{2^{n-1} \Gamma\left(\frac{n+1}{2}\right)} M\left(\frac{n}{2} + 1, \frac{3}{2}, z^2\right) \right] \quad (3-17)$$

(note that $erf(z) = 1 - erfc(z)$) While use of the confluent hypergeometric function significantly reduces the complexity of the code and computational time, it is still

impractical for a personal computer to calculate Eq. (3-16) at each iteration of the optimization routine. To further increase the efficiency of the calculation, note that

$$f(\tau) = \sum_{n=1}^N b_n d(n, \tau) \quad (3-18)$$

where

$$d(n, \tau) = (4\tau)^n \Gamma(n+1) e^{-2n} \operatorname{erfc}\left(\frac{1}{2\sqrt{\tau}}\right) \quad (3-19)$$

Equation (3-19) is the computationally expensive term but since it serves as a basis function in equation (3-18), the values of $d(n, \tau)$ only need to be calculated once. These values are stored in an array for use by the optimization routine which determines the values of b_n . This enables the fitting procedure to be performed in an economical manner suitable for a personal computer.

The curve-fitting process itself has to be implemented through an optimization routine, for example `fminsearch` in MATLAB. The details of the curve-fitting routine will depend on the numerical solver and the preferences of the user, but sample code for MATLAB is provided in Appendix C.

3.3 Transient Convection

Lastly, an equation for the transient temperature distribution in a wall undergoing convective heat transfer with an initial temperature gradient is derived. This is useful in determining how an initial gradient can impact the surface heat flux as well as

embedded sensor readings, which are important to know when designing such gauges. This equation therefore allows the assessment of errors which can arise in surface heat flux due to an initial temperature gradient, if one is assuming an initially isothermal wall.

3.3.1 Wall Temperature Distribution with Initial Temperature Gradient

The development of the expression for the temperature distribution in a wall undergoing transient convection with an initial temperature gradient (Fig. 3.2) follows the same general steps presented by Carslaw & Jaeger²⁵ in their solution for the temperature distribution in an initially isothermal wall. The basic idea is to transform the problem into one with a known solution: a semi-infinite solid with an initial non-zero uniform temperature and zero surface temperature. The transformation is a two step procedure.

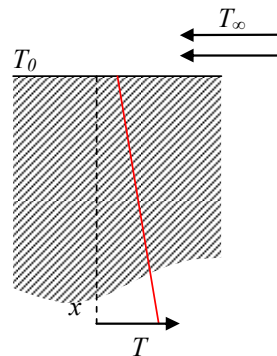


Fig. 3.2: Surface convection with an initial temperature gradient.

The first step is to re-scale the wall temperature in terms of the gas temperature (T_∞), the initial gradient (a), and distance, by introducing a new variable, v :

$$v = T - (T_\infty + ax) \quad (3-20)$$

It can be shown that v satisfies the transient heat conduction equation (Eq. 3-1):

$$\frac{\partial v}{\partial t} = \alpha \frac{\partial^2 v}{\partial x^2} \quad (3-21)$$

The initial temperature distribution is still given by Eq. (3-10) and the boundary condition is given by an energy balance at the surface. So, the initial and boundary conditions are

$$v(x,0) = T_0 - T_\infty \quad (3-22)$$

$$\frac{\partial v(0,t)}{\partial x} = \frac{h}{k} v(0,t) - a \quad (3-23)$$

It is convenient to introduce another temperature variable, ϕ :

$$\phi = v - \frac{k}{h} \frac{\partial v}{\partial x} - \frac{k}{h} a \quad (3-24)$$

This also satisfies the unsteady heat conduction equation;

$$\frac{\partial \phi}{\partial t} = \alpha \frac{\partial^2 \phi}{\partial x^2} \quad (3-25)$$

The initial and boundary conditions become

$$\phi(x,0) = T_0 - T_\infty - \frac{k}{h} a \quad (3-26)$$

$$\phi(0,t) = 0 \quad (3-27)$$

and the problem has been transformed into one of a semi-infinite plate with zero surface temperature and a *uniform* initial temperature distribution. The solution to this problem is given by Carslaw & Jaeger²⁵ and can be used directly to write:

$$\phi(x,t) = \frac{2}{\sqrt{\pi}} \left[T_0 - T_\infty - \frac{k}{h} a \right] \int_0^{\frac{x}{2\sqrt{\alpha t}}} e^{-u^2} du \quad (3-28)$$

The definition of ϕ , after some rearrangement, is used to solve for v :

$$\frac{\partial v}{\partial x} - \frac{h}{k} v + \left(\frac{h}{k} \phi + a \right) = 0 \quad (3-29)$$

This is a 1st order differential equation with the solution

$$v = -e^{\frac{h}{k}x} \int_{\infty}^x e^{-\frac{h}{k}\xi} \left(\frac{h\phi}{k} + a \right) d\xi + C e^{\frac{h}{k}x} \quad (3-30)$$

The constant C is determined by noting that the body is semi-infinite. So, as $x \rightarrow \infty$, $v \rightarrow T_0 - T_\infty$. Since the value of v is bounded, C must be zero. Simplifying Eq. (3-30) gives

$$v = -\frac{h}{k} e^{\frac{h}{k}x} \int_{\infty}^x \phi e^{-\frac{h}{k}\xi} d\xi + \frac{k}{h} a \quad (3-31)$$

The first term corresponds to the convection problem for a uniform initial temperature wall while the second term is new and arises from the initial temperature gradient.

The first integral has been evaluated by Carslaw & Jaeger²⁵ and can be used directly.

Inserting their solution into Eq. (3-31) gives the expression for v :

$$v = \left(T_0 - T_\infty - \frac{k}{h} a \right) \left\{ \operatorname{erf} \left[\frac{x}{2\sqrt{\alpha t}} \right] + e^{\frac{hx}{k} + \frac{h^2 \alpha t}{k^2}} \operatorname{erfc} \left[\frac{x}{2\sqrt{\alpha t}} + \frac{h}{k} \sqrt{\alpha t} \right] \right\} + \frac{k}{h} a \quad (3-32)$$

Substituting the definition of v (Eq. 3-20) to obtain the temperature gives:

$$T - T_\infty = \left(T_0 - T_\infty - \frac{k}{h} a \right) \left\{ \operatorname{erf} \left[\frac{x}{2\sqrt{\alpha t}} \right] + e^{\frac{hx}{k} + \frac{h^2 \alpha t}{k^2}} \operatorname{erfc} \left[\frac{x}{2\sqrt{\alpha t}} + \frac{h}{k} \sqrt{\alpha t} \right] \right\} + a \left(\frac{k}{h} + x \right) \quad (3-33)$$

Eq. (3-33) gives the temporal evolution of the temperature distribution in a semi-infinite solid after its surface is suddenly exposed to a convective heat transfer process. If $a = 0$, the solution collapses to the original expression given by Carslaw & Jaeger²⁵ for a semi-infinite slab with uniform initial temperature.

Finally, it should be noted that when

$$a = \frac{h(T_0 - T_\infty)}{k} \quad (3-34)$$

the first term on the right side of Eq. (3-33) vanishes and the solution is time independent. This is not surprising as it corresponds to the situation where the conductive heat flow towards the surface equals the heat removed by convection. In this case, the initial condition is also the steady state condition.

3.3.2 Thermal Penetration Depth

The preceding solutions are built upon the assumption of a semi-infinite body. In practical situations, however, the semi-infinite assumption can be satisfied as long as the body is thicker than the thermal penetration depth, δ . Schultz & Jones¹⁶ defined the penetration depth as the distance at which the scaled local temperature differs from the surface temperature by 1%. This can be presented as¹⁷:

$$\frac{T_{\delta} - T_s}{T_i - T_s} = 0.99 \quad (3-35)$$

Inserting Eq. (3-35) into Eq. (3-33) gives the following implicit expression for the penetration depth:

$$\frac{\operatorname{erf}\left[\frac{\delta}{2\sqrt{\alpha t}}\right] + e^{\frac{h\delta}{k} + \frac{h^2\alpha t}{k^2}} \operatorname{erfc}\left[\frac{\delta}{2\sqrt{\alpha t}} + \frac{h\sqrt{\alpha t}}{k}\right] - 0.01 e^{\frac{h^2\alpha t}{k^2}} \operatorname{erfc}\left[\frac{h\sqrt{\alpha t}}{k}\right] - 0.99}{\delta} = -\frac{0.01}{\left(T_0 - T_{\infty} - \frac{k}{h}a\right)} \quad (3-36)$$

In general, the effect of the initial gradient (a) on the penetration depth is weak. However, at the steady state (where a is given by Eq. 3-34), the right side of the equation tends to infinity which means that δ tends to zero.

3.4 Numerical Verification of Results

Figure 3.3 illustrates the problem that motivated this work: a convectively cooled MACOR[®] plate (the test plate) with initial $T_s = 340$ K, $T_{\infty} = 317.6$ K, $h = 435$ W/m²-K (obtained through correlations^{28,29} for the flow in the experiment), and $a = 173$ K/m

(due to natural convection, obtained by correlations^{30,31}). The plate is exposed to these conditions for approximately 6.8 seconds and we are interested in predicting the temporal response of the temperature distribution in the plate in addition to the heat flux at the gas-plate interface. Eq. (3-33) is verified numerically by solving Eq. (3-1) subject to the boundary conditions of the experiment described above. The numerical solution was obtained by solving Eq. (3-1) using a central differencing scheme on a uniform grid with elements spaced 0.13 mm apart and with a time step of 1.1 ms (based on the CFL criterion), as shown in Fig. 3.3.

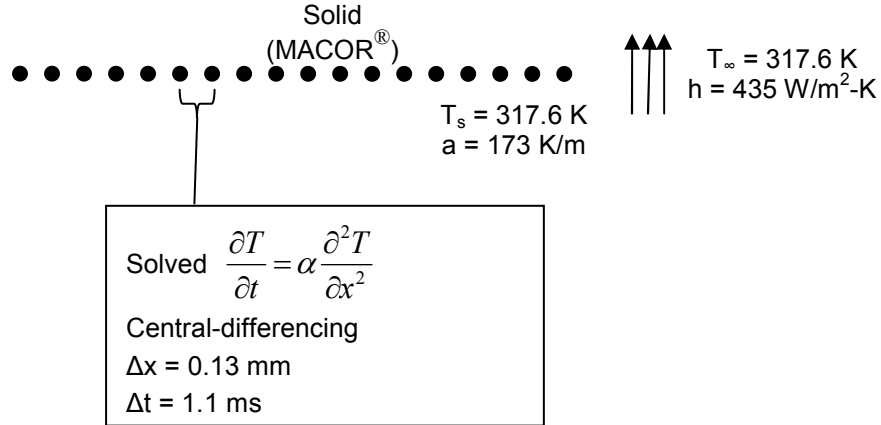


Fig. 3.3: Numerical simulation conditions.

Figure 3.4 compares plate temperature distributions predicted using Eq. (3-33) with and without an initial temperature gradient to the results of the numerical simulation with an initial temperature gradient. The fact that the numerical and analytical (Eq. 3-33) results overlap indicate that Eq. (3-33) is a valid solution to the problem.

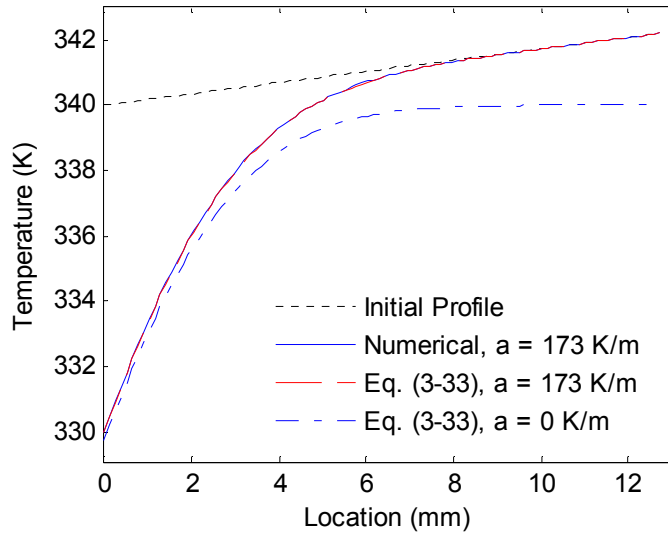


Fig. 3.4: Temperature profiles through a heated MACOR[®] plate with an initial temperature gradient 6.8 seconds after being exposed to a 317.6 K flow.

Since the principal motivation of this work is to understand the effect of an initial wall temperature gradient on convective heat flux measurements, Fig. 3.5 shows surface heat fluxes predicted using Eq. (3-33) for various initial wall temperature gradients. The heat flux decreases with time because the wall temperature decreases with time. The figure shows that a positive initial wall temperature gradient increases the heat flux from the wall to the flow. This means that assuming that the wall temperature is uniform when it is not will underestimate heat transfer when $a > 0$ and overestimate heat transfer when $a < 0$. Although this effect is not strong initially, the differences in heat flux grow and hence become more important with time. Figure 3.6 shows the error resulting from assuming a uniform temperature as a function of time for different values of the initial gradient.

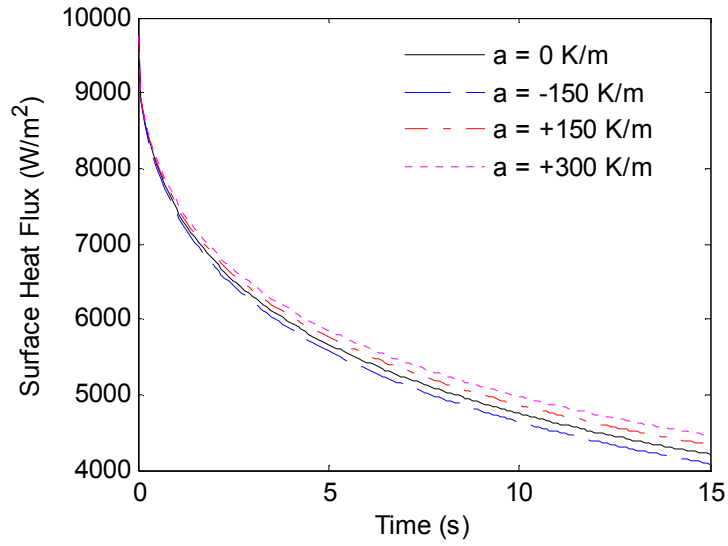


Fig. 3.5: Surface heat flux for different values of the initial thermal gradient, a .

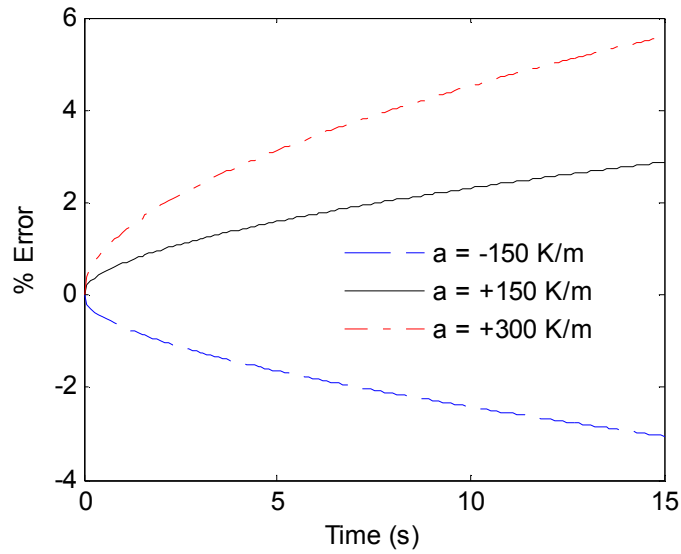


Fig. 3.6: Error in surface heat flux resulting from assuming a uniform initial temperature.

Figure 3.6 is important because it shows that for short times, the error from assuming an isothermal wall is small. For the purposes of the experiment, in which the test time

is on the order of 6 seconds, the error from assuming an isothermal wall is expected to be around 2%.

Of greater interest is how well the gradient correction technique proposed in section 3.2 actually works when applied to the convective heat transfer problem illustrated in Fig. 3.3. This is assessed by using Eq. (3-33) to generate the temperature-time history of a point 1.9 mm below the surface (the location of the thermocouple junction in the experiment). Then, this temperature-time history is used to infer the surface heat flux using the method of section 3.2.2 with $N = 5$. Finally, the inferred heat flux (dashed lines) is compared to the original or ‘actual’ analytical solution for the heat flux (solid lines) in Fig. 3.7. The comparison is made for two cases: one with a uniform initial wall temperature and one with an initial wall temperature gradient. The ‘ripple’ in the inferred heat flux is an artifact of the fitting process. It can be reduced by increasing the number of terms, N , but this comes at significantly increased computational cost. The effect of N will be discussed more in the next section.

Figure 3.8 shows that the errors (or differences) in both cases are +/- 2%. The fact that both curves lie virtually on top of each other demonstrates that the gradient correction technique from section 3.2.2 has removed the error arising from the initial gradient. Finally, Fig. 3.9 compares the surface temperature predicted using Eq. (3-33) to that inferred from the temperature-time history of the subsurface point. These results also demonstrate the validity of the gradient correction technique.

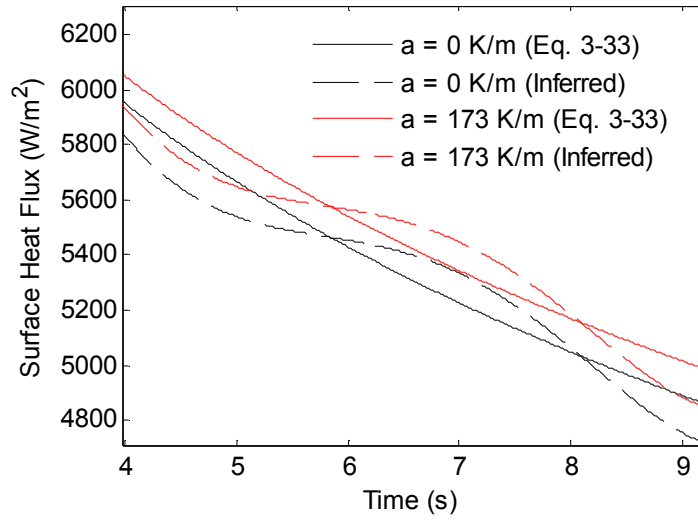


Fig. 3.7: Effect of gradient correction on inferred surface heat flux.

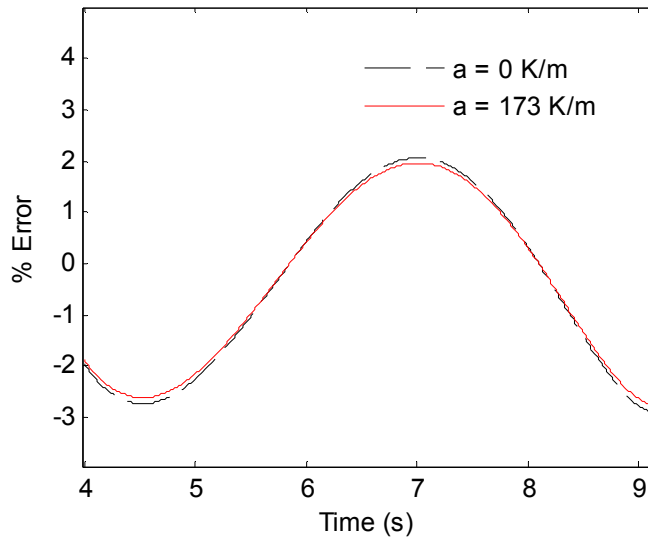


Fig. 3.8: Errors in inferred surface heat flux.

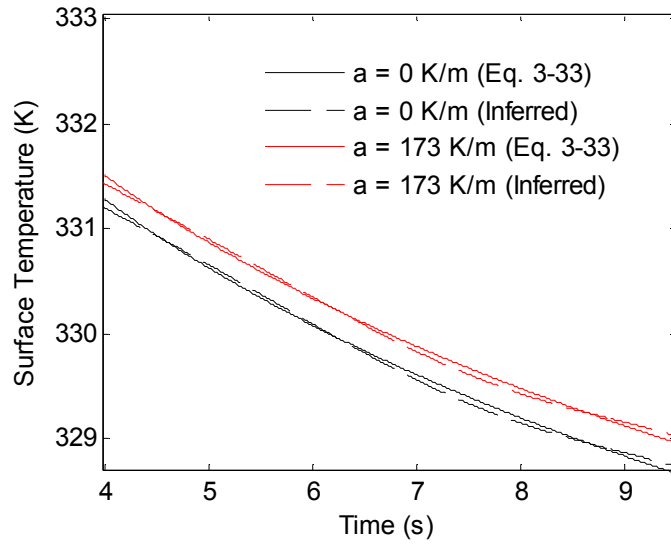


Fig. 3.9: Comparison of surface temperatures predicted using Eq. (3-33) and inferred from the subsurface temperature-time measurements.

3.5 The Effect of N (number of terms)

N is the number of terms that are used in the curve-fitting procedure (eq. 3-5). In general, a higher N implies higher accuracy (provided the solutions are converged) but at increased computational cost; increasing N is similar to grid refinement. For the convection problem in section 3.4, the effect of N on the inferred surface heat flux is shown in Figs. 3.10 and 3.11.

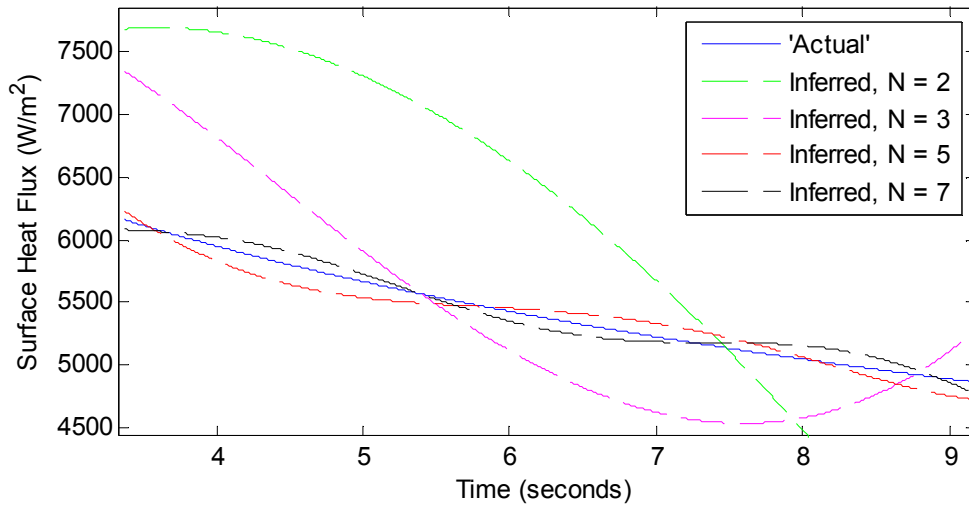


Fig. 3.10: Inferred surface heat flux for different values of N .

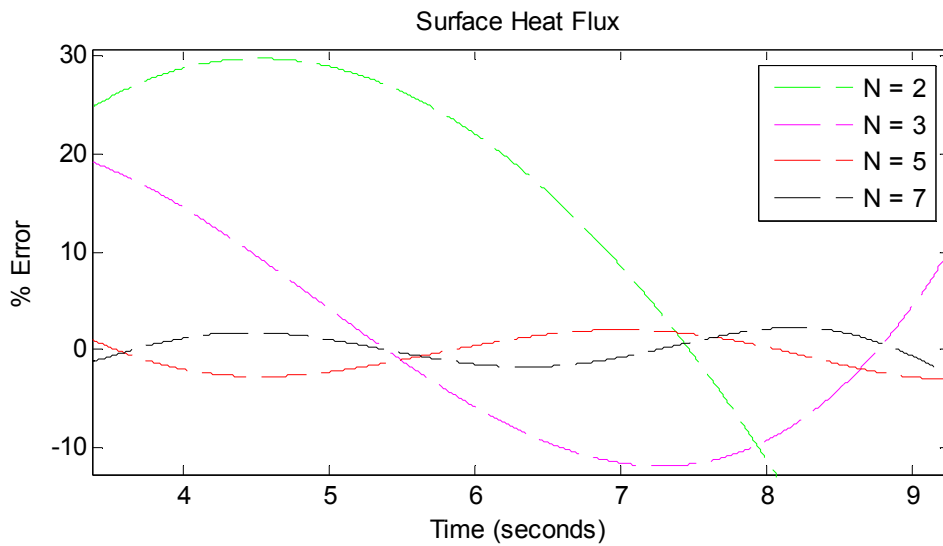


Fig. 3.11: Error in inferred surface heat flux for different values of N .

Figs. 3.10 and 3.11 demonstrate how increasing N improves the accuracy of the inverse method. These plots also show that in this case increasing N over 5 terms results in a negligible reduction of error, therefore one could say that the solutions are

‘converged’ at $N = 5$ for this case. Fig. 3.12 shows how the root mean square of the error varies with N .

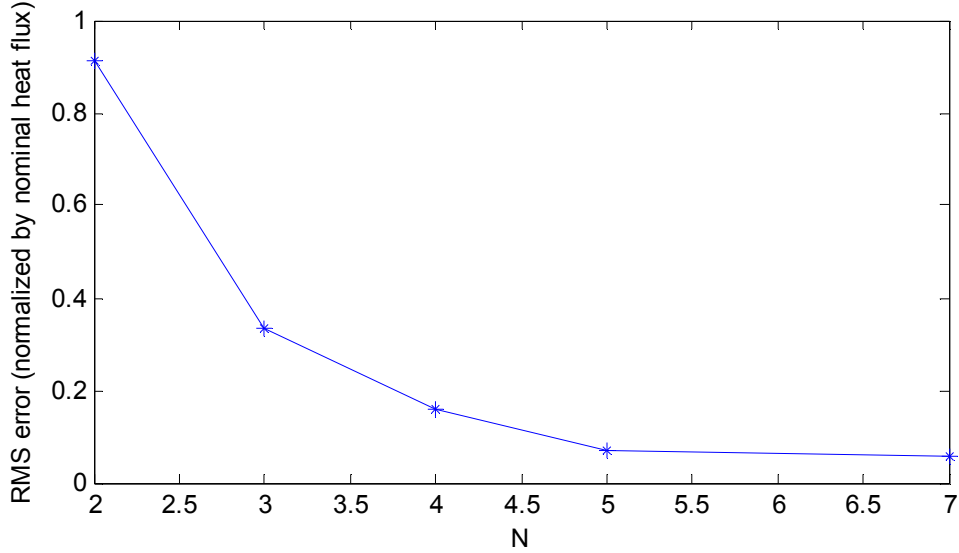


Fig. 3.12: Root mean square error for different values of N .

The time required for these computations increases with N and is unique for every problem. For this particular convection problem, the computational time with $N = 2$ is less than a minute, whereas with $N = 7$ it is over 10 minutes using an Intel Core 2 Duo 2.66 GHz processor.

3.6 Uncertainty in Heat Flux and Temperature Measurements

Standard methods are used to combine the uncertainties in the heat flux measurements³³. The standard (or total) uncertainty in a calculated quantity, V , which is a function of parameters $P_1, P_2, P_3, \dots, P_N$ is given by

$$V(P_1, P_2, P_3, \dots, P_N) = \sqrt{\sum_{i=1}^N (\theta_i \delta_i)^2} \quad (3-37)$$

The sensitivity coefficients θ_i are given by:

$$\theta_i = \frac{\Delta V}{\Delta P_i} \quad (3-38)$$

and δ_i is the uncertainty in the i^{th} parameter. The term $(\theta_i \delta_i)$ in eq. (3-37) is the uncertainty in the calculated quantity, V , due to the i^{th} parameter. Errors in the heat flux measurements can arise from four sources: uncertainty in the temperature readings (± 0.5 K), machining tolerance in the depth of the heat flux gauge location (± 0.005 in.), uncertainty in the thermal properties of MACOR[®] ($\pm 3\%$ ^{34,35}), and the curve-fitting process itself.

The terms $(\theta_i \delta_i)$ can be calculated numerically. The temperature, sensor location, and thermal diffusivity are perturbed in the numerical routine to observe their impact on the heat flux measurements, and the results are shown in figs. 3.13-3.15, for the problem in fig. 3.3, and the error due to the curve-fitting process itself is shown in fig. 3.16. The maximum errors due to the different sources are summarized in Table 3.1.

Table 3.1: Sources of error

<i>Source</i>	<i>Error Contribution $(\theta_i \delta_i)$</i>
Temperature	0.05
Sensor location	0.04
Thermal properties	0.03
Curve-fitting process	0.03

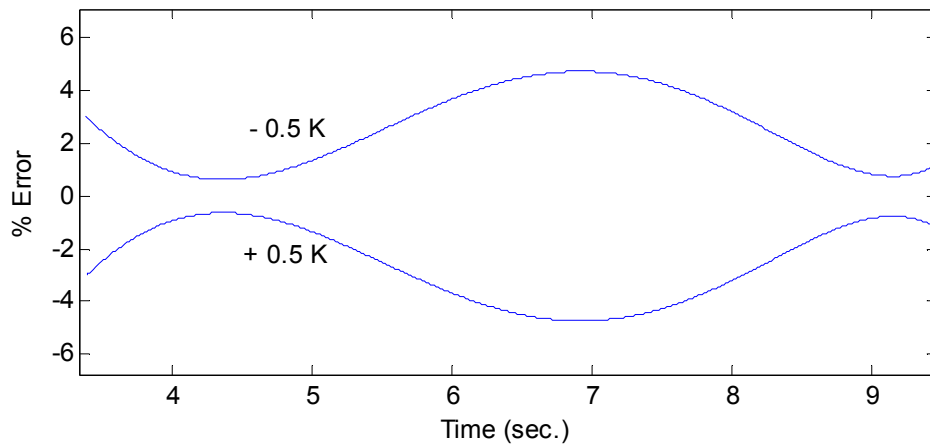


Fig. 3.13: Error in surface heat flux due to temperature uncertainty.

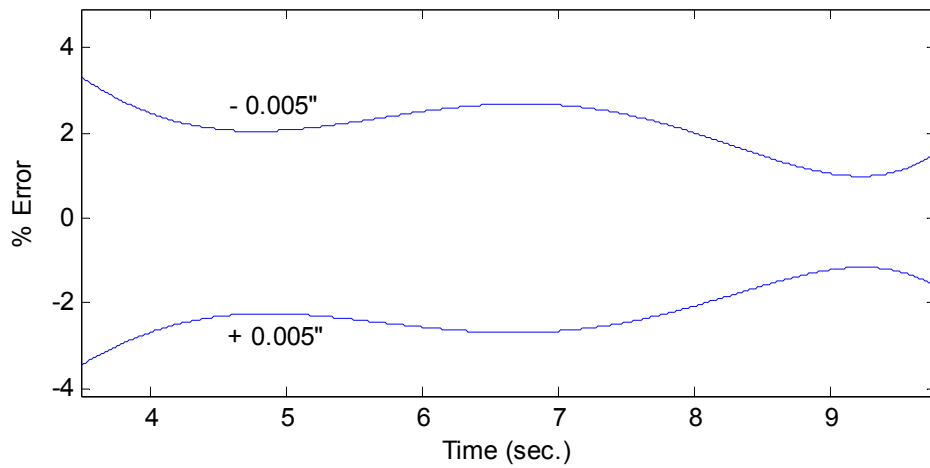


Fig. 3.14: Error in surface heat flux due to sensor location uncertainty.

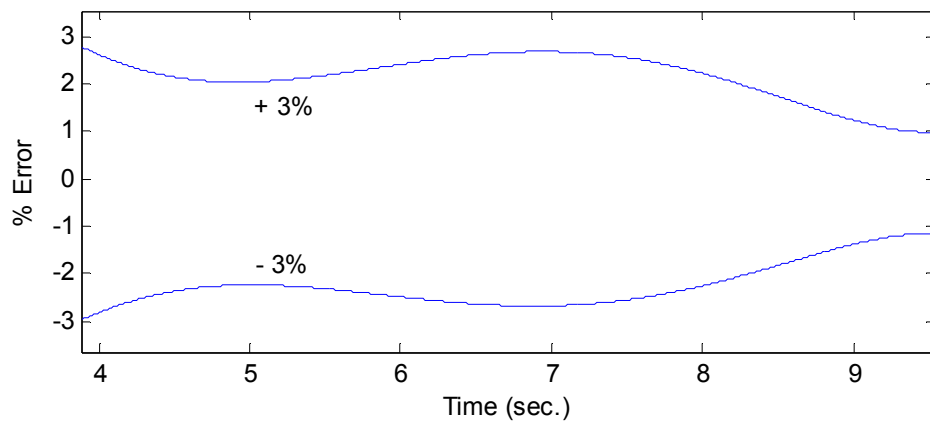


Fig. 3.15: Error in surface heat flux due to uncertainty in thermal properties.

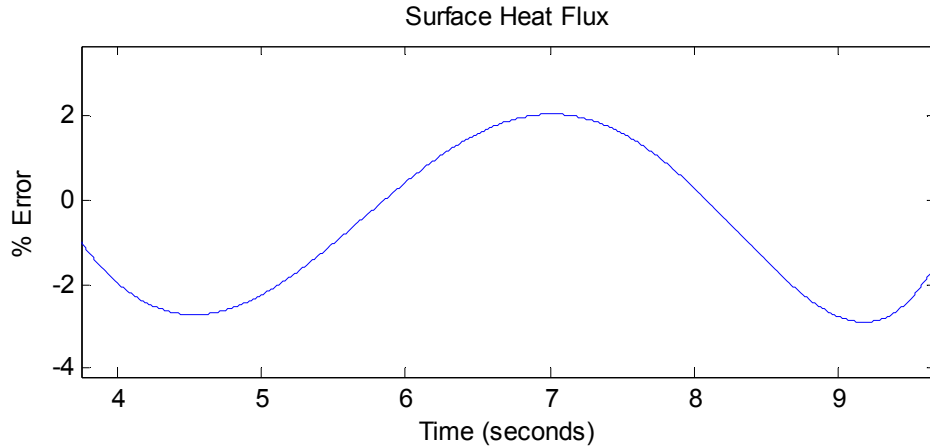


Fig. 3.16: Error in surface heat flux due to curve-fitting process.

These errors can now be combined using eq. (3-37). The result for the problem in fig. 3.3 is a combined uncertainty of 7.7%. While these uncertainty values are for the specific example in Fig. 3.3, this procedure was also applied to the experimental heat flux measurements in chapter 4 and it was found that the maximum error did not exceed 9.5% for all measurements (except those in the recirculating region of the rearward step in section 4.3.2). In light of the preceding analyses, standard uncertainty of 10% has been applied to the heat flux measurements (except for the measurements in the recirculating region, where due to small heat fluxes (a few hundred W/m^2), the uncertainty is up to 70% - this is reflected in the error bars in fig. 4.26).

3.7 Instrumentation Test

While the analytical and numerical aspects of the inverse measurement technique have been verified, the heat flux sensor hardware also needs to be assessed. To test the heat flux sensors, a slab of melting ice was suddenly placed on the test plates.

This produces an isothermal wall boundary condition because the melting ice is at 0° C. The resulting surface heat flux, as measured by the sensors, can be compared with the analytical solution to this problem:

$$\frac{T(x,t) - T_s}{T_i - T_s} = \text{erf}\left(\frac{x}{2\sqrt{\alpha t}}\right) \quad (3-39)$$

Fig. 3.17 shows the surface heat flux inferred from the sensors and compares it with the analytical solution given by eq. (3-39). It can be seen that there is good agreement between the experimental and analytical results (the mean error is less than 2%). This indicates that the heat flux sensor can produce an appropriate temperature signal from an interior location.

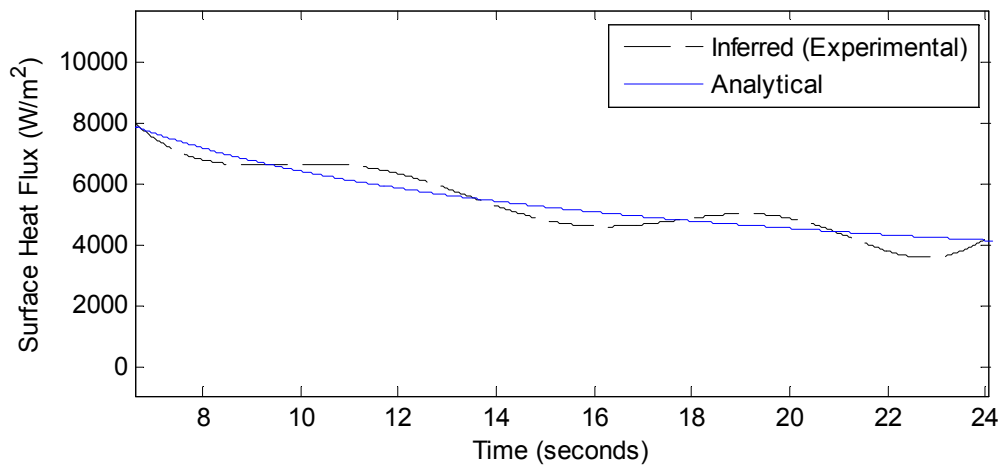


Fig. 3.17: Surface heat flux with 0° C isothermal wall boundary condition.

Chapter 4: Results

The principal objective of this chapter is to demonstrate that the measurement systems and especially the heat flux measurement technique function properly in a realistic supersonic flow. It is not to quantify the performance of the film in the experiment or validate the CFD simulations. These require a more extensive experimental effort which is beyond the scope of this thesis. Nevertheless, these things are discussed in order to demonstrate the efficacy of the measurement techniques and to provide preliminary but still useful assessments of the flow structures, pressures, temperatures, and heat fluxes.

4.1 Configuration of demonstration experiments.

The test conditions are similar to those of the first three test cases (Table 2.1) but with somewhat different Mach numbers and a different film total temperature. The latter is the result of problems with the film heater that could not be resolved before the tunnel had to be given up to the next set of users, and therefore all the results are with a film total temperature equal to ambient temperature. This is not expected to significantly change the behavior of the shear layers because the change in film temperature implies a 6% change in the speed of sound, and therefore the film velocity. It was also observed by Goldstein et al.⁶ that the film temperature did not significantly affect Schlieren images. While the Schlieren images are not expected to change significantly due to film heating, the only direct comparison to CFD that is possible is along the upper, unheated wall. Measurements on the lower wall in a zero film flow

situation are also presented. The experimental conditions are summarized in Table 4.1.

Table 4.1: Experimental test conditions. All flow temperatures are 295 K.

Test	Core Mach number	Film Mach number
1	2.26	0.51
2	2.26	0.72
3	2.26	1.2
No film flow	2.26	0

4.2 Schlieren Imaging and Pressure Measurements

4.2.1 Test Case 3

The results from test case 3 will be discussed first because they best demonstrate the key features of a supersonic film cooling flow. The design injectant Mach number is 1.4, as shown in Table 2.1, but we will see shortly that the actual Mach number is 1.2. The static pressures in the core and film streams are matched. Fig. 4.1 is a contrast-enhanced (83%) Schlieren image of the flow near the film injection point (full-view images are provided in Appendix D).

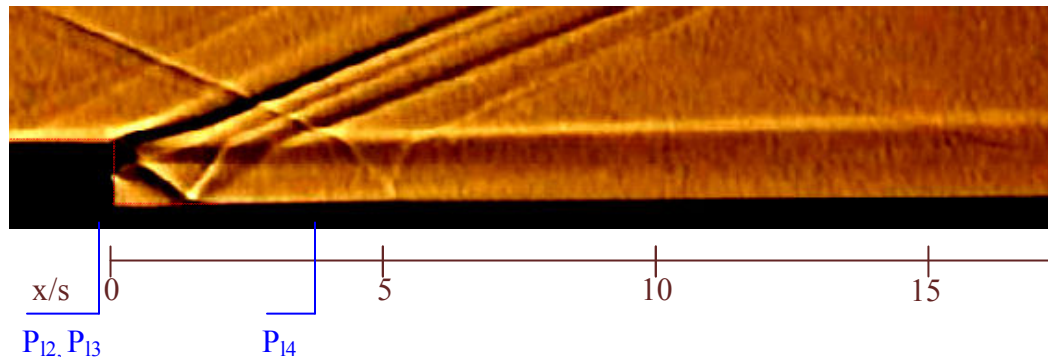


Fig. 4.1: Schlieren image for supersonic film injection (Test case 3) with matched static pressures.

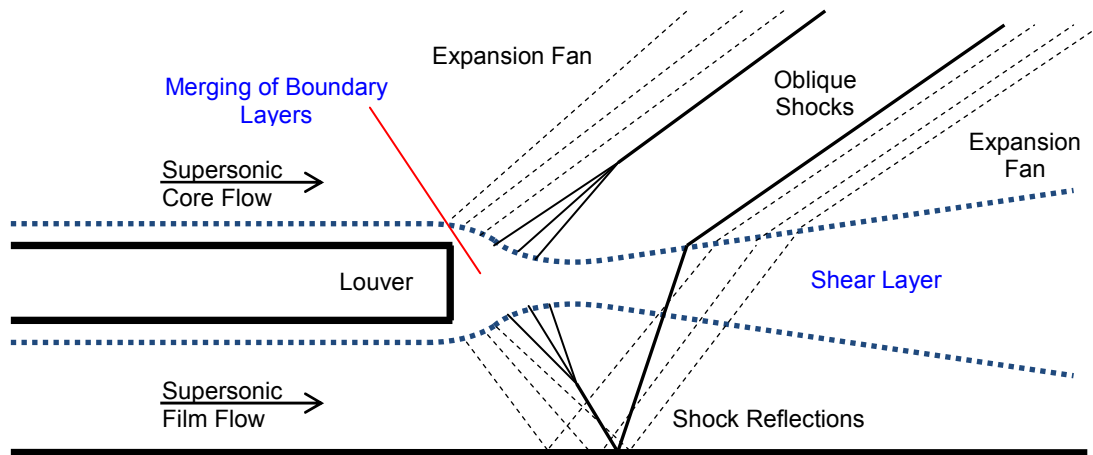


Fig. 4.2: Flow features in supersonic film cooling.

Figure 4.2 is a cartoon of the key flow features observed in Test Case 3. A shear layer forms at the interface of the core and film flows. Initially, the shear layer thickness is only the sum of the thicknesses of the boundary layers on the upper and lower surfaces of the louver. Since this sum is smaller than the louver thickness, the flows are drawn toward the louver centerline as they pass the louver lip. This produces expansion fans emanating from both sides of the lip. Soon, however, the incompressible shear layer begins to grow. This turns the core and film flows into themselves producing oblique shocks. The shocks in the film reflect off the wall, refract through the shear layer, and then proceed into the core flow.

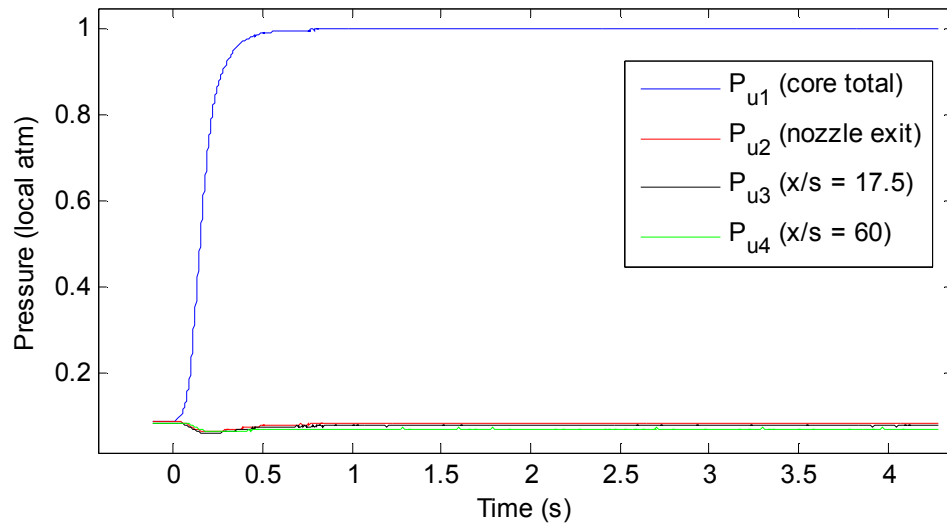


Figure 4.3: Pressure measurements along the upper wall with supersonic injection.

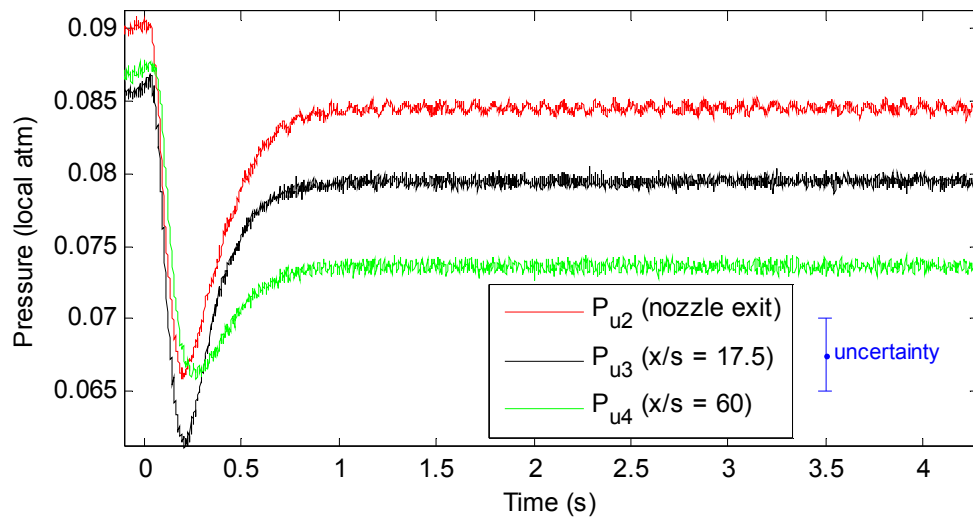


Figure 4.4: Zoom in on upper wall static measurements for supersonic film injection.

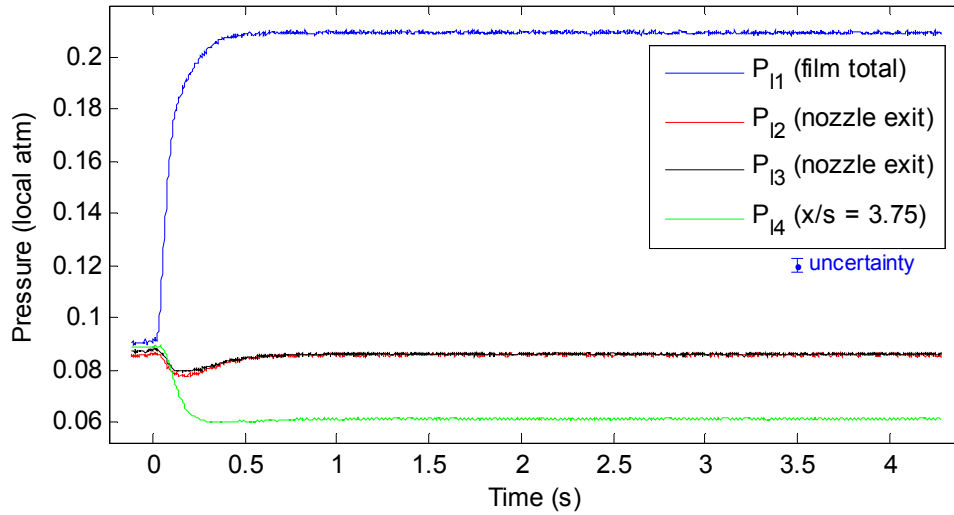


Fig. 4.5: Pressure measurements along the lower wall with supersonic injection.

The pressure measurements along the upper wall (Fig 4.3 and 4.4) indicate that the core exit Mach number is 2.26, not 2.4 as designed. Pressure measurements along the lower wall (Fig. 4.5) show that the film exit Mach number is 1.2, not 1.4 as designed. The discrepancy in the core flow Mach number is probably the result of imperfect assumptions made by the method of characteristics. First, the method of characteristics does not account for viscous effects. Secondly, it assumes a truncated contour at the throat whereas the ‘real’ nozzle uses a circular profile. Viscous effects appear to be the dominant reason for the discrepancy in the film nozzle exit Mach number. Fig. 4.5 also shows that the static pressure at $x/s = 3.74$ on the lower wall (P_{14}) is lower than at the film nozzle exit. This means that the expansion fans in the film flow are stronger than the oblique shocks. The fact that the two static pressure readings at the film nozzle exit, P_{12} and P_{13} , are nearly identical indicates that there is little or no 3-dimensionality in the flow at the lower exit. It can also be seen that prior to starting the experiment, the pressures are not exactly equal to each other,

which is largely due to measurement uncertainty, but also possibly due to the fact that the air has not completely settled in the tunnel after being pumped down. Lastly, Fig. 4.4 also shows that the static pressure along the upper wall decreases slightly as the flow progresses downstream. This is the reverse of what is generally observed for supersonic flow in a duct where the pressure rises with downstream distance. The reason for a pressure decrease in the experimental test section is that the blowing ratio is less than one. This means that less air per unit area is entering the test section from the film louver. Therefore, upon meeting the film, the core flow can expand into the film. The result is that the average flow area for the supersonic core flow increases in the test section, and it is this expansion which causes a drop in the static pressures.

4.2.2 Test Case 2

This test case corresponds to Mach 0.73 film injection. To achieve this, the film flow butterfly valve was throttled down from the Mach 1.4 injection case. A Schlieren image of this test case is shown in Fig. 4.6. No shocks are observed in the film stream because it is subsonic. However, shocks persist in the core stream.

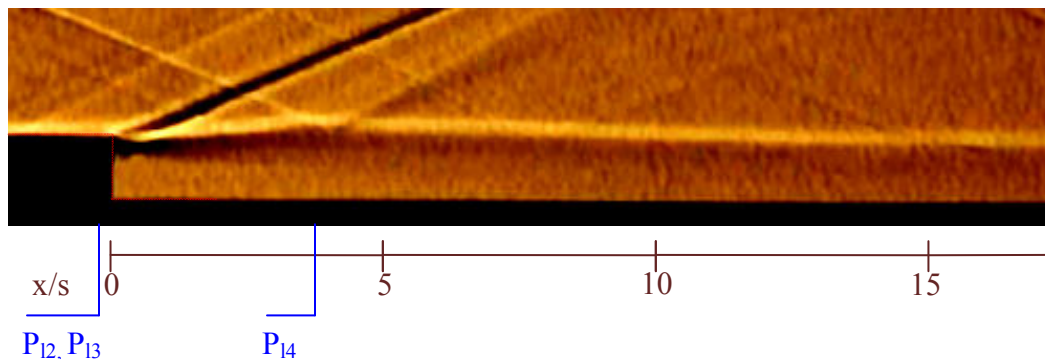


Fig. 4.6: Schlieren image for Mach 0.73 film injection.

The shear layer is visible as the growing light and dark bands between the two streams. It appears to reach its highest at the point where a disturbance hits it from upstream. This disturbance is likely due to non-ideal expansion in the core nozzle at the point where the method of characteristics contour was truncated. After this point the shear layer appears to come down, and the upper boundary (light region) appears to settle at a constant height above the wall.

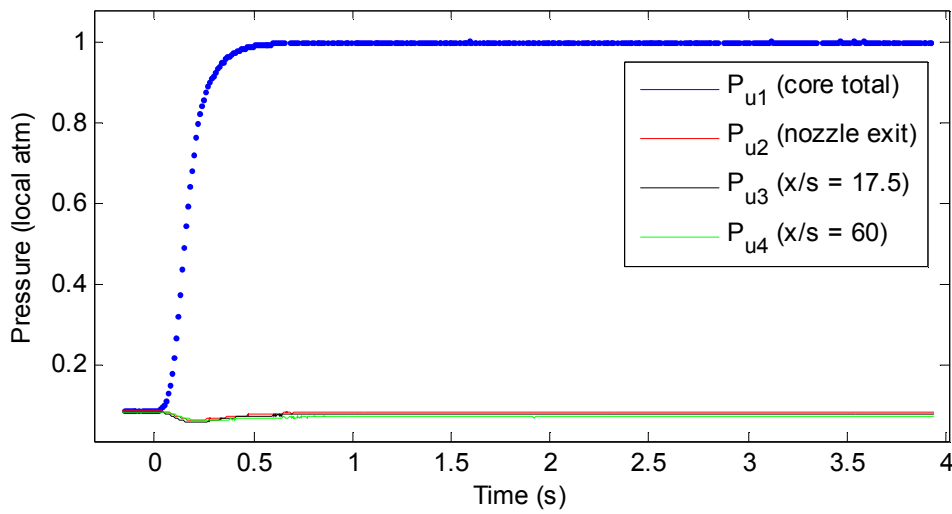


Fig. 4.7: Pressure measurements along upper wall with Mach 0.73 injection.

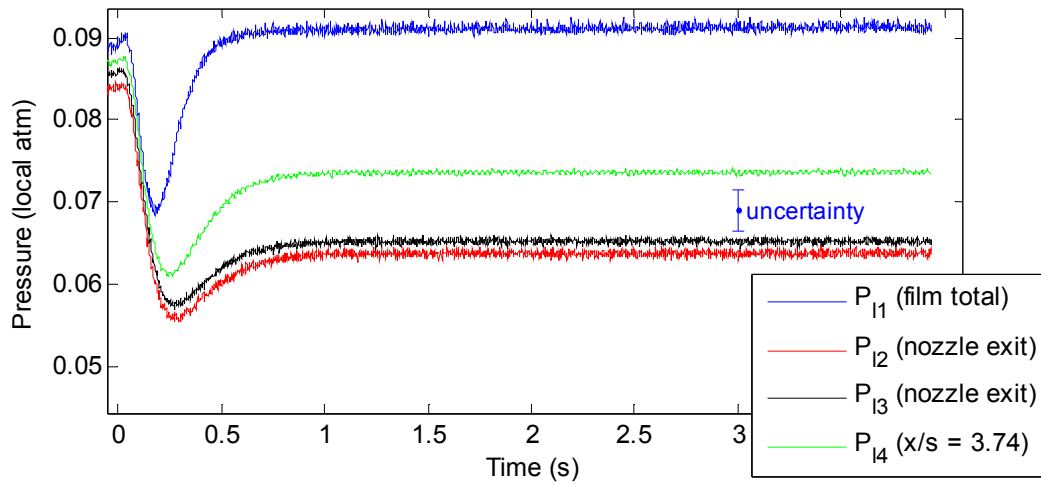


Fig. 4.8: Pressure measurements for lower wall with Mach 0.73 injection.

The pressures along the upper wall in Fig. 4.7 are identical within 3% of those observed for the supersonic film injection case. However, the lower wall readings in Fig. 4.8 are substantially different. The total and static pressure pressures correspond to a mean film Mach number of 0.72. The pressures at the louver exit are consistent within the experimental uncertainty which is proportionally larger here because the sensors are operating at only 6% of their rated pressure. Unlike the supersonic film injection case, the static pressure at $x/s = 3.14$ (P_{14}) is higher than at the film exit indicating the presence of an adverse pressure gradient and is consistent with the increase in shear layer thickness observed in the images. Due to absence of shocks, the film static pressure would be expected to approach the core static pressure as the flow progresses.

4.2.3 Test Case 1

This test case corresponds to a film injection Mach number of 0.5. Fig 4.9 is a Schlieren image of the flow, and Figs. 4.10 and 4.11 show results for wall pressure measurements. The results are qualitatively similar to Test Case 2, but the shear layer seems to settle at a lower height than with Mach 0.73 injection, as is expected.

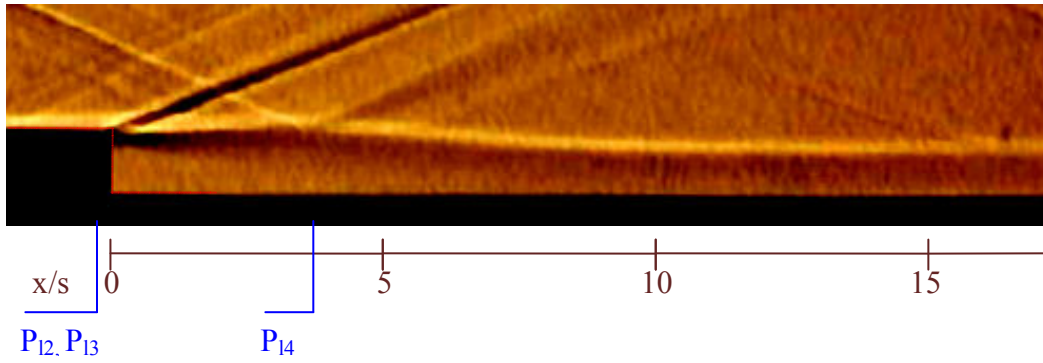


Fig. 4.9: Schlieren image for Mach 0.5 film injection.

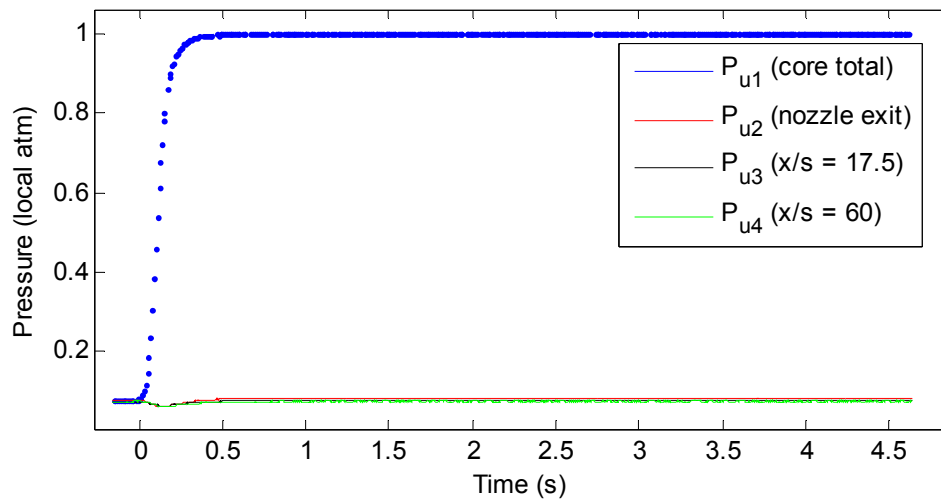


Fig. 4.10: Upper wall pressures for Mach 0.5 film injection.

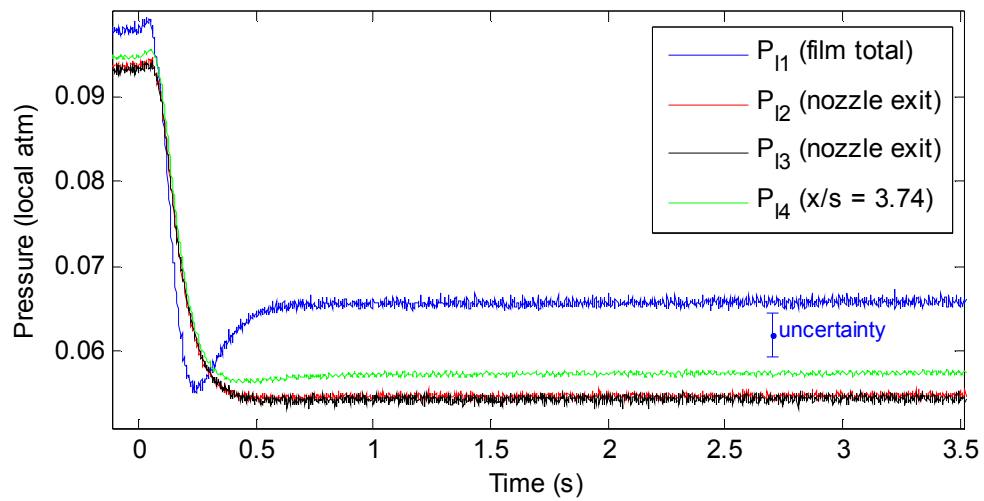


Fig. 4.11: Lower wall pressures for Mach 0.5 film injection.

The pressure on the upper wall behaves the same way as in the other test cases (within 3%). The trends on the lower wall are qualitatively similar to those observed for Mach 0.73 injection. As described previously, the differences between P_{12} and P_{13} are within the experimental uncertainty. The average injection Mach number based on these readings is 0.51.

4.2.4 No Film Flow

Finally, data was gathered with no flow through the louver. Since the film globe valve was closed for this experiment, the situation becomes essentially one of supersonic flow over a rearward-facing step. The pressure readings on the upper wall are identical to those observed in the previous test cases, and the lower wall readings are not particularly meaningful or useful, therefore only the Schlieren image will be presented here in Fig. 4.12.

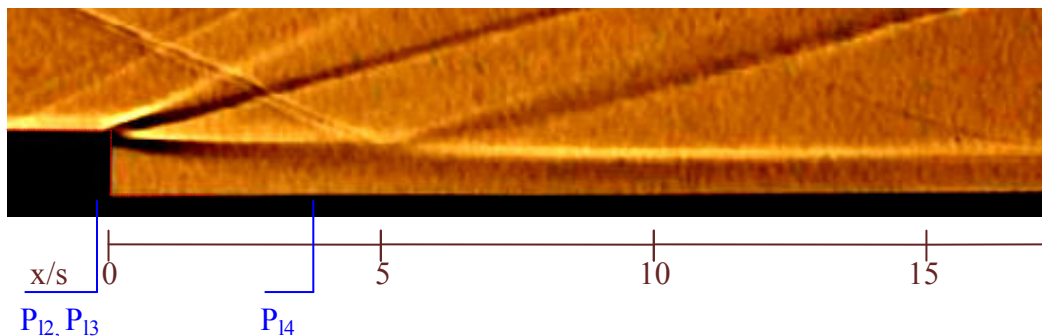


Fig. 4.12: Schlieren image with no film injection.

The flow over the lower wall with no film flow is very similar to supersonic flow over a rearward-facing step which has been studied extensively²⁶. The main features in such a flow are shown in Fig. 4.13. The supersonic flow, upon encountering the

step, expands downwards, which produces an expansion fan. When the expanded flow meets the lower wall after the step, it straightens by turning into itself, thereby producing an oblique shock (termed the reattachment shock). Between the flow and the step is a recirculating region which forms a free shear layer with the core flow. Heat flux to the wall in this recirculating region is small, but it rises sharply after the reattachment point.

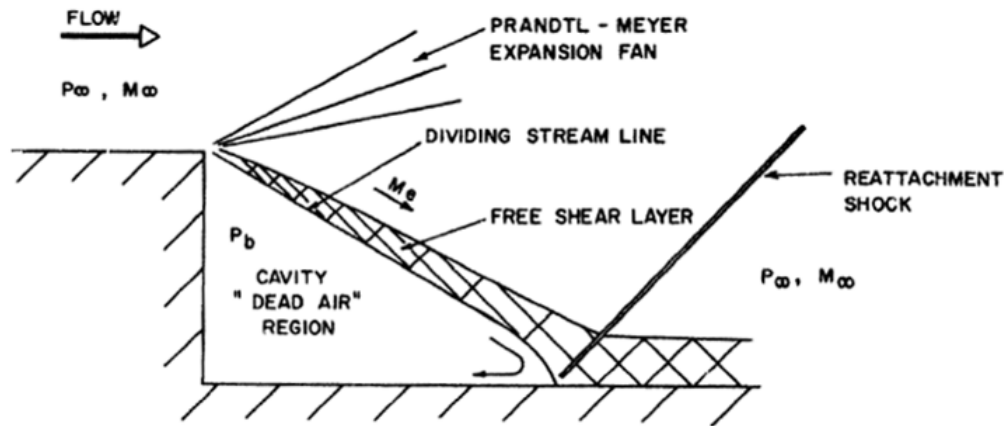


Fig. 4.13: Supersonic flow over a rearward-facing step (Due to H. E. Smith²⁶)

In the Schlieren images (Figs. 4.12 and 4.15), one can see that after the initial expansion fan, there is also an oblique shock which emerges from the lip. This shock (termed the ‘lip shock’) is due to the finite and growing thickness of the shear layer. A more detailed description of supersonic flow over a step shows the lip shock in Fig. 4.14.

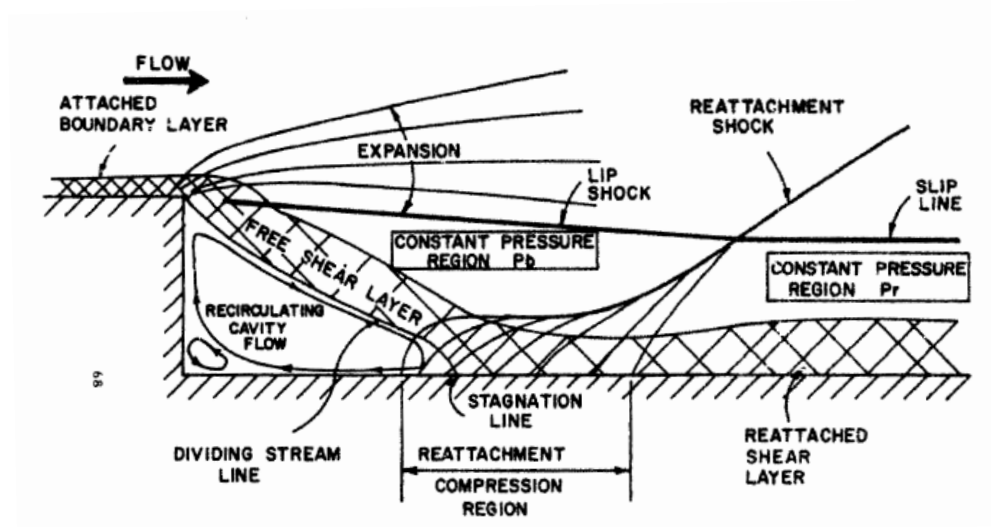


Fig. 4.14: Detailed description of supersonic flow over a step to explain the lip shock (Due to H. E. Smith²⁶)

In light of the preceding discussion, the reattachment point after the step can be determined in two ways. The first indicator is the origin of the reattachment shock, and the second indicator is the spike in surface heat flux.

4.2.5 Comparison of Schlieren Images

A comparison of Schlieren images from the different test cases is presented in Fig. 4.15.

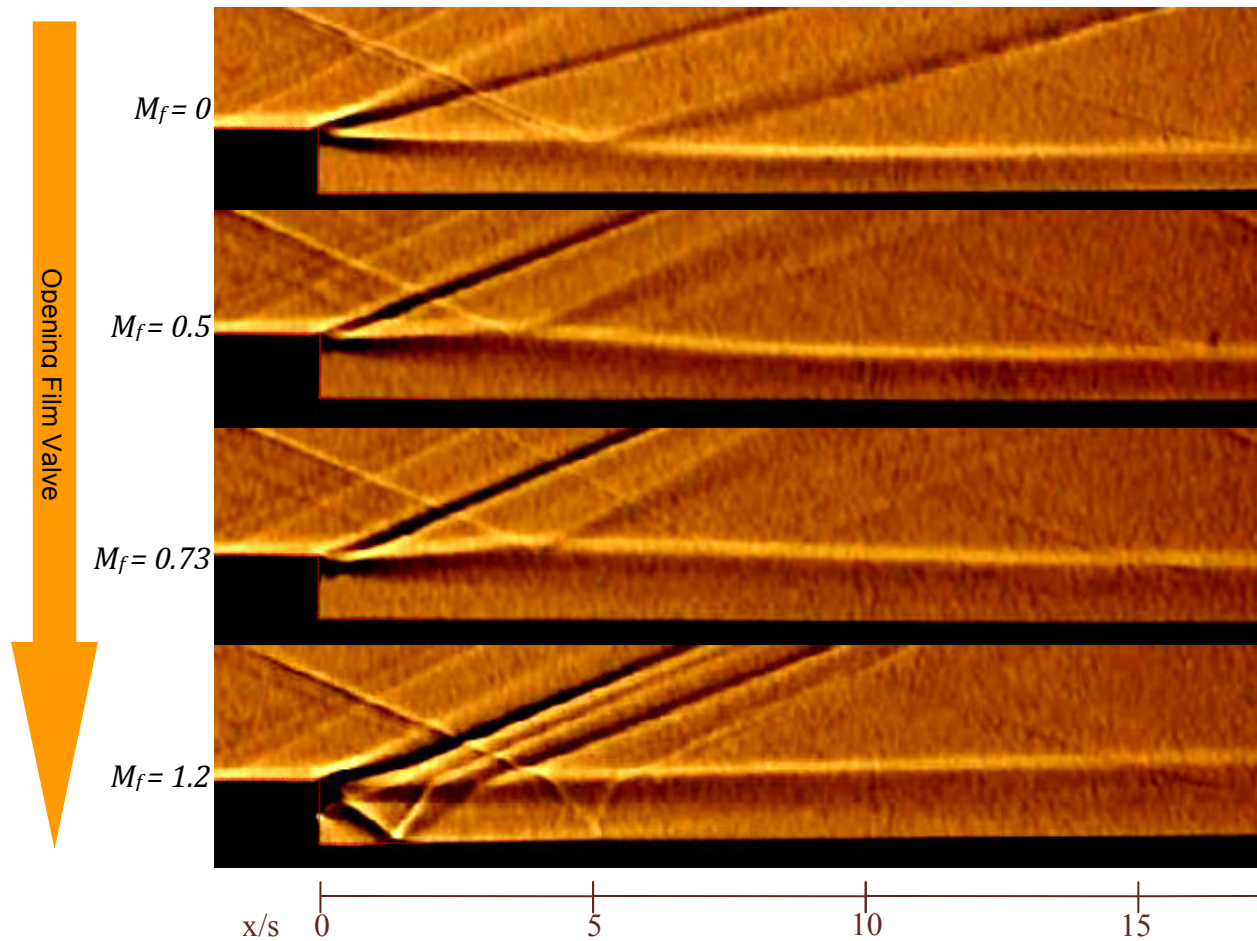


Fig. 4.15: Schlieren images showing progressing of shear layer growth with film injection Mach number.

It can be seen that as the film Mach number is increased (or as the film globe valve is opened), the shear layer appears to ‘lift up’. This is especially evident as one observes the right side (the downstream section) of the images.

4.2.6 Comparison with Numerical Results

The Schlieren images for the different test cases are compared to gray-scale images of the density gradient field computed by Dellimore⁵ using LOCI-Chem, a RANS-based solver with Menter’s SST turbulence closure. In keeping with the previous order, the

supersonic film injection case will be discussed first. Figure 4.16 (a) shows a grayscale numerical density contour with the shear layer outlined by red lines. Figure 4.16 (b) is an experimental Schlieren image. The shear layer is visible as the light and dark stripes between the core and film flows. Superimposed on the Schlieren image are the red lines that demarcate the shear layer from the numerical results. It can be seen that the numerical results are not accurate in the vicinity of the injection point, but appear to improve as one moves downstream.

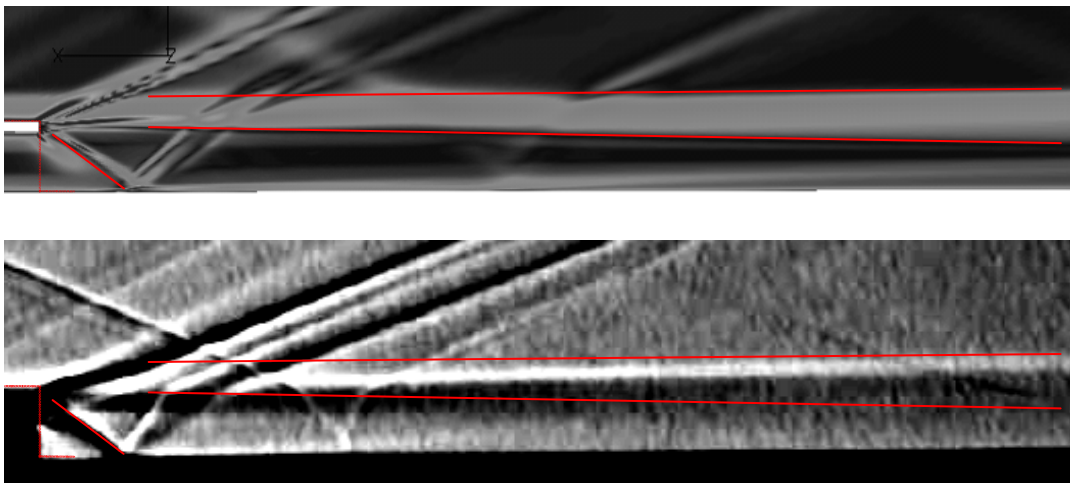


Fig. 4.16 (a) Numerical density gradient contour (b) Schlieren image for supersonic film injection.

Next, Fig. 4.17 compares experimental and numerical results for the Mach 0.73 film injection case. The images suggest that the simulations over-estimate viscous effects: the boundary layer on the upper surface of the louver is almost twice as thick in the simulations as it is in the Schlieren images. This trend continues in the shear layer.

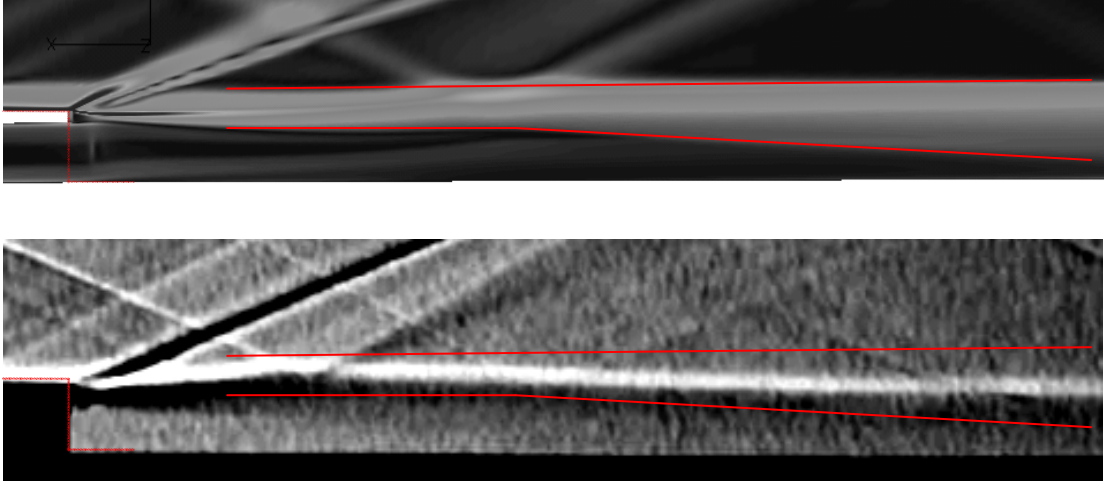


Fig. 4.17 (a) Numerical density gradient contour (b) Schlieren image for Mach 0.73 film injection.

Next, figure 4.18 compares results for the Mach 0.5 film injection case. While the images are qualitatively similar, the agreement between experiment and simulation is poorer.

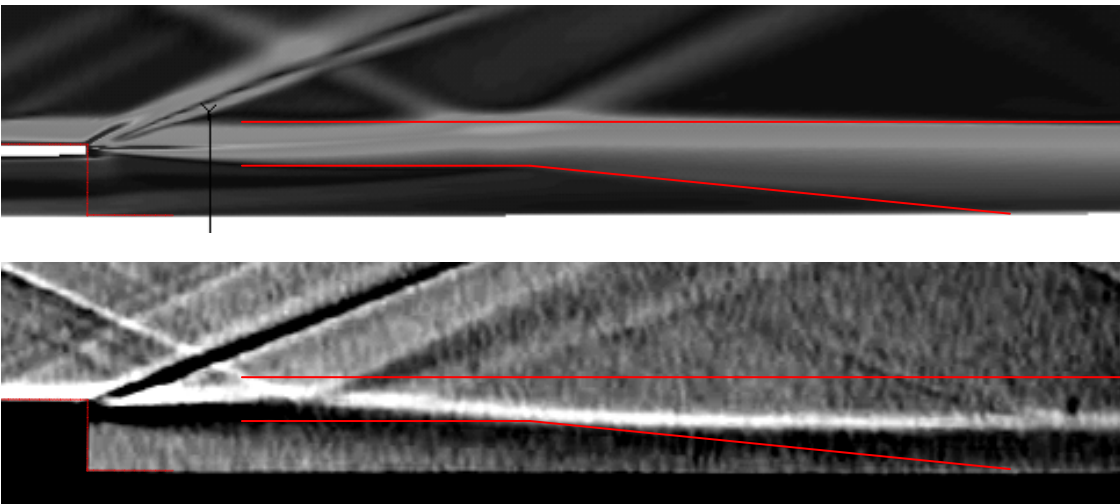


Fig. 4.18 (a) Numerical density gradient contour (b) Schlieren image for Mach 0.5 film injection.

Lastly, the results with no film flow are compared in Fig. 4.19. LOCI-Chem seems to predict an artificially steep decline of the free shear layer as compared to what is observed experimentally. Heat flux measurements were also made for this test case, which is essentially supersonic flow over a rearward-facing step. These are discussed in more detail in the next section.

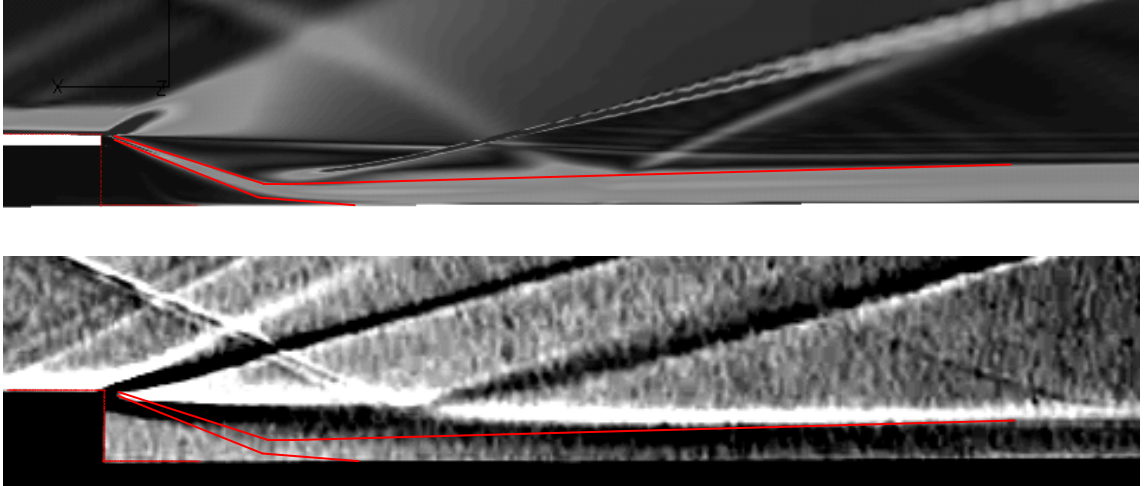


Fig. 4.19 (a) Numerical density gradient contour (b) Schlieren image with no film injection.

4.3 Heat Transfer Measurements

4.3.1 Upper Wall Heat Flux

As described in chapters 1 and 2, heat flux on the plain upper wall is needed as Q_0 , the reference heat flux to compute film cooling effectiveness. The upper wall was heated using electric cartridge heaters to about 60 K above ambient temperature. Once this temperature was reached, electric power was turned off and the plates were allowed to cool down to a little over 40 K above ambient. This allowed non-uniformities in plate temperature to be smeared out. At this temperature, the flow was

initiated and temperature measurements at the embedded locations were recorded for heat flux calculations.

The detailed procedure for inferring heat flux from interior temperature measurements was described in chapter 3, but a sample measurement will be described here. Figure 4.20 shows the raw temperature data from a sensor.

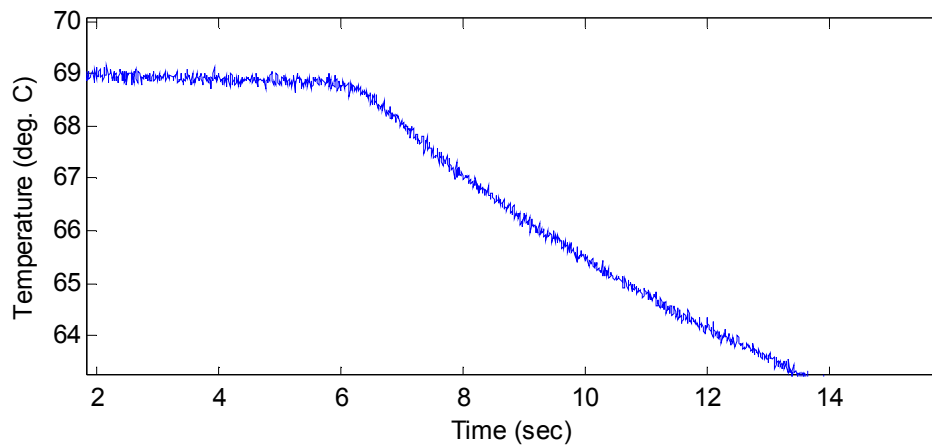


Fig. 4.20: Raw temperature signal for heat flux gauge.

It can be seen that prior to starting the experiment (which is at 6 sec. here), there is a small temperature gradient that exists because of heat loss from the plates to the environment. The first steps in the data analysis are to truncate the data set so as to isolate the data associated with flow in the tunnel and to correct for the initial gradient prior to starting the experiment (this initial gradient was found to not have a significant effect on the measurement results). The result of taking these steps is shown in Fig. 4.21.

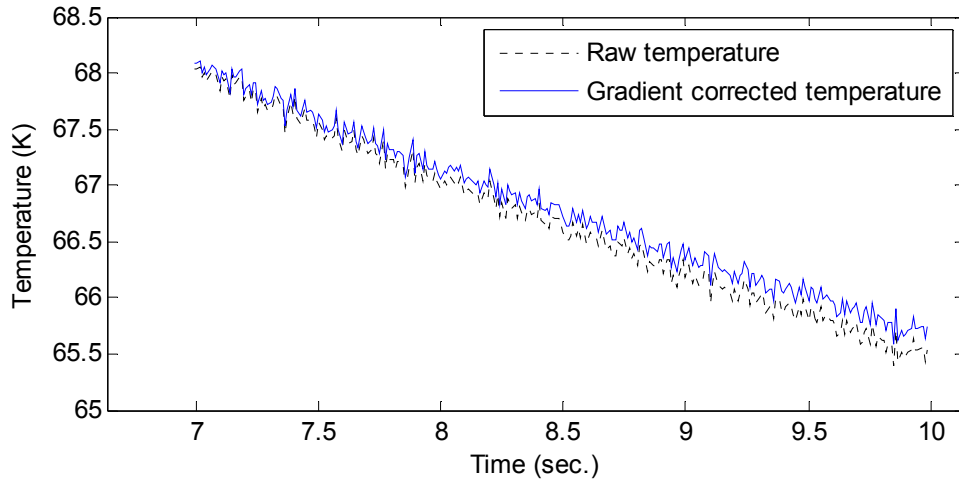


Fig. 4.21: Isolated and gradient corrected temperature data.

The next step is to non-dimensionalize the data as described in chapter 3 and fit eq. (3-5) to the temperature-time history using the optimization routine. The result of these steps is shown in Fig. 4.22.

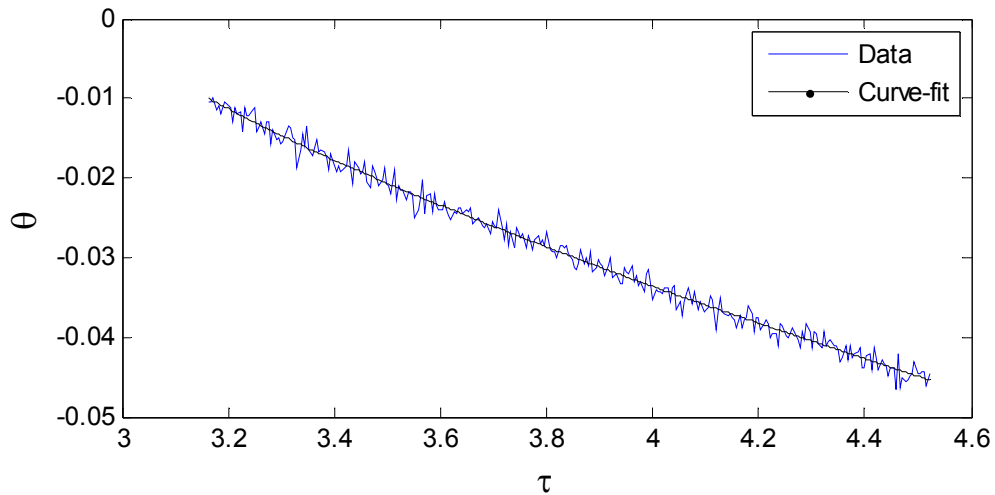


Fig. 4.22: Non-dimensionalized data and the corresponding curve-fit.

The last step is to use the coefficients from the curve-fit to obtain the surface temperature and heat flux. The results are shown in Figs. 4.23 and 4.24. Recall that the inferred values oscillate around the actual values (previously seen in Fig. 3.7).

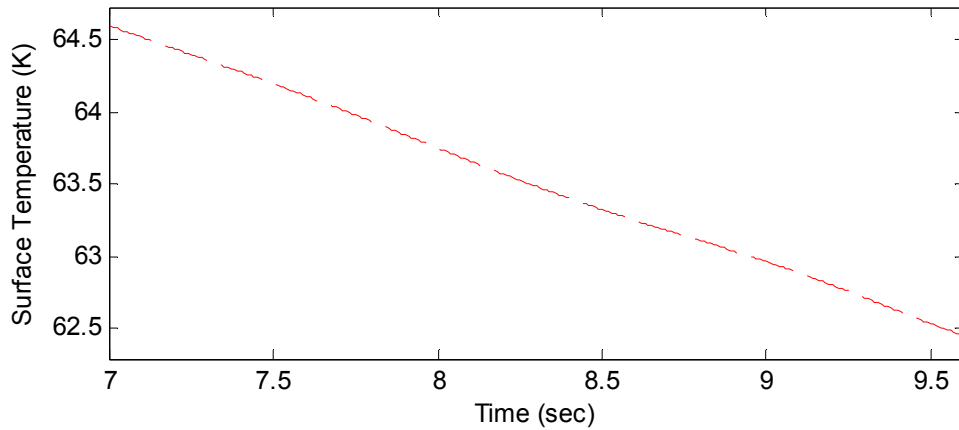


Fig. 4.23: Inferred surface temperature.

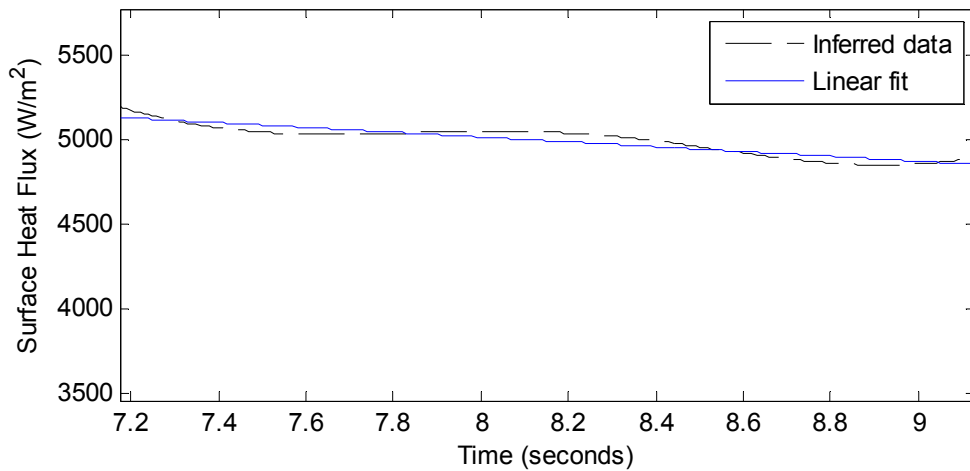


Fig. 4.24: Inferred surface heat flux.

The ambient temperature for this experiment was $24^{\circ}C$ so the surface temperature is 40 K above ambient at 7.75 seconds. At this point the corresponding heat flux is approximately $5100 W/m^2-K$. This value can now be compared with numerical

simulations which assumed an isothermal wall 40 K above the core total temperature. While every effort was made to keep the plates spatially isothermal, it was not possible to obtain all heat transfer measurements at exactly 40 K above ambient temperature. In this event, the surface temperature closest to 40 K above ambient and its corresponding heat flux were used to calculate a local value of h , the convective heat transfer coefficient. This value of h was then used to determine the surface heat flux if the wall was at exactly 40 K above ambient. For example, if the ambient temperature was 22° C, then the ideal surface temperature should be 62° C. However, if the heat flux is known to be 4000 W/m² at 59.4 K, then the heat transfer coefficient, h , is determined as $4000/(59.4 - 7) = 76.3 \text{ W/m}^2\text{-K}$ (7° C is the recovery temperature). Then this value of h can be used to determine the surface heat transfer if the surface temperature was 62° C; $76.3 \times (62 - 7) = 4198 \text{ W/m}^2$. In this way, the heat fluxes are compared for a surface temperature 40 K above ambient.

As mentioned in chapter 2, during the course of the experiments, several heat flux sensors were lost, but compiling the results from those available, the heat flux on the upper wall with a 40 K temperature difference between the wall and the core flow total temperature can be plotted and compared with numerical predictions as in Fig. 4.25.

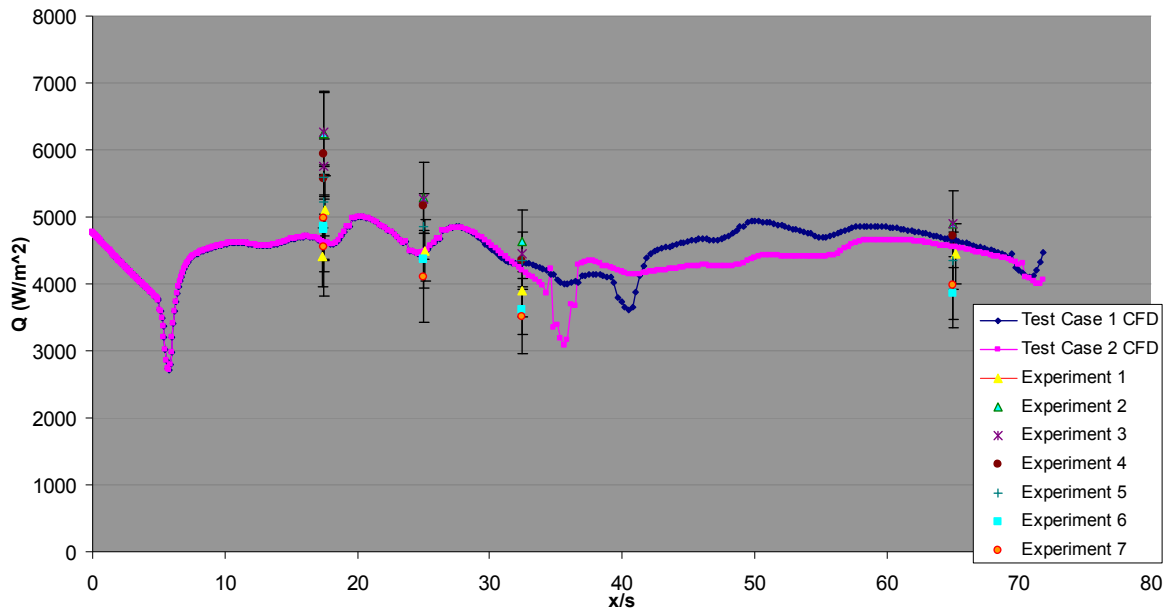


Fig. 4.25: Experimental heat flux results and comparison with numerical predictions for the upper wall.

The majority of heat flux measurements on the upper wall are consistent with numerical predictions within experimental error of 10%. This gives us some confidence in the heat flux measurements as they seem to be physically reasonable. However, the scatter between measurements is unacceptably large, and therefore, it is recommended to increase the surface temperature for future tests in order to decrease the random error.

4.3.2 Lower Wall Heat Flux with No Film Flow

Heat flux on the lower wall with no film flow was measured in the same way as for the upper wall. The results for heat flux along the lower wall with no film flow, and its comparison with numerical results, is shown in Fig. 4.26.

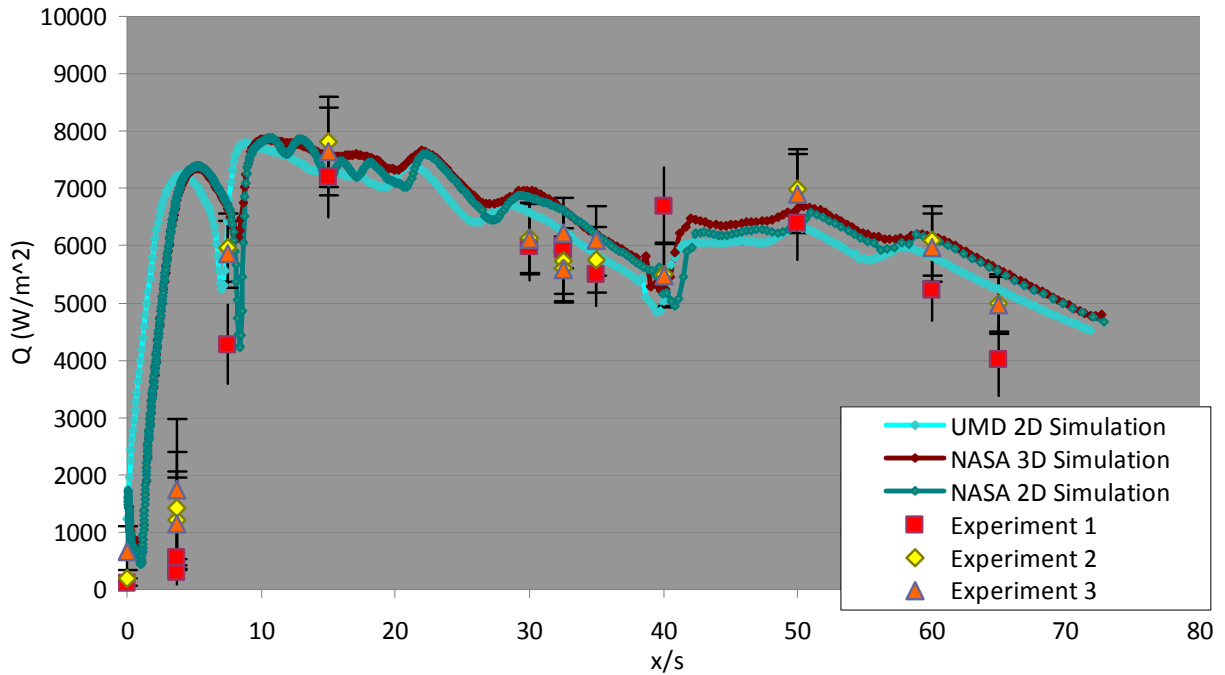


Fig. 4.26: Experimental and numerical results for lower wall heat flux with no film flow.

It can be seen from Fig. 4.26 that the experimental and numerical results exhibit the same trends: initially, there is little or no heat flux. This is followed by a spike at the reattachment point which raises the heat flux to over 7000 W/m²-K. After this spike, the heat flux gradually declines but then spikes upwards again due to shock impingement, only to gradually decrease once again. While the qualitative trends and the magnitude of the heat fluxes largely agree, there is some disagreement between experimental and numerical results over the exact locations of the spikes.

It is interesting to note that the heat flux is experimentally observed to rise sharply after 4 slot heights, whereas the numerical solver predicts a sharp rise in heat flux almost immediately after the step. This is in keeping with the trends observed in Fig.

4.19: it can be seen that the numerical solver predicts a much sharper decline of the shear layer than experimentally observed. In other words, the numerical density gradient contour shows the reattachment point to be much closer to the step than is experimentally observed. This explains the discrepancy between the experimental and numerical heat flux profiles.

Chapter 5: Conclusion

5.1 Summary of Findings

The main goal of this work is to provide measurements of wall heat transfer and flow field properties in canonical supersonic flows that can be used to validate numerical simulation tools. To this end, a facility for acquiring fundamental supersonic film cooling data has been designed, constructed, and operated to obtain some preliminary results. An analytical method for determining surface heat flux from an interior temperature measurement has been extended to include the effects of an initially non-isothermal test surface (plate). A new expression for transient temperature profiles and surface heat flux for a wall undergoing convective heat transfer with non-uniform initial temperature is also derived. It is found that the error from assuming an initially isothermal wall increases with time but is not substantial ($< 5\%$) for test times below 10 seconds and/or initial temperature gradients below 300 K/m for MACOR. In light of this work, it is concluded that thermal non-uniformities in the test plate have a negligible impact on the heat flux measurements, and the assumption of an initially isothermal test plate is reasonable.

The heat flux measurement technique is validated via comparison to numerical simulations of 1-D wall heat transfer, application of known heat flux boundary conditions to the instrumentation, and by comparing heat fluxes measured using the

technique to those predicted using CFD. Taken together, these efforts indicate that technique is capable of estimating wall heat flux within an uncertainty of +/- 10%.

Preliminary measurements of shear layer growth rate, wall pressure distributions, and wall heat flux are reported and compared with LOCI-CHEM RANS simulations.

They suggest that LOCI-Chem over-predicts viscous effects leading to boundary layer and shear layer thicknesses that are about twice as large as those suggested by Schlieren images. The disagreement between experimental and numerical results is greatest with no film flow but decreases as the film Mach number is increased.

Finally, preliminary heat flux measurements were also made for the case of no film flow which is essentially supersonic flow over a rearward-facing step. Measured surface heat flux is small immediately after the step (up to about 5 slot heights) but spikes when the core flow reattaches to the wall. The numerical results also indicate that the heat flux is small immediately after the step, but the rise in heat flux occurs much closer to the step than observed experimentally. This indicates that LOCI-Chem predicts flow reattachment much sooner than experimentally observed and reinforces what is seen in the Schlieren images. While there is discrepancy in surface heat flux in the vicinity of the step, LOCI-Chem correctly predicts the heat flux over the remainder of the test surface (largely within 15%).

5.2 Main Contributions

- 1) An instrumented apparatus to simulate supersonic film cooling in a canonical configuration has been developed.
- 2) An new and relatively easy to use inverse heat flux measurement technique (surface heat flux determined by an interior temperature response) capable of handling initially non-isothermal walls has been developed and verified.
- 3) It has been established that the error from assuming an initially isothermal wall in convective heat transfer studies is not substantial, unless the test times are long and/or the initial thermal gradient is high.
- 4) Preliminary Schlieren, pressure, and heat flux measurements indicate that RANS solvers like LOCI-CHEM do not predict shear layer thickness or growth rate correctly in the film cooling flows investigated here. One important problem appears to be the over-prediction of viscous effects.

5.3 Future Work

Recommendations for future work include:

- 1) Heat transfer measurements with a heated film flow should be made. This will determine the film cooling effectiveness, which can then be compared with numerical results. This will allow more rigorous assessment of LOCI-Chem in predicting film cooling flows.
- 2) Studies on film cooling with a favorable pressure gradient should be conducted. This is more realistic for simulating a rocket nozzle.

- 3) This study compares experimental results to numerical results using only one turbulence model (Menter's SST). Numerical results using additional turbulence models should be compared to determine which is best for predicting flows of this nature.

Appendix A: Method of Characteristics MATLAB Code

```
Mach_Design = 1.4;
Number_of_char_lines = 17;
Starting_angle = 0.375;
Throat_Height = 1.0;

Theta_Max_min_length = nu(Mach_Design)/2;

delta_Theta = (Theta_Max_min_length -
Starting_angle)/(Number_of_char_lines-1);

for i = 1:Number_of_char_lines
    Theta(i,1) = Starting_angle + (i-1)*delta_Theta;
    nu_flow(i,1) = Theta(i,1);
    K_plus(i,1) = 0.0;
    K_minus(i,1) = 2*Theta(i,1);
end

Theta(i+1,1) = Theta(i,1);
nu_flow(i+1,1) = nu_flow(i,1);
K_plus(i+1,1) = K_plus(i,1);
K_minus(i+1,1) = K_minus(i,1);

i = i+1;

k=i+1;

for j = 1:Number_of_char_lines-1
    l = Number_of_char_lines+1-j;
    for m = k:k+1
        K_minus(m,1) = K_minus(m-1,1);
        K_plus(m,1) = -K_minus(k-1,1);
        Theta(m,1) = 0.5*(K_minus(m,1)+K_plus(m,1));
        nu_flow(m,1) = 0.5*(K_minus(m,1)-K_plus(m,1));
    end
    k=m;
end

% adding Mach number and Mach angle

for i = 1:length(K_minus)
    Mach(i,1) = nu_inverse(nu_flow(i,1));
    Mach_angle(i,1) = asind(1/Mach(i,1));
    K_plus_angle(i,1) = Theta(i,1)+Mach_angle(i,1);
    K_minus_angle(i,1) = Theta(i,1)-Mach_angle(i,1);
end

K_minus = K_minus(1:length(K_minus)-1, 1);
K_plus = K_plus(1:length(K_plus)-1, 1);
Theta = Theta(1:length(Theta)-1, 1);
nu_flow = nu_flow(1:length(nu_flow)-1, 1);
```

```

Mach = Mach(1:length(Mach)-1, 1);
Mach_angle = Mach_angle(1:length(Mach_angle)-1, 1);
K_plus_angle = K_plus_angle(1:length(K_plus_angle)-1, 1);
K_minus_angle = K_minus_angle(1:length(K_minus_angle)-1, 1);

% Now we need to begin the painful process of generating the
% coordinates

% NOTE: first we are only calculating the internal points, not
the wall
% points

%First get coordinates of the first set of points

[x_pos(1) y_pos(1)] = find_intersection(0, Throat_Height,
K_minus_angle(1), 0,0,0);

for i = 2:Number_of_char_lines
    [x_pos(i) y_pos(i)] = find_intersection(0, Throat_Height,
K_minus_angle(i), x_pos(i-1), y_pos(i-1), K_plus_angle(i-1));
end

i = i+1;

for j = 1:Number_of_char_lines-2
    i = i+1;
    [x_pos(i) y_pos(i)] = find_intersection(x_pos(i-
Number_of_char_lines-1+j), y_pos(i-Number_of_char_lines-1+j),
K_minus_angle(i-Number_of_char_lines-1+j), 0, 0, 0);
    i = i+1;
    for l = i:i+Number_of_char_lines-2-j
        [x_pos(l) y_pos(l)] = find_intersection(x_pos(l-
Number_of_char_lines-1+j), y_pos(l-Number_of_char_lines-1+j),
K_minus_angle(l-Number_of_char_lines-1+j), x_pos(l-1), y_pos(l-1),
K_plus_angle(l-1));
    end
    i = l+1;
end

% calculation of the troublesome end point

i = i+1;
[x_pos(i) y_pos(i)] = find_intersection(x_pos(i-2), y_pos(i-2),
K_minus_angle(i-2), 0, 0, 0);

% Calculation of Internal points complete - Now calculate Wall
Points

% Calculate first Wall Point

Wall_x(1) = 0.0;
Wall_y(1) = Throat_Height;

```

```

    [x_pos(Number_of_char_lines+1) y_pos(Number_of_char_lines+1)] =
    find_intersection(0, Throat_Height,
    0.5*(Theta_Max_min_length+Theta(Number_of_char_lines+1)),
    x_pos(Number_of_char_lines), y_pos(Number_of_char_lines),
    K_plus_angle(Number_of_char_lines));

    index = Number_of_char_lines+1;

    Wall_x(2) = x_pos(index);
    Wall_y(2) = y_pos(index);

    for t = 1:Number_of_char_lines-1
        old_index = index;
        index = index + Number_of_char_lines-t+1;

        [x_pos(index) y_pos(index)] =
        find_intersection(x_pos(old_index), y_pos(old_index),
        0.5*(Theta(old_index)+Theta(index)), x_pos(index-1), y_pos(index-1),
        K_plus_angle(index-1));

        Wall_x(t+2) = x_pos(index);
        Wall_y(t+2) = y_pos(index);
    end

    plot(x_pos, y_pos);
    axis equal;
    hold on
    plot(Wall_x, Wall_y, 'r')

```

Subroutine nu_inverse:

```

function M = nu_inverse(nu)

M = 1.01;
gamma = 1.4;

deriv = - (gamma + 1)*M / (sqrt(M^2 - 1)*(2+(gamma-1)*M^2)) + 1 /
(M*sqrt(M^2 - 1));
func = nu*pi()/180 - sqrt((gamma+1)/(gamma-1)) * atan(sqrt((gamma -
1)*(M^2 - 1)/(gamma + 1))) + atan(sqrt(M^2 - 1));
new_M = M - func/deriv;

while abs(new_M - M) >= 1e-6
    M = new_M;
    deriv = - (gamma + 1)*M / (sqrt(M^2 - 1)*(2+(gamma-1)*M^2)) + 1
/ (M*sqrt(M^2 - 1));
    func = nu*pi()/180 - sqrt((gamma+1)/(gamma-1)) *
atan(sqrt((gamma - 1)*(M^2 - 1)/(gamma + 1))) + atan(sqrt(M^2 - 1));
    new_M = M - func/deriv;
end

M = abs(real(new_M));

```

Subroutine find_intersection:

```
function [x y] = find_intersection( x1, y1, Q1, x2, y2, Q2 )  
  
x = (y2 - y1 + x1*tand(Q1) - x2*tand(Q2))/(tand(Q1)-tand(Q2));  
y = ((x2-x1)*tand(Q1)*tand(Q2) - y2*tand(Q1) +  
y1*tand(Q2))/(tand(Q2)-tand(Q1));
```

Appendix B: Derivation of Inverse Method

This appendix derives the method of Chen, Chiou, and Thomsen^{20,22}.

The governing equation and initial and boundary conditions for the problem are stated in section 3.2.1:

$$\frac{\partial \theta}{\partial \tau} = \frac{\partial^2 \theta}{\partial X^2} \quad (3-3)$$

$$\theta(X, 0) = 0 \quad \theta(1, \tau) = f(\tau) \quad \theta(\infty, \tau) = 0 \quad (3-4)$$

The Laplace transform can be used to solve this problem. Let the transformation be

$$\bar{\theta}(X, s) = \int_0^{\infty} \theta(X, \tau) e^{-s\tau} d\tau \quad (B-1)$$

Transforming the governing and the initial and boundary conditions, the result is

$$\frac{d^2 \bar{\theta}}{dX^2} = s \bar{\theta} \quad (B-2)$$

$$\bar{\theta}(1, s) = \bar{f}(s) \quad \bar{\theta}(\infty, s) = 0 \quad (B-3)$$

The solution to this problem is

$$\bar{\theta}(X, s) = \bar{f}(s) e^{\sqrt{s}(1-X)} \quad (B-4)$$

Unfortunately, the term involving $e^{\sqrt{s}}$ cannot be inverted back to the time-domain. To address this problem, if the temperature profile is assumed to be of the form

$$f(\tau) = \sum_{n=1}^N b_n (4\tau)^n \Gamma(n+1) i^{2n} \operatorname{erfc}\left(\frac{1}{2\sqrt{\tau}}\right) \quad (3-5)$$

Then in the Laplace domain, this is

$$\bar{f}(s) = e^{-\sqrt{s}} \sum_{n=1}^N \Gamma(n+1) \frac{b_n}{s^{1+n}} \quad (B-5)$$

Which can cancel the $e^{\sqrt{s}}$ term in eq. (B-4). Substituting eq. (B-5) into eq. (B-4) and differentiating yields,

$$\bar{\theta}(X, s) = e^{-X\sqrt{s}} \sum_{n=1}^N \Gamma(n+1) \frac{b_n}{s^{1+n}} \quad (B-6)$$

$$-\frac{\partial \bar{\theta}}{\partial X} = e^{-X\sqrt{s}} \sum_{n=1}^N \Gamma(n+1) \frac{b_n}{s^{\frac{1}{2}+n}} \quad (B-7)$$

Equations (B-6) and (B-7) can now be inverted back to the time domain to yield

$$\theta(0, \tau) = \sum_{n=1}^N b_n \tau^n \quad (3-6)$$

$$-\frac{\partial \theta(0, \tau)}{\partial X} = \sum_{n=1}^N b_n \tau^{n-1/2} \frac{\Gamma(n+1)}{\Gamma(n+1/2)} \quad (3-7)$$

Appendix C: Inverse Method MATLAB Code

```
tic

load 'C:\J-2X\Data\Full
runs\Upper_wall_heat_28_Oct_2010\upper_wall_heat_flux_10-10-
28_1240.lvm'

alpha = (7.3e-7);
x = 0.00127;
k = 1.46;

% control panel starts

tunnel_start_time = 6;
data_start_index = (tunnel_start_time+1)*100;
data_end_index = (tunnel_start_time+4)*100;

times =
upper_wall_heat_flux_10_10_28_1240((data_start_index:data_end_index)
,1);
temps =
upper_wall_heat_flux_10_10_28_1240((data_start_index:data_end_index)
,3);
T_init = 68.8;
temp_gradient = 0.05;

% control panel ends

figure(1)
plot(times, temps, 'k:')
hold on

tgc = 0;
for tgc = 1:length(temps)
    temps(tgc) = temps(tgc) + (times(tgc)-
tunnel_start_time)*temp_gradient;
end

plot(times, temps)

% Non-dimensionalize time, temperature, and distance
nd_times = alpha.*times./(x^2);
nd_temps = (temps - T_init)/T_init;

% set number of terms

n = 20;

% precalculate coefficients of b
```

```

for t_counter = 1:1:length(nd_times)
    for n_counter = 1:1:n
        inerf_terms(t_counter, n_counter) = inerf(2*n_counter,
0.5/sqrt(nd_times(t_counter)));
        pre_coeffs(t_counter, n_counter) =
((4*nd_times(t_counter))^n_counter)*gamma(n_counter+1)*inerf_terms(t
_counter, n_counter);
    end
end

toc

options = optimset('fminsearch');
options = optimset(options, 'Display', 'iter');
options = optimset(options, 'MaxFunEvals', 500000);
options = optimset(options, 'MaxIter', 500000);
options = optimset(options, 'TolFun', 1e-18);
options = optimset(options, 'TolX', 1e-18);
bs = fminsearch(@(bs) temperature_fmin_function(bs, pre_coeffs,
nd_times, nd_temps), -0.02.*zeros(1,n), options)

%curve fit

for cc = 1:length(nd_times)
    fit_temp = 0;
    for bb = 1:length(bs)
        fit_temp = fit_temp +
bs(bb)*(4*nd_times(cc))^bb*gamma(bb+1)*inerf_terms(cc, bb);
    end

    fit_temps(cc) = fit_temp;
end

toc

figure(2)
plot(nd_times, nd_temps)
hold on
plot(nd_times, fit_temps, 'k--')
xlabel('Non-dimensional time')
ylabel('Non-dimensional temperature')
title('Sensor Location Temperature')

figure(3)
plot(nd_times.*(x^2)./alpha, 100*(fit_temps'-nd_temps)./nd_temps)
xlabel('Time (sec)')
ylabel('% Error')
title('Sensor Location Temperature')
hold on

for cc = 1:length(nd_times)
    fit_q = 0;
    for bb = 1:length(bs)

```

```

    fit_q = fit_q + bs(bb)*(nd_times(cc))^(bb-
0.5)*gamma(bb+1)/gamma(bb+0.5);
    end

    fit_qs(cc) = fit_q*k*T_init/(x);
end

figure(4)
plot(nd_times.*(x^2)./alpha, -fit_qs, 'k--')
xlabel('Time (seconds)')
ylabel('Surface Heat Flux (W/m^2)')
%plot(nd_times.*((N_sensor-1)*delta_x)^2)./alpha, -fit_qs+(a*k),
'r--')
hold on

for cc = 1:length(nd_times)
    fit_surface_temp = 0;
    for bb = 1:length(bs)
        fit_surface_temp = fit_surface_temp +
bs(bb)*(nd_times(cc))^(bb);
    end

    fit_surface_temps(cc) = fit_surface_temp*T_init + T_init;
end

figure(5)
plot(nd_times.*(x^2)./alpha, fit_surface_temps, 'r--')
xlabel('Time (sec)')
ylabel('Surface Temperature (K)')

dimensional_times = nd_times.*(x^2)./alpha;
fit_coeffs = polyfit(dimensional_times(22:202)', -fit_qs(22:202),
1)

figure(6)
plot(nd_times.*(x^2)./alpha, -fit_qs, 'k--')
xlabel('Time (seconds)')
ylabel('Surface Heat Flux (W/m^2)')
%plot(nd_times.*((N_sensor-1)*delta_x)^2)./alpha, -fit_qs+(a*k),
'r--')
hold on
plot(dimensional_times, fit_coeffs(1)*dimensional_times +

subroutine inerf:

function x = inerf(n,z)

hfg = M((n+1)/2,0.5, z^2);
hfg = hfg/((2^n)*gamma((n/2)+1));
hfg = hfg - (z/((2^(n-1))*gamma((n+1)/2)))*M((n/2)+1,1.5, z^2);
x = hfg*exp(-(z^2));

subroutine temperature_fmin_function:

```

```

function K = temperature_fmin_function(bs, pre_coeffs, xdata, ydata)

error_square = 0;

for i = 1:1:length(xdata)

    total = 0;

    for n = 1:1:length(bs)
        total = total + bs(n)*pre_coeffs(i,n);
    end

    error_square = error_square + (total - ydata(i))^2;

end

K = error_square;

```

Subroutine M:

```

function yeah = M(j, f, k)
%This program is a direct conversion of the corresponding Fortran
program in
%S. Zhang & J. Jin "Computation of Special Functions" (Wiley, 1996).
%online: http://iris-lee3.ece.uiuc.edu/~jjin/routines/routines.html
%
%Converted by f2matlab open source project:
%online: https://sourceforge.net/projects/f2matlab/
% written by Ben Barrowes (barrowes@alum.mit.edu)
%
%
% =====
% Purpose: This program computes the confluent
% hypergeometric function M(a,b,x) using
% subroutine CHGM
% Input : a --- Parameter
% b --- Parameter (b <> 0,-1,-2,...)
% x --- Argument
% Output: HG --- M(a,b,x)
% Example:
% a      b      x      M(a,b,x)
% -----
% 1.5    2.0    20.0    .1208527185D+09
% 4.5    2.0    20.0    .1103561117D+12
% -1.5   2.0    20.0    .1004836854D+05
% -4.5   2.0    20.0    -.3936045244D+03
% 1.5    2.0    50.0    .8231906643D+21
% 4.5    2.0    50.0    .9310512715D+25
% -1.5   2.0    50.0    .2998660728D+16
% -4.5   2.0    50.0    -.1806547113D+13
% =====
a=[];b=[];x=[];

```

```

hg=[];
% fprintf(1,'%s \n','please enter a, b and x ');
%   READ(*,*)A,B,X
a=j;
b=f;
x=k;
% fprintf(1,'%s \n','   a       b       x       m(a,b,x)');
% fprintf(1,'%s \n',' -----');
[a, b, x, hg]=chgm(a,b,x,hg);

% fprintf(1,[repmat(' ',1,1),'%5.1g',repmat('
',1,3),'%5.1g',repmat(' ',1,3),'%5.1g','%20.10g' ' \n'],a,b,x,hg);
%format(1x,f5.1,3x,f5.1,3x,f5.1,d20.10);
yeah = hg;
end

function [a,b,x,hg]=chgm(a,b,x,hg,varargin);
%
%   =====
%   Purpose: Compute confluent hypergeometric function
%   M(a,b,x)
%   Input  : a --- Parameter
%   b --- Parameter(b <> 0,-1,-2,...)
%   x --- Argument
%   Output: HG --- M(a,b,x)
%   Routine called: GAMMA for computing  $\hat{a}(x)$ 
%   =====
ta=[];tb=[];xg=[];tba=[];
pi=3.141592653589793d0;
a0=a;
a1=a;
x0=x;
hg=0.0d0;
if(b == 0.0d0|b == -abs(fix(b)));
hg=1.0d+300;
elseif(a == 0.0d0|x == 0.0d0);
hg=1.0d0;
elseif(a == -1.0d0);
hg=1.0d0-x./b;
elseif(a == b);
hg=exp(x);
elseif(a-b == 1.0d0);
hg=(1.0d0+x./b).*exp(x);
elseif(a == 1.0d0&b == 2.0d0);
hg=(exp(x)-1.0d0)./x;
elseif(a == fix(a)&a < 0.0d0);
m=fix(-a);
r=1.0d0;
hg=1.0d0;
for k=1:m;
r=r.*(a+k-1.0d0)./k./(b+k-1.0d0).*x;
hg=hg+r;
end; k=m+1;
end;
if(hg ~= 0.0d0) return; end;
if(x < 0.0d0);
a=b-a;

```

```

a0=a;
x=abs(x);
end;
if(a < 2.0d0)n1=0; end;
if(a >= 2.0d0);
n1=1;
la=fix(a);
a=a-la-1.0d0;
end;
for n=0:n1;
if(a0 >= 2.0d0)a=a+1.0d0; end;
if(x <= 30.0d0+abs(b) | a < 0.0d0);
hg=1.0d0;
rg=1.0d0;
for j=1:500;
rg=rg.*(a+j-1.0d0)./(j.*(b+j-1.0d0)).*x;
hg=hg+rg;
if(abs(rg./hg)< 1.0d-15)break; end;
end;
else;
[a,ta]=gamma(a,ta);
[b,tb]=gamma(b,tb);
xg=b-a;
[xg,tba]=gamma(xg,tba);
sum1=1.0d0;
sum2=1.0d0;
r1=1.0d0;
r2=1.0d0;
for i=1:8;
r1=-r1.*(a+i-1.0d0).*(a-b+i)./(x.*i);
r2=-r2.*(b-a+i-1.0d0).*(a-i)./(x.*i);
sum1=sum1+r1;
sum2=sum2+r2;
end; i=8+1;
hg1=tb./tba.*x.^(-a).*cos(pi.*a).*sum1;
hg2=tb./ta.*exp(x).*x.^(a-b).*sum2;
hg=hg1+hg2;
end;
if(n == 0)y0=hg; end;
if(n == 1)y1=hg; end;
end;
if(a0 >= 2.0d0);
for i=1:la-1;
hg=((2.0d0.*a-b+x).*y1+(b-a).*y0)./a;
y0=y1;
y1=hg;
a=a+1.0d0;
end; i=la-1+1;
end;
if(x0 < 0.0d0)hg=hg.*exp(x0); end;
a=a1;
x=x0;
return;
end
function [x,ga]=gamma(x,ga,varargin);
% =====
% Purpose: Compute gamma function  $\hat{a}(x)$ 

```

```

%      Input : x --- Argument of  $\hat{a}(x)$ 
%(x is not equal to 0,-1,-2,úúú)
%      Output: GA ---  $\hat{a}(x)$ 
%      =====
g=zeros(1,26);
pi=3.141592653589793d0;
if(x == fix(x));
if(x > 0.0d0);
ga=1.0d0;
m1=x-1;
for k=2:m1;
ga=ga.*k;
end; k=m1+1;
else;
ga=1.0d+300;
end;
else;
if(abs(x)> 1.0d0);
z=abs(x);
m=fix(z);
r=1.0d0;
for k=1:m;
r=r.*(z-k);
end; k=m+1;
z=z-m;
else;
z=x;
end;
g(:)=[1.0d0,0.5772156649015329d0,-0.6558780715202538d0,-
0.420026350340952d-1,0.1665386113822915d0,-.421977345555443d-1,-
.96219715278770d-2,.72189432466630d-2,-.11651675918591d-2,-
.2152416741149d-3,.1280502823882d-3,-.201348547807d-4,-
.12504934821d-5,.11330272320d-5,-.2056338417d-6,.61160950d-
8,.50020075d-8,-.11812746d-8,.1043427d-9,.77823d-11,-.36968d-
11,.51d-12,-.206d-13,-.54d-14,.14d-14,.1d-15];
gr=g(26);
for k=25:-1:1;
gr=gr.*z+g(k);
end; k=1-1;
ga=1.0d0./(gr.*z);
if(abs(x)> 1.0d0);
ga=ga.*r;
if(x < 0.0d0)ga=-pi./(x.*ga.*sin(pi.*x)); end;
end;
end;
return;
end

```

Appendix D: Full-view Schlieren Images

Test Case 3:



Test case 2:



Test Case 1:



Test Case: No Film Flow



Bibliography

- ¹Sutton, G. P. and Biblarz, O., "Rocket Propulsion Elements," 7th Edition, Wiley-Interscience, 2000.
- ²Kerrebrock, J. L., "Aircraft Engines and Gas Turbines," 2nd Edition, The MIT Press, 1992.
- ³Hunt, M. L., Juhany, K. A., and Sivo, J. M., "Supersonic Film Cooling using Air and Helium for a Range of Injectant Temperatures and Mach Numbers," AIAA-94-1416, AIAA 26th Thermophysics Conference, June 1991, Honolulu, HI.
- ⁴Hansmann, T., Wilhelmi, H., and Bohn, D., "An Experimental Investigation of the Film Cooling Process at High Temperatures and Velocities," AIAA-93-5062, AIAA/DGLR 5th International Aerospace Planes and Hypersonics Technologies Conference, Nov. – Dec. 1993, Munich, Germany.
- ⁵Dellimore, K., "Modeling and Simulation of Mixing Layer Flows for Rocket Engine Film Cooling," Ph.D. Dissertation, University of Maryland, 2010.
- ⁶Goldstein, R. J., Eckert, E. R. G., Tsou, F. K., and Haji-Sheikh, A., "Film Cooling with Air and Helium Injection Through a Rearward-Facing Slot into a Supersonic Air Flow," AIAA Journal, Vol. 4, pp. 981-985, June 1966.
- ⁷Bass, R., Hardin, L., and Rodgers, R., "Supersonic Film Cooling," AIAA-90-5239, AIAA 2nd International Aerospace Planes Conference, Oct. 1990, Orlando, FL.
- ⁸Dannenber, R. E., "Helium Film Cooling on a Hemisphere at a Mach Number of 10," NASA Technical Note D-1550, Nov. 1962.
- ⁹Lucas, J. G. and Golladay, R. L., "Gaseous Film Cooling of a Rocket Motor with Injection near the Throat," NASA Technical Note D-3836, Feb. 1967.
- ¹⁰Aupoix, B., Mignosi, A., Viala, S., Bouvier, F., and Gaillard, R., "Experimental and Numerical Study of Supersonic Film Cooling," AIAA Journal, Vol. 36 no. 6, pp. 915-923, 1998.
- ¹¹Juhany, K. A. and Hunt, M. L., "Flow-Field Measurements in Supersonic Film Cooling Including the Effect of Shock Wave Interaction," AIAA-92-2950, AIAA 27th Thermophysics Conference, July 1992, Nashville, TN.
- ¹²Kanda, T., Ono, F., and Saito, T., "Experimental Studies of Supersonic Film Cooling with Shock Wave Interaction," AIAA-1996-2663, AIAA/ASME/SAE/ASEE 32nd Joint Propulsion Conference and Exhibit, July 1996, Lake Buena Vista, FL.
- ¹³Peng, W. and Jiang, P., "Influence of Shock Waves on Supersonic Film Cooling," AIAA Journal of Spacecraft and Rockets, Vol. 46 no. 1, pp 67-73, 2009.
- ¹⁴Takita, K. and Masuya, G., "Effects of Shock Wave Impingement on Supersonic Film Cooling," AIAA Journal of Spacecraft and Rockets, Vol. 36 no. 4, pp. 602-604, 1999.
- ¹⁵Diller, T.E., "Advances in Heat Flux Measurements," Advances in Heat Transfer, volume 23, 1993.
- ¹⁶Schultz, D.L. and Jones, T.V. "Heat Transfer Measurements in Short-Duration Hypersonic Facilities". AGARD Report, AGARD-AG-165, 1973.
- ¹⁷Yan, X.T., "On the Penetration Depth in Fourier Heat Conduction," 8th AIAA/ASME Joint Thermophysics and Heat Transfer Conference, June 2002, St. Louis, MO.
- ¹⁸Beck, J.V., Blackwell, B., and Haji-Sheikh, A., "Comparison of Some Inverse Heat Conduction Methods using Experimental Data," International Journal of Heat and Mass Transfer, vol. 39, no. 17, 1996, pp. 3649 – 3657.
- ¹⁹Ozisik, M.N. and Orlande, H.R.B., "Inverse Heat Transfer," Taylor & Francis, 2000.
- ²⁰Chen, C.J. and Thomsen, D.M., "On Determination of Transient Surface Temperature and Heat Flux by Imbedded Thermocouple in a Hollow Cylinder," AIAA Journal, vol. 13, no. 5, 1975, pp. 697 – 699.
- ²¹Imber, M. and Khan, J., "Prediction of Transient Temperature Distributions with Embedded Thermocouples," AIAA Journal, vol. 10, no. 6, 1972, pp. 784 – 789.
- ²²Chen, C.J. and Chiou, J.S., "Prediction of Surface Temperature and Heat Flux from an Interior Temperature Response," Letters in Heat and Mass Transfer, vol. 3, 1976, pp. 539 – 548.
- ²³Monde, M., "Analytical Method in Inverse Heat Transfer Problem using Laplace Transform Technique," International Journal of Heat and Mass Transfer, vol. 43, 2000, pp. 3965 – 3975.
- ²⁴Abramowitz, M. and Stegun, I.A., "Handbook of Mathematical Functions," National Bureau of Standards, Applied Mathematics Series, 7th Ed., May 1968, pp. 300.
- ²⁵Carslaw, H.S. and Jaeger, J.C., "Conduction of Heat in Solids," 2nd Edition, Oxford University Press, 1959, pp. 70-73.

- ²⁶Smith, H. E., "The Flow Field and Heat Transfer Downstream of a Rearward Facing Step in Supersonic Flow," *ARL 67-0056, Aerospace Research Laboratories, March 1967*.
- ²⁷R. M. C. So, H. S. Zhang, and C. G. Speziale, "Near Wall Modeling of the Dissipation Rate Equation," AIAA 92-0441, 30th Aerospace Sciences Meeting & Exhibit, Reno, NV, Jan. 1992.
- ²⁸Kays, W.M. and Crawford, M.E. "Convective Heat and Mass Transfer". *McGraw-Hill, 1993*.
- ²⁹Gnielinski, V. "New Equations for Heat and Mass Transfer in Turbulent Pipe and Channel Flow". *Int. Chem. Eng., vol. 16, 1976 (p. 359 – 368)*.
- ³⁰McAdams, W.H., "Heat Transmission". *McGraw-Hill, 1954*.
- ³¹Lloyd, J.R. and Moran, W.R., "Natural Convection Adjacent to Horizontal Surfaces of Various Planforms". *Paper 74-WA/HT-66, ASME, 1974*.
- ³²Personal Communication with Joseph H. Ruf of NASA Marshall Space Flight Center.
- ³³"Test Uncertainty," ASME PTC 19.1-1998, American Society of Mechanical Engineers.
- ³⁴Hollis, B. R. and Perkins, J. N., "Transition Effects on Heating in the Wake of a Blunt Body," AIAA 97-2569, 32nd AIAA Thermophysics Conference, Atlanta, GA, June 1997.
- ³⁵Hollis, B. R., "User's Manual for the One-Dimensional Hypersonic Aero-Thermodynamic (1DHEAT) Data Reduction Code," NASA CR 4691, August 1991.